LA-13188-T
Thesis

A Kinetic Study of Plutonium Dioxide Dissolution in Hydrochloric Acid Using Iron (II) as an Electron Transfer Catalyst

Los Alamos
NATIONAL LABORATORY

Los Alamos National Laboratory is operated by the University of California for the United States Department of Energy under contract W-7405-ENG-36.

This thesis was accepted by the Graduate School, New Mexico State University, Las Cruces, New Mexico, in partial fulfillment of the requirements for the degree of Doctor of Philosophy specializing in Chemical Engineering. The text and illustrations are the independent work of the author and only the front matter has been edited by the CIC-1 Writing and Editing Staff to conform with Department of Energy and Los Alamos National Laboratory publication policies.

An Affirmative Action/Equal Opportunity Employer

This report was prepared as an account of work sponsored by an agency of the United States Government. Neither The Regents of the University of California, the United States Government nor any agency thereof, nor any of their employees, makes any warranty, express or implied, or assumes any legal liability or responsibility for the accuracy, completeness, or usefulness of any information, apparatus, product, or process disclosed, or represents that its use would not infringe privately owned rights. Reference herein to any specific commercial product, process, or service by trade name, trademark, manufacturer, or otherwise, does not necessarily constitute or imply its endorsement, recommendation, or favoring by The Regents of the University of California, the United States Government, or any agency thereof. The views and opinions of authors expressed herein do not necessarily state or reflect those of The Regents of the University of California, the United States Government, or any agency thereof. The Los Alamos National Laboratory strongly supports academic freedom and a researcher's right to publish; therefore, the Laboratory as an institution does not endorse the viewpoint of a publication or guarantee its technical correctness.

LA-13188-T
Thesis

UC-701
Issued: September 1996

A Kinetic Study of Plutonium Dioxide Dissolution in Hydrochloric Acid Using Iron (II) as an Electron Transfer Catalyst

Keith William Fife

Los Alamos
NATIONAL LABORATORY
Los Alamos, New Mexico 87545

ACKNOWLEDGMENTS

This program has taken the better part of five years to complete and has been successfully integrated into a full-time career. I must thank the management and technical staff of the Nuclear Materials Technology Division at Los Alamos National Laboratory for their support of this degree program. They not only provided the fundamental opportunity for this investigation, but they provided all financial support, mentor opportunities, and the laboratory facilities to accomplish this work.

I especially thank Wayne H. Smith for his help in understanding and troubleshooting the electrochemical systems as well as for many helpful discussions and comments, to Louis D. Schulte for his continued interest and helpful discussions regarding this research topic, to Gregory D. Bird and Charles C. Davis for their operation of the LASENTEC LAB-TEC™ 1000 instrument performing the transit time measurements of PuO_2 particle size distribution and surface area, to Michael D. Greenbank for all photography, and to Robert F. Meehan for the electronic versions of the cyclic voltammograms. Also to be recognized for their support are Dana C. Christensen, Joel D. Williams, and Stephen L. Yarbro (all soon to complete their doctorates) for pursuing this degree program in this manner.

The Department of Chemical Engineering at NMSU is to be recognized for their open support and vision; not only for this work, but for taking the chance to initiate and develop this novel distance learning program for which I am proud to have been a part. Key in originally initiating and developing this program is Dr. Stanford T. Holbrook.

And for the gracious use of Fig. 2.1b and Fig. 2.2 in this text, the American Chemical Society is acknowledged.

TABLE OF CONTENTS

LIST OF TABLES....x

LIST OF APPENDIX TABLES....xi

LIST OF FIGURES....xiii

LIST OF APPENDIX FIGURES....xvi

ABSTRACT....xix

1 INTRODUCTION....1

1.1 Purpose of the Research....2

1.2 Research Goals....4

2 LITERATURE REVIEW....6

2.1 The Plutonium-Oxygen System....6

2.2 Dissolution of Plutonium Oxide....8

2.2.1 PuO_2 Dissolution Without Redox....11

2.2.2 Oxidative PuO_2 Dissolution....13

2.2.3 Reductive PuO_2 Dissolution....14

2.3 Heterogeneous Reaction Systems....15

2.3.1 PuO_2 Dissolution Kinetics....15

2.3.2 Noncatalytic Fluid-Solid Reactions....21

2.3.2.1 Nonporous Shrinking Spherical Particle–Surface Chemical Reaction Control....24

2.3.2.2 Nonporous Shrinking Spherical Particle–Diffusion Control for Small Particles in the Stoke's Law Regime....27
2.3.2.3 Nonporous Shrinking Spherical Particle–Diffusion Control for Large Particles with Initially High Reynolds Number....30

2.3.2.4 Uniformly Reacting Porous Spherical Particle–Surface Chemical Reaction Control....32

2.3.2.5 Concluding Remarks....37

2.4 Effect of Temperature on the Rate Determining Step....38

2.5 Voltammetry....42

2.6 Mixing and Segregation in Dry Particulate Systems....46

3 EXPERIMENTAL PROCEDURE....52

3.1 Overview....52

3.2 Equipment....59

3.2.1 Electrochemical and Associated Equipment....59

3.2.2 Particle Size and Sieving Equipment....62

3.3 Procedure....64

4 RESULTS AND DISCUSSION....78

4.1 Overview....78

4.2 Particle Size Analysis....89

4.3 Kinetic Analysis....96

5 CONCLUSIONS AND RECOMMENDATIONS.....118

5.1 Conclusions.....118

5.2 Recommendations.....121

REFERENCES.....123

APPENDIX: EXPERIMENTAL DATA.....131

LIST OF TABLES

Table 2.1: Thermodynamic Data for the Dissolution of PuO_2 10

Table 2.2: Rate-Limiting Mechanisms for Nonporous Fluid-Solid Reactions....23

Table 3.1: Analytical Composition of the PuO_2 used in this Study....55

Table 4.1: Sieve Results from the ATM Sonic Sieve....80

Table 4.2: Comparison of Linear Correlation Coefficients Between Chemical Reaction Control and Film Diffusion Control for the 50°C Dissolution Experiments....88

Table 4.3: Spherical Equivalent Mean Particle Size Data for ATM Screen Fractions and the Original PuO_2 Assemblage....95

Table 4.4: Comparison of Slope Data from the Linearized Surface Chemical Reaction Expression for All Experiments and the Calculation of First-Order Rate Constants....105

Table 4.5: All Data for the Slope of the Surface Reaction Relationship for the Dissolution of Various PuO_2 Sieve Fractions and the Oxide Assemblage....109

Table 4.6: Comparison of Parameters Obtained from Linearizing the Surface Reaction Control Model with Parameters Obtained from Nonlinear Least Squares Estimation....110

Table 4.7: Surface Chemical Reaction Control Rate Constants at the Various Arrhenius Temperatures....115

Table 4.8: Values of the Apparent Activation Energy for Different Oxide Dissolution Temperature Ranges....116

LIST OF APPENDIX TABLES

Table A-1: Experimental Data for February 1, 1994; Arrhenius Data at 40°C.....132

Table A-2: Experimental Data for February 14, 1994; Arrhenius Data at 28°C.....134

Table A-3: Experimental Data for February 28, 1994; Arrhenius Data at 28°C. 136

Table A-4: Experimental Data for March 14, 1994; Arrhenius Data at 40°C. 138

Table A-5: Experimental Data for November 17, 1995.....140

Table A-6: Experimental Data for November 20, 1995.....142

Table A-7: Experimental Data for November 21, 1995.....144

Table A-8: Experimental Data for November 29, 1995.....146

Table A-9: Experimental Data for November 30, 1995.....148

Table A-10: Experimental Data for December 1, 1995.....150

Table A-11: Experimental Data for December 12, 1995.....152

Table A-12: Experimental Data for December 13, 1995 am.....154

Table A-13: Experimental Data for December 13, 1995 pm.....156

Table A-14: Experimental Data for December 19, 1995.....158

Table A-15: Experimental Data for December 20, 1995.....160

Table A-16: Experimental Data for January 9, 1996.....162

Table A-17: Experimental Data for January 10, 1996 am.....164

Table A-18: Experimental Data for January 10, 1996 pm.....166

Table A-19: Experimental Data for January 11, 1996; Acid Titrated at 6 *M*.....168

Table A-20: Experimental Data for January 12, 1996; Acid Titrated at 6 *M*.....170

Table A-21: Experimental Data for January 16, 1996 am.....172

Table A-22: Experimental Data for January 16, 1996 pm.....174

Table A-23: Experimental Data for January 17, 1996.....176

Table A-24: Experimental Data for January 18, 1996.....178

Table A-25: Experimental Data for January 24, 1996; Arrhenius data at 60°C.....180

Table A-26: Experimental Data for January 26, 1996; Arrhenius Data at 65°C.....182

Table A-27: Experimental Data for February 8, 1996.....184

Table A-28: Experimental Data for February 13, 1996.....186

Table A-29: Experimental Data for February 14, 1996.....188

Table A-30: Experimental Data for February 15, 1996 am.....190

Table A-31: Experimental Data for February 15, 1996 pm.....192

Table A-32: Experimental Data for February 23, 1996.....194

Table A-33: Experimental Data for February 26, 1996.....196

Table A-34: Experimental Data for February 27, 1996 am.....198

Table A-35: Experimental Data for February 27, 1996 pm.....200

Table A-36: Experimental Data for February 28, 1996.....202

Table A-37: Experimental Data for May 9, 1996; Arrhenius Data at 75°C.....204

LIST OF FIGURES

Figure 2.1: Plutonium-oxygen phase diagram; (a) from Ellinger (1968) and (b) from Naito et al. (1992) 7

Figure 2.2: Theoretical solubility of PuO_2 in nitric acid (Ryan and Bray 1980) 12

Figure 2.3: Representation of a nonporous solid reacting with a fluid in which no solid product is formed.....22

Figure 2.4: (a) the potential waveform used in cyclic voltammetry, and (b) the resulting cyclic voltammogram.....45

Figure 3.1: Schematic of the electrochemical cell used for studying PuO_2 dissolution in the HCl-Fe(II) system.....53

Figure 3.2: The electrochemical cell used for studying PuO_2 dissolution in the HCl-Fe(II) system.....54

Figure 3.3: A series of cyclic voltammograms from the dissolution of plutonium oxide in HCl-Fe(II) showing the increase in dissolved plutonium as the dissolution proceeds.....58

Figure 3.4: Dissolution rate data from cyclic voltammogram peak-height ratios.....59

Figure 3.5: The ATM Sonic Sieve apparatus used for obtaining screen fractions of the PuO_2 assemblage.....65

Figure 3.6: Subtle shifting in the position of the anodic peak current for plutonium indicating possible degradation of the precision area working electrode.....74

Figure 3.7: Evident problems with the precision area working electrode.....75

Figure 3.8: The more subtle, progressive fouling of a precision area working electrode.....77

Figure 4.1: Spherical equivalent mean particle size distribution of the PuO_2 used in this study (number basis).....79

Figure 4.2: PuO_2 size distribution from sieving (weight basis).....81

Figure 4.3: Linearization of experimental rate data showing the applicability of various nonporous shrinking sphere models.....85

Figure 4.4: Comparison of nonporous shrinking sphere dissolution models with actual dissolution data for the PuO_2 assemblage.....87

Figure 4.5: Particle size distribution data from scanning laser microscopy and dry sieving for the plutonium oxide assemblage used in this study.....89

Figure 4.6: Illustration of the amorphous and possibly fragile nature of the PuO_2 used in this study.....91

Figure 4.7: Scanning laser microscopy particle size distribution on discrete oxide fractions produced from sieving compared with the original assemblage (spherical equivalent mean number distribution).....94

Figure 4.8: Appearance of needle-like structures in the original PuO_2 particle assemblage.....97

Figure 4.9: Assuming surface chemical reaction control, this figure illustrates the difference in the slope of the linearized rate expression among the varying oxide particle sizes compared with the oxide assemblage.....99

Figure 4.10: The extent of dissolution of varying oxide particle size fractions compared with the entire plutonium oxide assemblage.....100

Figure 4.11: Values of the slope for surface chemical reaction control from all experiments showing data variability.....102

Figure 4.12: Results of screening surface reaction controlled slope data from all experiments for data quality problems. Included is the 95% confidence interval determined from the standard error in the assemblage experiments.....103

Figure 4.13: Comparison of nonlinear least squares and linearized surface reaction models with experimental data for December 1, 1995.....112

Figure 4.14. A plot of residuals from five sets of data presented previously in Table 4.4.....113

Figure 4.15: Arrhenius data for the dissolution of PuO_2 in the HCl-Fe(II) system containing 7 *M* HCl and 40 *mM* Fe(II).....117

LIST OF APPENDIX FIGURES

Figure A-1: Experimental data for February 1, 1994; Arrhenius data at 40°C.....133

Figure A-2: Experimental data for February 14, 1994; Arrhenius data at 28°C.....135

Figure A-3: Experimental data for February 28, 1994; Arrhenius data at 28°C. 137

Figure A-4: Experimental data for March 14, 1994; Arrhenius data at 40°C. 139

Figure A-5: Experimental data for November 17, 1995.....141

Figure A-6: Experimental data for November 20, 1995.....143

Figure A-7: Experimental data for November 21, 1995.....145

Figure A-8: Experimental data for November 29, 1995.....147

Figure A-9: Experimental data for November 30, 1995.....149

Figure A-10: Experimental data for December 1, 1995.....151

Figure A-11: Experimental data for December 12, 1995.....153

Figure A-12: Experimental data for December 13, 1995 am.....155

Figure A-13: Experimental data for December 13, 1995 pm.....157

Figure A-14: Experimental data for December 19, 1995.....159

Figure A-15: Experimental data for December 20, 1995.....161

Figure A-16: Experimental data for January 9, 1996.....163

Figure A-17: Experimental data for January 10, 1996 am.....165

Figure A-18: Experimental data for January 10, 1996 pm.....167

Figure A-19: Experimental data for January 11, 1996; acid titrated at 6 *M*.....169

Figure A-20: Experimental data for January 12, 1996; acid titrated at 6 *M*.....171

Figure A-21: Experimental data for January 16, 1996 am.....173

Figure A-22: Experimental data for January 16, 1996 pm.....175

Figure A-23: Experimental data for January 17, 1996.....177

Figure A-24: Experimental data for January 18, 1996.....179

Figure A-25: Experimental data for January 24, 1996; Arrhenius data at 60°C.....181

Figure A-26: Experimental data for January 26, 1996; Arrhenius data at 65°C.....183

Figure A-27: Experimental data for February 8, 1996.....185

Figure A-28: Experimental data for February 13, 1996.....187

Figure A-29: Experimental data for February 14, 1996.....189

Figure A-30: Experimental data for February 15, 1996 am.....191

Figure A-31: Experimental data for February 15, 1996 pm.....193

Figure A-32: Experimental data for February 23, 1996.....195

Figure A-33: Experimental data for February 26, 1996.....197

Figure A-34: Experimental data for February 27, 1996 am.....199

Figure A-35: Experimental data for February 27, 1996 pm.....201

Figure A-36: Experimental data for February 28, 1996.....203

Figure A-37: Experimental data for May 9, 1996; Arrhenius data at 75°C.....205

A KINETIC STUDY OF PLUTONIUM DIOXIDE DISSOLUTION IN HYDROCHLORIC ACID USING IRON (II) AS AN ELECTRON TRANSFER CATALYST

BY

KEITH WILLIAM FIFE

ABSTRACT

Effective dissolution of plutonium dioxide has traditionally been accomplished by contact with strong nitric acid (>8 *M*) containing a small amount of fluoride (<0.5 *M*) at temperatures of ~100°C. In spite of these aggressive conditions, PuO_2 dissolution is sometimes incomplete requiring additional contact with the solvent.

This work focused on an alternative to conventional dissolution in nitric acid where an electron transfer catalyst, Fe(II), was used in hydrochloric acid. The overall dissolution reaction appeared to proceed according to the following:

$$PuO_2 + 4H^+ + Fe^{+2}_{(aq)} \rightarrow Pu^{+3}_{(aq)} + 2H_2O + Fe^{+3}_{(aq)}$$

The work was an extension of an earlier investigation (Shakila et al. 1989), and used bulk electrolysis to maintain iron in the reduced state for continued reaction with the plutonium oxide surface. Cyclic voltammetry was employed as an *in-situ* analytical technique for monitoring the dissolution

The plutonium oxide selected for this study was decomposed plutonium oxalate with >95% of the material having a particle diameter <70 μm as determined by a scanning laser microscopy technique. Attempts to dry sieve the oxide into narrow size fractions prior to dissolution in the HCl-Fe(II) solvent system failed, apparently due to significant interparticle attractive forces. Although sieve splits were obtained, subsequent scanning laser microscopy analysis of the sieve fractions indicated that particle segregation was not accomplished and the individual sieve fractions retained a particle size distribution very similar to the original powder assemblage. This phenomena was confirmed through subsequent dissolution experiments on the various screen fractions which illustrated no difference in kinetic behavior between the original oxide assemblage and the sieve fractions.

Irrespective of the inability to sieve the oxide, the plutonium oxide was found to obey the classic surface reaction controlled nonporous shrinking sphere model. Arrhenius analysis of the dissolution rate data confirmed this observation and indicated an apparent activation energy for the dissolution reaction of 76.6±2.2 kJ/mol over the temperature range 28°C to 65°C, which compared favorably with previously reported values of 54 kJ/mol and 65 kJ/mol.

1 INTRODUCTION

From the recovery of plutonium associated with irradiated reactor fuel to the stabilization of legacy plutonium residues remaining from nuclear weapons production efforts, the dissolution of plutonium oxide prior to separation and purification has proven to be one of the most challenging operational problems within the entire plutonium processing sequence. From the days of the Manhattan Project to the present process flowsheet, the solvent of choice for plutonium oxide dissolution has been boiling, concentrated nitric acid containing fluoride ion. Of all of the metallic oxides capable of producing relatively concentrated solutions in acidic media, plutonium oxide has proven to be the most difficult to dissolve. Ryan and Bray (1980) were among the first to demonstrate that in low acidities (<5 *M*), plutonium oxide is practically insoluble from a thermodynamic basis. The standard free energy of the dissolution reaction in non-complexing acidic media was calculated at 41 kJ/mol, and at the boiling point was only a slightly more favorable -10.5 kJ/mol.

Improvements to the HNO_3-HF system have been suggested that replace the fluoride ion with either strong oxidants like Ce(IV) or Ag(II), or strong reductants such as Cr(II), V(II), U(III) to accomplish solubilization of the plutonium as either Pu(VI) in oxidizing dissolution or as Pu(III) in reducing dissolution. In some cases, these reagents offer significant advantages over

the conventional system, but in general, concerns about adverse impacts on downstream processing operations and current environmental regulatory guidelines definitely preclude the widespread use of many of these proposed alternatives in the United States.

1.1 Purpose of the Research

The attention given to the dissolution of PuO_2 over the past several decades by numerous researchers has been followed closely in hopes that new developments in this area would improve the overall efficiency of oxide dissolution from the wide variety of feed sources that require treatment. The recent detailed oxidative and reductive dissolution studies of Berger (1990) and Machuron-Mandard (1991) are summarized by Madic (1992), and are excellent works describing the introduction and use of electrochemistry in facilitating new approaches to PuO_2 dissolution.

Because there are a variety of matrices contaminated with chloride requiring treatment to separate and recover plutonium, there would be advantages for developing a PuO_2 dissolution technique in a chloride solvent rather than being concerned about matrix compatibility in a nitric acid system. This present study extended prior work by Shakila et al. (1989) and investigated a reductive dissolution technique for plutonium oxide using

Fe(II) in hydrochloric acid. The overall reaction describing PuO_2 dissolution in this solvent system was determined by Shakila as :

$$PuO_2 + 4H^+ + Fe^{+2}_{(aq)} \rightarrow Pu^{+3}_{(aq)} + 2H_2O + Fe^{+3}_{(aq)} \qquad (1.1)$$

In the work by Shakila, reductive dissolution continued so long as ferrous ion was present in solution. They were successful in extending the dissolution reaction by adding a reducing agent to the system, such as hydrazine, to reduce the reaction product Fe(III) to Fe(II) for continued participation in dissolution.

This study extended Shakila's observations to include continuous regeneration of the Fe(II) electron transfer catalyst by bulk electrolysis and the use of cyclic voltammetry as an *in-situ* analytical technique for measuring the progress of the dissolution reaction. An attempt was made to dry-sieve the oxide into fairly narrow particle size ranges to investigate fundamental heterogeneous reaction kinetics, and to determine the best heterogeneous reaction model describing oxide dissolution. Dry-sieving the PuO_2 used in this study failed, due to significant interparticle attractive forces. This did not, however, preclude determining that the classic surface reaction controlled nonporous shrinking sphere model very adequately and appropriately described the dissolution behavior of this system. In addition, the activation

energy of the dissolution reaction was determined by the traditional Arrhenius model and compared favorably to work completed by other investigators.

1.2 Research Goals

The goal of this research was to study the dissolution phenomena of plutonium oxide in the non-traditional HCl-Fe(II) system, and to suggest a heterogeneous model best describing the fluid-solid reaction. In addition to this overall objective, supporting work in this area included:

- evaluating bulk electrolysis for continuous regeneration of the Fe(II) electron transfer catalyst used in this reaction,
- evaluating the effectiveness of cyclic voltammetry as an *in-situ* analytical tool for monitoring the progress of the dissolution reaction,
- evaluating the fundamental nature of heterogeneous PuO_2 dissolution kinetics in this solvent system,
- presenting a general dissolution model for this particle assemblage,
- presenting an estimate of the activation energy of the dissolution reaction as obtained from analysis of the classical Arrhenius model, and

- investigating dry sieving as a method for segregating the PuO_2 assemblage into narrow size fractions for further evaluation.

2 LITERATURE REVIEW

2.1 The Plutonium-Oxygen System

The plutonium-oxygen system has previously been studied in great detail from the view of reactor fuel technology and solid state chemistry. An exhaustive presentation of this information is not necessary to meet the objective of this research, but discussion of some of the basic properties of plutonium oxide is appropriate.

With the exception of PuO, which has not been found to occur as a solid equilibrium phase, there are four plutonium-oxygen phases that have been clearly identified to date. The crystal structure and preparatory techniques of all oxides identified as separate entities are succinctly presented in Katz, Seaborg, and Morss (1986). Two of the phases correspond to stoichiometric compounds represented by $PuO_{2.00}$ (stoichiometric plutonium oxide) and $PuO_{1.50}$ (the β-Pu_2O_3 stoichiometric plutonium sesquioxide phase). The nonstoichiometric phases correspond to two hyperstoichiometric sesquioxides of the forms $PuO_{1.51}$ (α-Pu_2O_3) and $PuO_{1.61}$ (α'-Pu_2O_3); and to the substoichiometric dioxide PuO_{2-x} which extends from $PuO_{1.61}$ to $PuO_{1.98}$ depending on the oxide treatment temperature and the oxygen partial pressure. This material is closely related to $PuO_{2.00}$ but belongs in a different phase region.

Because of handling difficulties, the defect structure and nonstoichiometry of the plutonium oxides has not been studied extensively. The phase diagram of the plutonium-oxygen system as shown in Figure 2.1a is the version originally reported by Ellinger (1968) as a composite presentation of several authors. To date, the entire phase diagram is not well-established, and future work will no doubtably lead to clarifications of the tentatively proposed diagram indicated in Figure 2.1b (Naito et al. 1992).

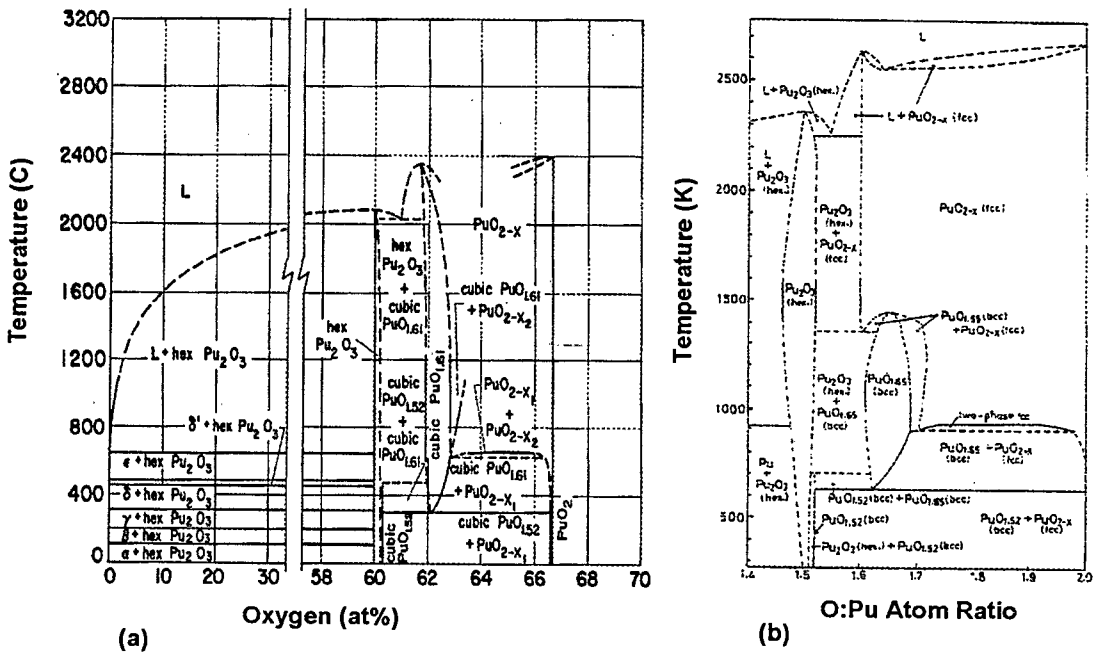

Figure 2.1. Plutonium-oxygen phase diagram; (a) from Ellinger 1968 and (b) from Naito et al. 1992 (Fig. 2.1b reprinted by permission from the American Chemical Society).

2.2 Dissolution of Plutonium Oxide

Numerous researchers have investigated the dissolution of plutonium oxide in aqueous acidic media. As discussed in Benedict, Pigford, and Levi (1981), this step is fundamentally important to the many hydrometallurgical unit operations developed for the nuclear industry. Much of the original research into understanding and improving PuO_2 dissolution has principally been directed towards empirical kinetic studies. Bjorklund and Staritzky (1954), and Gilman (1965, 1968) looked at the pretreatment and subsequent dissolution of PuO_2 under a variety of conditions including dissolution in mineral acids, after fusion, after halogenation, and in the presence of complexing agents. Nitric-hydrofluoric acid has been recognized as the classical industrial plutonium oxide dissolution process with only limited investigations into the alternative hydrochloric acid system (Molen 1967, Crossley and Milner 1969, Bray et al. 1986, Shakila et al. 1989).

Uriarte and Rainey (1965) looked at the dissolution behavior of UO_2, PuO_2 and mixed UO_2-PuO_2 in nitric acid with and without redox or complexing reagents. Other basic studies have also been conducted evaluating the importance of fluoride to successful dissolution (Barney 1976, Tallent and Mailen 1977a, 1977b), while others studied thoria dissolution in hopes it would lead to a better understanding of the plutonia dissolution phenomena (Shying et al. 1970, 1972). Some researchers studied the effect of various

promoters in combination with fluoride to improve dissolution performance (Uriarte and Rainey 1965, Harmon 1975a, 1975b). An electrolytic dissolution procedure using electron transfer catalysts was developed for rapid and complete oxide dissolution in nitric acid systems (Bray and Ryan 1982, Wheelwright et al. 1988, Berger 1992, Ryan et al. 1992).

Ryan and Bray (1980), in their historical review of PuO_2 dissolution, were the first to attempt explain, from a thermodynamic viewpoint, the relative insolubility of plutonium oxide in noncomplexing acid media by calculating the free energy of reaction. In low acidities (<5 *M*), they calculated the standard free energy of the dissolution reaction to be ΔG^0_{298} = 41 kJ/mol, and at the acid boiling point to be only slightly more favorable at ΔG_{373} = -10.5 kJ/mol. As part of a study to systematically evaluate the dissolution behavior of several different actinide oxides, Berger (1990) utilized carbon paste electrochemical techniques and considered the following general dissolution mechanisms for PuO_2:

- with no redox reaction, producing the Pu(IV) species in solution,
- by oxidation, producing either Pu(V) or Pu(VI), and
- by reduction, producing Pu(III).

From Berger (1990) and Madic (1992), only the reductive dissolution path appears thermodynamically favorable in noncomplexing acidic media

(Table 2.1); although oxidation leading to Pu(V) and Pu(VI) can be theoretically observed for electrochemical electrode potentials higher than 1.43 V and 1.22 V respectively, vs. the normal hydrogen electrode (NHE). It should be noted, however, that all of these plutonium redox products have been previously produced by chemical or electrochemical methods.

Table 2.1: Thermodynamic Data for the Dissolution of PuO_2, (Berger 1990)

Reaction	ΔG^0_{298} **(kJ/mol)**
$PuO_2(s) \rightarrow Pu^{+4}(aq)$	32.4 ($\pm$4.00)
$PuO_2(s) \rightarrow Pu^{+3}(aq)$	-64.96 ($\pm$4.00)
$PuO_2(s) \rightarrow PuO_2^{+}(aq)$	138.27 ($\pm$9.79)
$PuO_2(s) \rightarrow PuO_2^{+2}(aq)$	236.19 ($\pm$15.40)

In spite of the pessimistic thermodynamic data presented in Table 2.1, dissolution of PuO_2 is practiced on a daily basis using fluoride complexation equilibria to shift the thermodynamics presented in Table 2.1 into a favorable region and achieving effective solubilization of Pu(IV).

2.2.1 PuO_2 Dissolution Without Redox

Numerous acid media have been recommended for the dissolution of PuO_2 without changing the plutonium valance state. As described in Crossley and Milner (1969), Dahlby et al. (1975), and Machuron-Mandard (1991), these procedures have been limited to the analytical field and generally require extreme physicochemical conditions to achieve effective dissolution of the PuO_2 (concentrated HCl and HNO_3 at 100°C to 300°C and pressures as high as 4000 psig; concentrated HCl and $HClO_4$ or H_2SO_4 at 300°C; or H_3PO_4 at 200°C).

From Ryan and Bray (1980), nitrate ion in solution leads to the complexing equilibria of Pu(IV); and in the presence of high concentrations of nitric acid, the Pu(IV) complexation is sufficient to produce moderately favorable thermodynamics for the overall PuO_2 dissolution reaction. Considering only Pu(IV) and $Pu(NO_3)^{+3}$ as soluble species, they calculated the solubility of PuO_2 at 100°C (Figure 2.2). The solubility limits reported for high nitric acid concentrations are lower than real values, however, since plutonium nitrate complexes with higher valence states of plutonium were not considered in the theoretical presentation.

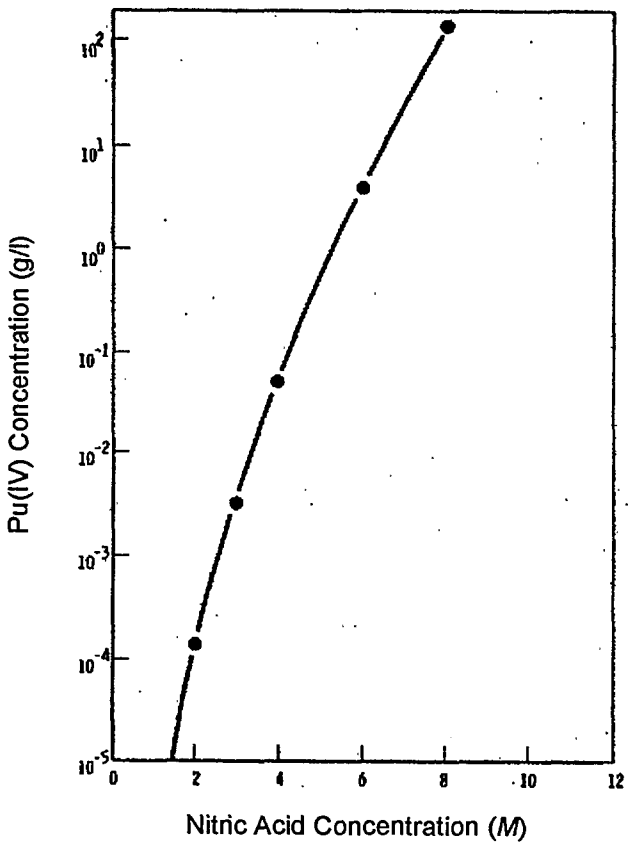

Figure 2.2. Theoretical solubility of PuO_2 in nitric acid (Ryan and Bray 1980; reprinted by permission from the American Chemical Society).

The majority of studies on the dissolution of PuO_2 in nitric-hydrofluoric acid did not include detailed thermodynamic analysis; and only elaborated on the beneficial role played by the fluoride ion. Besides its strong ability to form highly stable complexes with Pu(IV), evidently enhancing the dissolution thermodynamics, fluoride ion was also thought to promote a fundamentally different oxide surface reaction mechanism than the one observed in pure

nitric acid, thereby causing increased reaction kinetics. Work on describing the interaction of fluoride with the plutonium oxide during nitric-hydrofluoric acid dissolution was completed by Barney (1976) and Tallent (1977a).

2.2.2 Oxidative PuO_2 Dissolution

In an attempt to improve PuO_2 dissolution kinetics and move away from the aggressive nature of the boiling nitric-hydrofluoric acid solvent, industrial improvements led to the implementation of redox chemistry. Wilson (1961) and later Uriarte and Rainey (1965) and Harmon (1975a and 1975b), investigated the use of Ce(IV) as a promoter to enhance the performance of the nitric-hydrofluoric acid process. This reagent was successful because the Ce(IV)-Ce(III) half-cell potential (1.61 V vs. NHE in 1.0 *F* HNO_3) was higher than the potential required to oxidize Pu(IV) to either Pu(V) or Pu(VI). These values were determined by Berger (1990) to be 1.43 V and 1.22 V vs. NHE, respectively.

Other oxidative reagents have been evaluated for PuO_2 dissolution or the destruction of plutonium-contaminated organic materials using the Ag(II)-Ag(I) couple (1.929 V vs. NHE in 4 *F* HNO_3) reported by Berger (1990), Ryan et al. (1992), and Zawodzinski et al. (1993); and the Co(III)-Co(II) couple (1.85 V vs. NHE in 4 *F* HNO_3) reported by Zawodzinski (1996). CEPOD, as discussed by Ryan et al. (1992), is an acronym for Catalyzed

Electrochemical Plutonium Oxide Dissolution and was developed to dissolve PuO_2 by oxidizing Pu(IV) from the oxide crystal lattice to form the more soluble PuO_2^{+2}. Successful CEPOD solvents contain catalytic amounts of elements that form kinetically fast, strongly oxidizing ions that can be continuously regenerated at an electrochemical anode. In their oxidized form, the catalysts offering the most promise include Ag(II), Ce(IV), Co(III), and AmO_2^{+2}.

2.2.3 Reductive PuO_2 Dissolution

An early example of reductive dissolution was found in Bjorklund and Staritzky (1954), where they observed the rapid dissolution of PuO_2 in a mixture of hydrochloric acid and potassium iodide. Until recently, other studies involving reductive dissolution have been practically nonexistent. Berger (1990) estimated the standard potential of the $PuO_2(s)/Pu^{+3}(aq)$ couple to be +0.67 V vs. NHE; and Machuron-Mandard (1991), extended this work to examine the reductive dissolution of PuO_2 using the Cr(II)/Cr(III) couple in sulfuric acid media (-0.42 V vs. NHE). Shakila et al. (1989) examined the reductive dissolution of PuO_2 in hydrochloric media using ferrous ion as an electron transfer catalyst. Although the Fe(II)/Fe(III) couple is reported as 0.732 V vs. NHE in 1 *F* HCl, it was found to be approximately 0.55 V vs. NHE in 7 *M* HCl (according to anodic peak height measurements

from the cyclic voltammograms generated in this present study). In Shakila's work, the oxide dissolution reaction proceeded vigorously as long as Fe(II) was present in solution. They also observed that the use of a reducing agent (hydrazine) in conjunction with Fe(II) prolonged the dissolution rate supposedly due to reduction of the Fe(III) product back to the Fe(II) reactant thereby continuing the reduction of Pu(IV) to the more soluble Pu(III). In an earlier investigation, Shakila et al. (1987) also observed that hydrazine led to improved PuO_2 dissolution in the HNO_3-HF system.

2.3 Heterogeneous Reaction Systems

2.3.1 PuO_2 Dissolution Kinetics

Although several basic studies have been conducted attempting to evaluate the dissolution kinetics of PuO_2 in HNO_3-HF, the principle conclusion from the past work was that very little agreement among the various researchers existed regarding the effect of various parameters on the dissolution rate. There was certain agreement that oxide surface area, fluoride concentration, nitric acid concentration, and solvent-to-oxide ratio were of primary importance at a given temperature (usually 100°C). It was also generally concluded that as the PuO_2 dissolution proceeded, the rate

decreased as free fluoride was complexed with Pu(IV) or consumed by other parasitic side reactions. As discussed previously, Ryan and Bray (1979), presented a fairly comprehensive review of plutonium dioxide dissolution in the nitric acid system using fluoride ion in conjunction with several reaction promoters.

Uriarte (1965) found the dissolution rate of PuO_2 to increase by the 1.4^{th} power of HF molarity at constant acidity and by the 4th power of the total HNO_3 molarity. Barney (1976) found the rate to be first order in the total HF not complexed by Pu(IV); first order in oxide surface area, and independent of acid concentration in the range 4 *M* to 12 *M*. He also found the dissolution rate to decrease with the amount of PuO_2 dissolved because fluoride was complexed with Pu(IV) in solution. This effect increased with decreasing acidity due to the formation of higher fluoro complexes at lower acidities. Tallent and Mailen (1977a, 1977b) also found the rate to be first order in uncomplexed HF concentration and found the rate to be first order in mean ionic activity of HNO_3 (second order if fluoride ion instead of HF was the reacting species). They also recognized that the rate decreased as the fluoride was complexed by Pu(IV) and performed experiments to eliminate this effect by oxidizing the Pu(IV) to Pu(VI), which forms a much weaker fluoro complex.

Despite the rather wide differences in conclusions with regard to the effect of acidity on dissolution rate, the values of the *initial* rate from these studies were in rather good agreement for dissolution in 8 *M* to 10 *M* HNO_3-0.05 *M* HF at 100°C; all in the range of $1 \cdot 10^{-3}$ to $9 \cdot 10^{-3}$ mg PuO_2 min^{-1}-cm^{-2}. Tallent and Mailen (1977a) indicated that the dissolution of PuO_2 followed a mechanism similar to a thoria dissolution mechanism proposed by Shying et al. (1972), and that the rate controlling step for PuO_2 dissolution involved the reaction of protons and fluoride ions with the fluorinated PuO_2 surface sites.

$$PuOF + F^- + 2H^+ \rightarrow PuF_2^{+2} + H_2O + e^- \tag{2.1}$$

Tallent and Mailen (1977a) suggested that if PuO_2 dissolution followed the thoria dissolution mechanism proposed by Shying et al. (1972), the PuF_2^{+2} complex would dissociate in solution and the electron would re-adsorb or react with the remaining PuO_2 surface sites as the first step in continued dissolution.

Considering the dissolution of thoria in HNO_3-HF (which is chemically similar to PuO_2); Takeuchi et al. (1971) found the dissolution rate of the ThO_2 to be less than first order in HF concentration and proportional to

$$\frac{K_1[HF]}{1+K_1[HF]} \tag{2.2}$$

where K_1 was determined empirically.

This observation was found to be accurate in the HF concentration range 0.01 *M* to 0.05 *M* where ThO_2 dissolution was found to be first order in uncomplexed HF concentration. Takeuchi also found a small dependence on total acidity of the same form

$$\frac{K_2[HNO_3]}{1+K_2[HNO_3]} \tag{2.3}$$

where K_2 was also determined empirically.

Barney (1976) had previously found a similar result for the dissolution of PuO_2.

In severe contrast to the work completed in the nitric acid system, there has been relatively little attention paid to other solvent systems. Molen (1967) compared the dissolution behavior of PuO_2 in HNO_3-CaF_2 to the dissolution of PuO_2 in the HCl-$SnCl_2$ system and found generally a better performance by the HCl solvent. His work was semi-quantitative, however, and illustrated oxide dissolution behavior graphically as a function of particle surface area, solid-to-liquid ratio, and mean crystallite size.

Bray et al. (1986) extended work from the nitric acid system to the HCl system and included mixtures of HCl-CaF_2 where they also found that the dissolution rate of the oxide decreased markedly as the calcination temperature of the oxide increased. They also, however, observed acceptable dissolution performance in boiling HCl that contained varying

molar ratios of fluoride-to-plutonium. Oxide fired to ~1700°C was essentially completely dissolved in 3 hours with a fluoride-to-plutonium molar ratio of 2; whereas oxide fired to only 950°C was completely dissolved in ~1 hour at a fluoride-to-plutonium molar ratio of 1.8.

As previously discussed, there has been a remarkable lack of research into reductive PuO_2 dissolution with the exception of work by Shakila et al. (1989) who looked at the dissolution of plutonium oxide in the presence and absence of reducing agents at solution temperatures of ~100°C; and recent work by Machuron-Mandard (1991), where the reductive dissolution of PuO_2 was studied in a dilute solution of H_2SO_4-Cr(II) at 55°C to 65°C.

Shakila's results indicated that the addition of hydrazine increased the dissolution of oxide even at low acidities, and the presence of low concentrations of Fe(II) were sufficient to complete PuO_2 dissolution in approximately 2 hours. Their work showed that dissolution appeared to stop when all of the Fe(II) was converted to Fe(III) and also showed the reaction could be extended by using hydrazine to convert the iron back to the +2 oxidation state. As a result of their study, they proposed the following overall dissolution reaction for the HCl-Fe(II) system as presented previously:

$$PuO_2 + 4H^+ + Fe^{+2}_{(aq)} \rightarrow Pu^{+3}_{(aq)} + 2H_2O + Fe^{+3}_{(aq)} \qquad (1.1)$$

Similarly, Machuron-Mandard examined the reductive dissolution of PuO_2 in the H_2SO_4-Cr(II) system. As with iron in Shakila's research, the chromium electron transfer catalyst was added in the reduced state and allowed to spontaneously reduce plutonium according to the following reaction:

$$PuO_2 + 4H^+ + Cr^{+2}_{(aq)} \rightarrow Pu^{+3}_{(aq)} + 2H_2O + Cr^{+3}_{(aq)} \tag{2.4}$$

Machuron-Mandard, however, did evaluate the effect of agitation, Cr(II) concentration, PuO_2 surface area, temperature, and proton concentration on the overall dissolution rate. He concluded the empirical rate law for dissolution in the H_2SO_4-Cr(II) system took the form:

$$v = 1.8 \cdot 10^4 \cdot S \cdot \exp\left[\frac{(-6.5\pm5)\cdot10^3}{RT}\right] \cdot \left[H^+\right]^{(0.4\pm0.1)} \tag{2.5}$$

where:

v is the dissolution rate (mol PuO_2/sec),

S is the BET (Brunauer, Emmett, and Teller) surface area (m^2/g),

R is the gas constant (8.314 j/mol-K),

T is the absolute temperature (K), and

$\left[H^+\right]$ is the proton concentration (*M*).

2.3.2 Noncatalytic Fluid-Solid Reactions

The majority of models for fluid-solid reactions were originally developed based on the simplifying assumption of a nonporous reactant, even when the reactant was known to contain considerable porosity. This simplification may confound data interpretation, but it is generally the approach taken by many researchers when studying a new reaction system. An important characteristic of nonporous solid reactions is that chemical reaction and mass transport are coupled in series. Since the chemical reaction occurs at the planar surface of the solid, the surface always appears as one of the boundary conditions in the mass transport equations. This makes analysis of the nonporous solid systems easier than the analysis of porous solid systems.

The simplest system in fluid-solid reactions is that of a shrinking nonporous particle that forms no solid product layer:

$$aA_{fluid} + bB_{solid} \rightarrow cC_{fluid} \tag{2.6}$$

Figure 2.3 illustrates the reaction schematically.

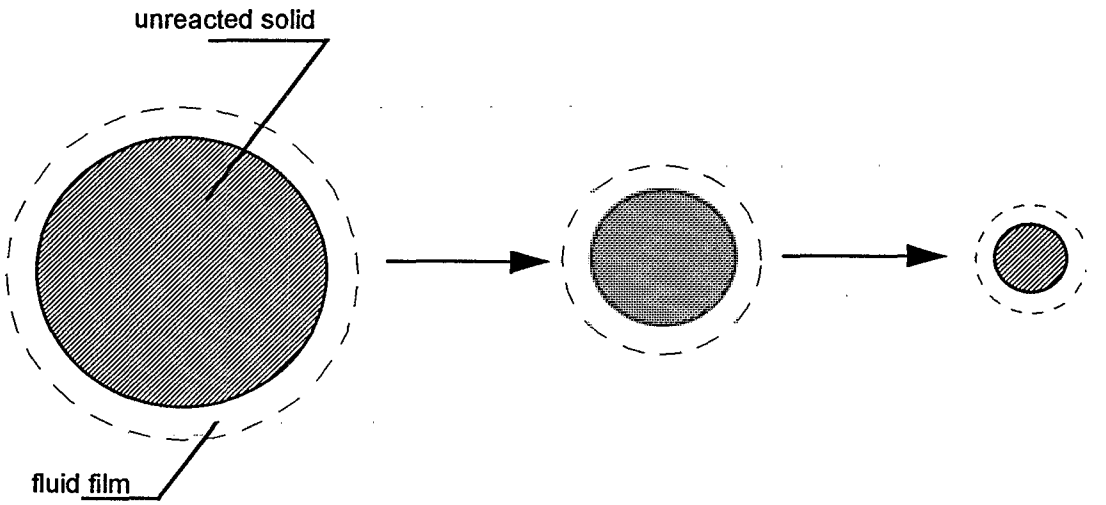

Figure 2.3. Representation of a nonporous solid reacting with a fluid in which no solid product is formed.

In many situations, these nonporous fluid-solid interactions are accurately approximated by first-order reactions. The rate expression obtained for the reaction is determined from the rate limiting step based on the sequence of actions found in Table 2.2 and generally takes a form similar to

$$\frac{dA}{dt} = k[C_A^n - (C_C^m / K_E)] \tag{2.7}$$

where $\frac{dA}{dt}$ is the disappearance of A by surface chemical reaction,

k is the heterogeneous rate constant,

C_A and C_C are the fluid reactant and product concentrations, respectively, at the reaction surface, and

K_E is the equilibrium constant.

When the reaction orders $n = m = 1$, and the reaction is irreversible (as most fluid-solid reactions are), the rate becomes first order. This, in addition to its mathematical simplicity, is why first order kinetics are frequently used for describing many types of fluid-solid reactions.

Table 2.2. Rate-Limiting Mechanisms for Nonporous Fluid-Solid Reactions

Progressive Step	Rate-Limiting Mechanism
1	Diffusion of the fluid reactants across the fluid film surrounding the solid.
2	Adsorption of the fluid reactants at the solid reactant surface.
3	Chemical reaction with the solid surface.
4	Desorption of the fluid products from the solid reaction surface.
5	Diffusion of the fluid products away through the fluid film surrounding the solid.

Development of the following general models considers both porous and nonporous fluid-solid reactions and are some examples of the variety and complexity of models available for examining reaction systems in this area. These examples consider isothermal systems of spherical particles reacting with first order kinetics at quasi-steady state to produce only fluid products.

2.3.2.1 Nonporous Shrinking Spherical Particle–Surface Chemical Reaction Control

For a nonporous (large) shrinking spherical particle under chemical reaction control, the conversion-time relationship originally given by Wen (1968) and Levenspiel (1972) is:

$$\frac{t}{\tau_{rxn}} = 1-(1-X)^{1/3} \tag{2.8}$$

where $\tau_{rxn} = \dfrac{\rho_B R}{b k_s C_{Af}}$ = time for complete particle conversion

ρ_B = molar density of species B in the solid material (mol/cm^3),

R = initial particle radius (cm),

b = stoichiometric ratio (moles of solid reacted per mole of fluid reactant),

k_s = first order rate constant for the surface reaction (cm/sec),

C_{Af} = bulk solution concentration of species A (mol/cm^3), and

X = fractional particle conversion (dimensionless).

This result can be developed assuming that the following general reaction describes the dissolution process:

$$aA_{fluid} + bB_{solid} \rightarrow cC_{fluid} \tag{2.6}$$

The amount of B_{solid} present in a sphere of radius R is

$$N_B = \rho_B V = \rho_B \tfrac{4}{3}\pi R^3 \tag{2.9}$$

where ρ_B = molar density of species B (mole/cm^3),

R = the initial radius of the unreacted core (cm), and

V = the volume of the sphere containing species B (cm^3).

As dN_B moles of solid reactant disappear, the decrease in volume or radius of the unreacted core is given by

$$-dN_B = -bdN_A = -\rho_B dV = -\rho_B d(\tfrac{4}{3}\pi r^3) = -4\pi\rho_B r^2 dr \tag{2.10}$$

where r is the radius of the unreacted core at any time.

The decrease in solid reactant B is controlled by the rate of surface chemical reaction and is proportional to the available surface area of the reacting particle. In this reaction, film diffusion is fast compared to the surface reaction, thus, dN_B is dependent on the available surface of the unreacted particle, and the a rate of reaction is given by

$$-\frac{1}{4\pi r^2}\frac{dN_B}{dt} = -\frac{b}{4\pi r^2}\frac{dN_A}{dt} = bk_s C_{Af} \tag{2.11}$$

And by combining Eq. 2.10 and 2.11, the rate of reaction in terms of the shrinking particle radius can be written as

$$-\frac{1}{4\pi r^2}(4\pi\rho_B r^2)\frac{dr}{dt} = bk_s C_{Af} = -\rho_B \frac{dr}{dt} \tag{2.12}$$

integrating

$$-\rho_B \int_R^r dr = bk_s C_{Af} \int_o^t dt \tag{2.13}$$

$$t = \frac{\rho_B}{bk_s C_{Af}}(R - r) \tag{2.14}$$

At $r = 0$, the reaction is complete; therefore, the time for complete reaction τ_{rxn}, is given by

$$\tau_{rxn} = \frac{\rho_B R}{bk_s C_{Af}} \tag{2.15}$$

and

$$\frac{t}{\tau_{rxn}} = 1 - \frac{r}{R} \tag{2.16}$$

Since the fractional conversion X is given by the volume change in the particle

$$X = \frac{\frac{4}{3}\pi R^3 - \frac{4}{3}\pi r^3}{\frac{4}{3}\pi R^3} = 1 - \frac{r^3}{R^3} \tag{2.17}$$

or

$$\frac{r}{R} = (1 - X)^{1/3} \tag{2.18}$$

Therefore, the general form of the relationship for a nonporous shrinking spherical particle governed by surface chemical reaction results in Eq. 2.8.

$$\frac{t}{\tau_{rxn}} = 1 - (1 - X)^{1/3} \tag{2.8}$$

2.3.2.2 Nonporous Shrinking Spherical Particle–Diffusion Control for Small Particles in the Stokes' Law Regime

For a nonporous (small) shrinking spherical particle in the Stokes' law regime, the fluid dynamics of the system are quiescent and laminar with a Reynolds number less than one. In this case, the experimental drag force for a sphere is the same as the theoretical Stokes' law equation. Essentially this fluid-solid system is unmixed and film diffusion controls the reaction. For this system, the conversion-time relationship becomes (Levenspiel 1972):

$$\frac{t}{\tau_{spf}} = 1-(1-X)^{2/3} \tag{2.19}$$

where $\tau_{spf} = \dfrac{\rho_B R^2}{2bC_{Af}D_e}$ = time for complete particle conversion

D_e = effective diffusivity in the fluid film surrounding the particle (cm^2/sec) and definitions for the other parameters are given in section 2.3.2.1.

Levenspiel (1972) illustrates the development of this relationship from previously correlated mass transfer relationships. Film resistance to mass transfer at a particle surface will be dependent on many factors; fluid and particle velocity, particle size, and various fluid properties. An example of an applicable mass transport correlation for a component of mole fraction y in a fluid to free-falling solids is given by Ranz and Marshall (1952)

$$\frac{k_g d_p}{D_e} = 2 + 0.6(Sc)^{1/3}(\mathrm{Re})^{1/2} = 2 + 0.6\left(\frac{\mu}{\rho D_e}\right)^{1/3}\left(\frac{d_p \rho u}{\mu}\right)^{1/2} \tag{2.20}$$

where

k_g = fluid phase mass transfer coefficient (cm/sec),

d_p = particle diameter (cm),

Sc = Schmidt number = $\frac{\mu}{\rho D_e}$ (dimensionless),

Re = Reynolds number = $\frac{d_p \rho u}{\mu}$ (dimensionless),

ρ = mass density (g/cm^3),

μ = fluid viscosity (g/cm sec), and

u = fluid velocity (cm/sec).

At the time when a nonporous spherical particle originally of radius R has reacted and shrunk to size r, the molar flux of the solid reactant is

$$dN_B = \rho_B dV = 4\pi\rho_B r^2 dr \tag{2.21}$$

Analogous to the surface reaction control development (Eq. 2.11), the amount of material reacting is proportional to the available surface of the unreacted particle. Since fluid film diffusion controls the reaction, the gradient of the fluid reactant concentration between the bulk fluid phase and the particle surface is the driving force for the reaction. This can be further simplified recognizing that the reactant concentration at the particle surface

is zero due to the speed of the surface reaction relative to mass transfer ($k_s >> k_g$). Combining Eq. 2.21 with the mass transfer analog to Eq. 2.11 results in

$$-\frac{1}{4\pi r^2}\frac{dN_B}{dt} = -\frac{\rho_B 4\pi r^2}{4\pi r^2}\frac{dr}{dt} = -\rho_B \frac{dr}{dt} = bk_g(C_{Af} - C_{As}) = bk_g C_{Af} \tag{2.22}$$

where C_{As} is the fluid reactant concentration at the particle surface.

For a fluid-particle reaction taking place in the Stokes' law regime, the fluid velocity and the particle diameter are sufficiently small and Eq. 2.20 reduces to

$$k_g = \frac{2D_e}{d_p} = \frac{D_e}{r} \tag{2.23}$$

Combining Eq. 2.22 and 2.23 and integrating produces

$$-\rho_B \frac{dr}{dt} = \frac{bD_e C_{Af}}{r} \Rightarrow -\int_R^r r dr = \frac{bD_e C_{Af}}{\rho_B}\int_0^t dt \tag{2.24}$$

and

$$\frac{R^2 - r^2}{2} = \frac{bD_e C_{Af} t}{\rho_B} \tag{2.25}$$

At $r = 0$, $t = \tau_{spf}$; the time for complete disappearance of the particle

$$\tau_{spf} = \frac{\rho_B R^2}{2bD_e C_{Af}} \tag{2.26}$$

Therefore

$$\frac{t}{\tau_{spf}} = 1 - \left(\frac{r}{R}\right)^2 \tag{2.27}$$

And employing Eq. 2.18 resulted in the time-conversion relationship

$$\frac{t}{\tau_{spf}} = 1 - (1 - X)^{2/3} \tag{2.19}$$

2.3.2.3 Nonporous Shrinking Spherical Particle–Diffusion Control for Large Particles with Initially High Reynolds Number

In a system where the fluid dynamics produce initially a high Reynolds number around a large, nonporous, shrinking spherical particle controlled by film diffusion, the conversion-time relationship previously given by Levenspiel (1972) is:

$$\frac{t}{\tau_{lpf}} = 1 - (1 - X)^{1/2} \tag{2.28}$$

where $\tau_{lpf} = \dfrac{(const)R^{3/2}}{C_{Af}}$ = time for complete particle conversion.

Development of this diffusion control model is similar to the model developed for diffusion control in the Stokes' law regime. In the Stokes' law regime

$$k_g \propto \frac{1}{d_p} \qquad \text{for small } d_p \text{ and } u \tag{2.29}$$

while for larger particles with an initially high Reynolds number

$$k_g \propto \frac{u^{1/2}}{d_p^{1/2}} \qquad \text{for large } d_p \text{ and } u \tag{2.30}$$

For this situation

$$k_g = \frac{const}{d_p^{1/2}} = \frac{const}{r^{1/2}} \tag{2.31}$$

The constant in Eq. 2.31 can be evaluated from the mass transfer correlation used in the development (Eq. 2.20 for example). At a high Reynolds number, Eq. 2.20 reduces to

$$k_g = \frac{0.6D_e\left(\frac{\mu}{\rho D_e}\right)^{1/3}\left(\frac{d_p \rho u}{\mu}\right)^{1/2}}{d_p} = \frac{const}{d_p^{1/2}} \tag{2.32}$$

This result can be used in the development of Eq. 2.28, by following a procedure similar to the one previously performed in Section 2.3.2.2,

$$-\rho_B \frac{dr}{dt} = \frac{bC_{Af}(const)}{r^{1/2}} \Rightarrow -\int_R^r r^{1/2} dr = C_{Af}(const)\int_0^t dt \tag{2.33}$$

and

$$R^{3/2} - r^{3/2} = C_{Af}(const)t \tag{2.34}$$

At $r = 0$, $t = \tau_{lpf}$; the time for complete disappearance of the particle

$$\tau_{lpf} = const\frac{R^{3/2}}{C_{Af}} \tag{2.35}$$

Therefore

$$\frac{t}{\tau_{lpf}} = 1 - \left(\frac{r}{R}\right)^{3/2} \tag{2.36}$$

And again employing Eq. 2.18 results in the time-conversion relationship

$$\frac{t}{\tau_{lpf}} = 1 - (1 - X)^{1/2} \tag{2.28}$$

2.3.2.4 Uniformly Reacting Porous Spherical Particle–Surface Chemical Reaction Control

Peterson (1957) and Sohn (1976) studied the involved nature of noncatalytic heterogeneous reactions in an initially porous particle, and although there are several extensions to this general model (Ishida and Wen 1968, 1971, Park and Levenspiel 1975, Szekely et al. 1976), the following is presented only as a representative example of the rigor of some of these heterogeneous fluid-solid models.

For uniformly reacting porous particles where the fluid species can penetrate deeply into the interior of the solid prior to reacting (chemical reaction controlling), the rate of reaction per unit volume is given by (Sohn 1976):

$$R(v) = kC_A^n \left(\frac{\varepsilon_0}{r_0}\right) \frac{(2G - 3\varsigma)\varsigma}{G - 1} \tag{2.37}$$

and the relationship between conversion and time is

$$X = \frac{\varepsilon_0}{1-\varepsilon_0}\left[\left(1+\frac{t}{\tau}\right)^2\left(\frac{G-1-\frac{t}{\tau}}{G-1}\right)-1\right] \tag{2.38}$$

where k = fluid-solid reaction rate constant (cm/sec),

$\varsigma = r / r_0$

ε_0 = initial porosity of the solid (dimensionless),

r_0 = initial radius of pores (cm),

r = pore radius at any time (cm),

C_A = molar concentration of reactant A (mol/cm^3),

$G = 3\pi L / K r_0$,

L = total length of the pore system per unit volume defined as the centerline distances of the individual pores,

K = characteristic constant depending on the number of pore intersections per unit volume and the angles at which they intersect,

$\tau = \frac{r_0 \rho_s}{bkC_A^n}$ = time for complete particle conversion (sec),

ρ_s = molar density of the pore-free solid (moles/cm^3),

b = stoichiometric ratio (moles of solid reacted per mole of fluid reactant), and

n = order of reaction.

For the general reaction described by Eq. 2.6, and governed by chemical reaction control, the rate of reaction per unit volume of porous solid is given by

$$\left(\frac{\rho_s S_v}{b}\right)\frac{dr}{dt} = \frac{\rho_s}{b}\frac{d\varepsilon}{dt} \Rightarrow S_v = \frac{d\varepsilon}{dr} \tag{2.39}$$

where

S_v = surface area to volume ratio of the solid (cm^{-1}), and

ε = porosity of the solid at any time.

and recognizing as well that

$$\frac{dr}{dt} = \frac{bk}{\rho_s} C_A^n \tag{2.40}$$

To solve Eq. 2.39, a relationship for the surface area to volume ratio and the pore radius is necessary. In the original development, Petersen (1957) considers a porous solid represented by an idealized network of cylindrical pores with random intersections; and for a constant concentration of fluid reactant, the cylindrical pore radii increase uniformly from r_0 to r. After geometric considerations and assuming that no new pores are created, the relationship for surface area becomes

$$S_v = 2\pi r L - K r^2 \tag{2.41}$$

where L is the total length of the pore system per unit volume, and

K is a characteristic constant depending on the number of pore intersections per unit volume and the angles at which the poles intersected each other.

From Eq. 2.39 and Eq. 2.41

$$\varepsilon = \int_0^r (2\pi rL - Kr^2)dr = \pi Lr^2 - \frac{K}{3}r^3 \tag{2.42}$$

When $r = r_0$, $\varepsilon = \varepsilon_0$, therefore

$$\frac{\varepsilon}{\varepsilon_0} = \frac{\pi Lr^2 - (K/3)r^3}{\pi Lr_0^2 - (K/3)r_0^3} = \varsigma^2\left(\frac{G-\varsigma}{G-1}\right) \tag{2.43}$$

As defined earlier, $\varsigma = r/r_0$ and G is determined to be $3\pi L/Kr_0$ by rearranging terms in Eq. 2.43. Recognizing that as $\varepsilon \to 1$, $S_v \to 0$. By combining Eq. 2.39 and 2.43, the surface area relationship S_v becomes

$$S_v = \frac{d\varepsilon}{r_0 d\varsigma} = \frac{\varepsilon_0}{r_0}\frac{(2G-3\varsigma)\varsigma}{G-1} \tag{2.44}$$

For $S_v = 0$ at $\varepsilon = 1$, the term $2G - 3\varsigma = 0$ at $\varepsilon = 1$. Therefore

$$\varsigma\big|_{\varepsilon=1} = \frac{2G}{3} \tag{2.45}$$

Upon combining Eq. 2.45 with Eq. 2.43 results in $G = G(\varepsilon_0)$ only; and can be reduced to

$$\frac{4\varepsilon_0 G^3}{27} - G + 1 = 0 \tag{2.46}$$

And combining Eq. 2.38 with Eq. 2.43 produces

$$kS_vC_A^n = kC_A^n(\frac{\varepsilon_0}{r_0})\frac{(2G-3\varsigma)\varsigma}{G-1} \tag{2.47}$$

which was initially presented as Eq. 2.37.

A relationship between conversion and time can be developed by first integrating Eq. 2.40

$$\frac{dr}{dt} = \frac{bk}{\rho_s}C_A^n \Rightarrow \int_{r_0}^{r} dr = \frac{bkC_A^n}{\rho_s}\int_0^t dt \Rightarrow r - r_0 = \frac{bkC_A^n t}{\rho_s} \Rightarrow \frac{r}{r_0} - 1 = \frac{bkC_A^n t}{r_0\rho_s} \tag{2.48}$$

Since

$$\frac{r}{r_0} = \varsigma = 1 + \frac{t}{\tau} \tag{2.49}$$

where $\tau = \frac{r_0\rho_s}{bkC_A^n}$, the total time for conversion of the porous solid.

Since during the reaction, porosity is developed and continues to increase as the reaction proceeds; the void space in the initial solid ranges from 0 to 1. Conversion of the solid can be described as

$$X = \frac{\varepsilon - \varepsilon_0}{1-\varepsilon_0} \Rightarrow \frac{X(1-\varepsilon_0)}{\varepsilon_0} = \frac{\varepsilon}{\varepsilon_0} - 1 \Rightarrow X = \frac{\varepsilon_0}{1-\varepsilon_0}\left(\frac{\varepsilon}{\varepsilon_0} - 1\right) \tag{2.50}$$

Combining Eq. 2.43 and Eq. 2.49 into the final result of Eq. 2.50 produces the final conversion and time relationship

$$X = \frac{\varepsilon_0}{1-\varepsilon_0}\left[\left(1+\frac{t}{\tau}\right)^2\left(\frac{G-1-\frac{t}{\tau}}{G-1}\right) - 1\right] \tag{2.38}$$

2.3.2.5 Concluding Remarks

In considering these examples of model development, they only begin to illustrate the different levels of simplicity leading to complexity that have been utilized in describing heterogeneous fluid-solid reactions. Wen (1968) supports the philosophy of inspecting simple, but applicable models before developing complex ones.

He qualitatively describes the situation of uncatalyzed heterogeneous fluid-solid reaction controlled by surface chemical reaction control as depending on the rate limiting mechanism selected, the resulting rate equation may involve more than two arbitrary constants, and sometimes as many as seven. In selecting the constants for each mechanism, the curve representing the rate equation is chosen to best fit of the experimental data. But because of intrinsic scatter in the data, however, little meaning can be attributed to many of the constants; and often, the difference in fit between competitive rate expressions is so slight that it can be difficult to determine whether the difference is due to experimental error or due truly to a difference in mechanism.

Although an alternative mechanism may fit the data equally well, the new model may require additional experimentation to confirm the true mechanism. He concluded that although an understanding of the true mechanism would allow for extrapolation beyond the region of investigation;

there are no reasons why simple rate equations fitting the data satisfactorily should not be used provided no extrapolation beyond the original range of investigation is allowed.

2.4 Effect of Temperature on the Rate Determining Step

Generally, for liquid-phase heterogeneous reactions controlled by diffusional processes, the activation energy is low with values ranging between 10 kJ/mol and 20 kJ/mol (Habashi 1969, Terry 1983, Machuron-Mondard 1990). For reactions controlled by chemical reaction at the particle surface, however, values of the apparent activation energy are generally greater than 40 kJ/mol. In liquid solutions, this is due to the linear dependence of the diffusion coefficient with temperature, and can be described by semi-empirical correlations such as the Stoke's-Einstein equation or the Wilke-Chang relationship (Geankoplis 1983). In contrast, the chemical reaction rate constant is exponentially dependent on temperature as illustrated by the Arrhenius relationship.

Stokes-Einstein equation: $$D_{AB} = \frac{9.96 \cdot 10^{-16} T}{\mu V_A^{0.333}} \tag{2.51}$$

where D_{AB} is the diffusivity of solute A in solvent B (cm^2/sec),

T is the absolute temperature (°K),

μ is the solution viscosity (kg/m·sec), and

V_A is the solute molar volume at its normal boiling point (m^3/kg mol).

Wilke-Chang correlation: $$D_{AB} = 1.173 \cdot 10^{-16} (\varphi M_A)^{0.5} \frac{T}{\mu_B V_A^{0.6}} \tag{2.52}$$

where φ is an "association parameter" (Geankoplis 1983),

M_B is the molecular weight of the solvent B (kg/kg mol), and

μ_B is the viscosity of the solvent B in (kg/m·sec).

Arrhenius relationship: $$k = k_0 e^{-E_a/RT} \tag{2.53}$$

where k is a general n^{th}-order heterogeneous rate constant ($(mol/cm^3)^{1-n} \cdot sec^{-1}$),

k_0 is the pre-exponential factor (cm/sec),

E_a is the apparent activation energy (J/mol),

R is the gas constant (8.314 J/mol·K), and

T is the absolute temperature (°K).

For reactions in aqueous solutions, therefore, a doubling of the *absolute* temperature nearly doubles the diffusivity, but the chemical reaction

rate constant can be increased by two orders of magnitude or more depending on the activation energy of the system. For this reason, the activation energy of diffusion controlled processes is characterized as being 10 kJ/mol to 20 kJ/mol while chemical reaction controlled processes usually exhibit activation energies greater than 40 kJ/mol.

This generality, however, is limited to reactions in aqueous solution and some gas-phase systems, and may not apply to catalytic reactions or other systems where strong interparticle pore diffusion or external mass transfer resistances dominate (Smith 1970, Levenspiel 1972, Szekely et al. 1976, Sohn and Wadsworth 1979, Froment and Bischoff 1990, Fogler 1992). In these situations, falsification of the kinetic rate coefficients and the activation energy can occur due to diffusion effects. The magnitude of the effect of this falsification can be illustrated by applying an Arrhenius-type temperature dependency to the diffusion coefficient as well as to the chemical reaction rate constant; a valid procedure as long as the temperature range is not too large (Levenspiel 1972).

$$D_{AB} = D_0 e^{-E_{diff}/RT} \tag{2.54}$$

where D_0 is the equivalent pre-exponential factor for diffusion (cm^2/sec), and

E_{diff} is the activation energy for effective diffusion (kJ/mol).

In their discussion of falsified or disguised kinetics, the previous authors describe that for any n^{th}-order heterogeneous reaction with significant interparticle pore diffusion or external mass transfer resistance, the observed rate of reaction is proportional to $(kD_{AB})^{1/2}$ from the following equation (Froment and Bischoff 1990):

$$(r_A)_{obs} = \frac{S}{V}\sqrt{\frac{2}{n+1}D_{AB}k}\left(C_A\right)^{(n+1)/2} \tag{2.55}$$

where $(r_A)_{obs}$ is the observed rate of reaction (mol/g catalyst/sec),

S is the external surface area of the catalyst (m^2),

V is the catalyst volume (m^3),

n is the reaction order,

D_{AB} is the effective diffusivity (cm^3/cm catalyst/sec),

k is the heterogeneous rate constant (cm^3/g catalyst/sec),

C_A is the molar concentration of the fluid reactant at the solid surface (mol/cm^3).

Equation 2.55 illustrates the dependency of the observed rate of reaction on $(kD_{AB})^{1/2}$. Employing Arrhenius relationships for both the chemical rate constant and the effective diffusion (Eq. 2.53 and 2.54) indicates that the apparent activation energy is the arithmetic average of the activation energies of the intrinsic reaction and diffusion.

$$k_{obs} = \frac{S}{V}\sqrt{\frac{2}{n+1}}\left[D_0 e^{-E_{diff}/RT} k_0 e^{-E_a/RT}\right]^{1/2} \tag{2.56}$$

so that

$$E_{obs} = \frac{d\ln(k_{obs})}{d(1/T)} = \frac{E_{diff} + E_a}{2} \approx \frac{E_a}{2} \tag{2.57}$$

Since the activation energy for gas-phase reactions under chemical reaction control is rather high (80 kJ/mol to 250 kJ/mol) and the activation energy for diffusion is small (5 kJ/mol at room temperature to ~15 kJ/mol at 1000°C (Levenspiel 1972)), Eq. 2.57 is generally true. Therefore, for situations with strong interparticle diffusional or external mass transfer resistance, the observed activation energy may be only one-half the true activation energy. According to Froment and Bischoff (1990), this provides one possible experimental test for the presence of diffusion problems. If the observed activation energy is 20 kJ/mol to 40 kJ/mol, it is probably one-half of the true chemical activation energy value; however, if the observed activation energy is 85 kJ/mol, it could be the true value or one-half of 190 kJ/mol. In this latter instance, the experimental test would be inconclusive.

2.5 Voltammetry

The general electrochemical category of voltammetry includes a sophisticated collection of analytical techniques where the relationship

between voltage and current is observed at an electrode during an electrochemical process. The current measured at the electrode is a function of the potential applied to the electrode and when that potential is systematically varied, the resulting current-potential plot is a voltammogram.

Voltammetry can be used to analyze any electroactive chemical species that can be made to oxidize or reduce. By controlling the electrode potential, the experimenter can control the redox reaction occurring at the electrode surface. Current measured at the electrode surface is a measure of redox electron transfer, or electron flow. This current is proportional to the concentration of electroactive species in the electrochemical system being studied.

Cyclic voltammetry (Harris 1991, Hibbert 1993, Gosser 1994) is used principally to characterize the redox properties of compounds and to study the mechanism of redox reactions. A cyclic potential sweep is imposed on an electrode and the current response is observed. Analysis of the current response can give information about the thermodynamics and kinetics of the electron transfer reaction at the electrode-solution interface, as well as provide information about the kinetics and mechanisms of homogeneous chemical reactions initiated by heterogeneous electron transfer at the electrode surface. A triangular waveform similar to the illustration in Figure 2.4a is applied to the working electrode and the current generated at the

electrode is measured (Figure 2.4b). By convention, an oxidizing potential is assigned a positive value and the associated anodic, or oxidizing current is assigned a negative value. Conversely, a reducing potential is assigned a negative value and its associated cathodic, or reducing current is positive.

For any cyclic voltammogram, the initial sweep potential is set at a value (the rest potential) where zero current occurs (t_0 in Fig. 2.4). This value is generally not at either the cathodic or anodic extreme, but rather at an somewhat arbitrary intermediate value. As the potential sweep begins, for example in the positive anodic direction, the current associated with the anodic redox process increases to a maximum and decreases as the potential is made even more positive. This happens as the electroactive species becomes depleted immediately around the electrode surface, and diffusion from the bulk solution is too slow to replenish the depleted concentration. As the anodic potential reaches its maximum value (t_1 in Fig. 2.4), the current has decayed to a relatively small value. After t_1, the potential is reversed and the sweep begins in the negative cathodic direction.

When the potential is sufficiently reducing, the oxidized species around the electrode begins to reduce and the cathodic wave begins to appear. The cathodic current also passes through a maximum as applied potential decreases and ultimately decays as the potential approaches the maximum cathodic value (t_2). The potential is again reversed, and anodic

potential is applied to achieve the final rest potential (t_0), and the completion of one potential sweep cycle.

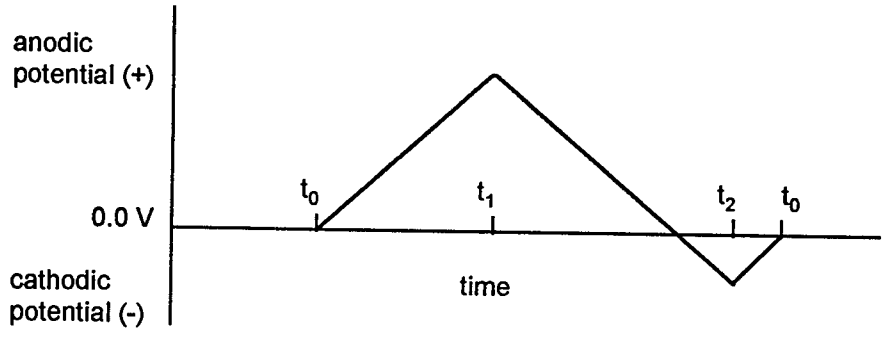

(a)

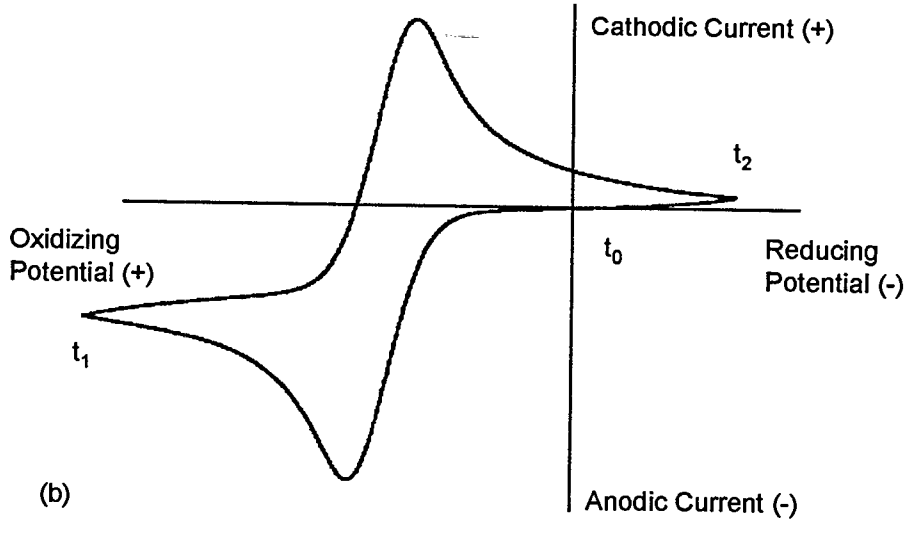

(b)

Figure 2.4. (a) the potential waveform used in cyclic voltammetry, and (b) the resulting cyclic voltammogram.

The voltammogram in Figure 2.4b is an example of a reversible electrode reaction where the redox process is fast enough to maintain equilibrium concentrations of both reactant and product at the electrode surface as the electrode potential is varied. Studying the peak current as a function of the rate of change of applied potential is useful in evaluating the kinetic rate constants of electrochemical reactions. If there are secondary chemical reactions competing for the electrochemical reactants or products, the shape of the voltammogram will reflect the rates of these competing reactions.

2.6 Mixing and Segregation in Dry Particulate Systems

Wide differences among material properties such as particle size distribution, density, particle shape, porosity, and any surface characteristics, such as electrostatic charge or adsorbed moisture, make dry blending or dry segregation of particulate systems very difficult to achieve with consistent uniformity. In fact, powder handling technologists still do not completely understand the interaction of specific material properties well enough to predict the performance of a bulk assemblage without the benefit of laboratory testing or previous field experience. Technologists *do* recognize that materials in dry particulate systems interact; not only among the various size fractions of the same material, but also among other materials present in

the system. However, the *a priori* prediction about the interactive behavior of a specific system in mixing or segregating modes is generally not possible. In some systems, the interaction of the material is so profound that dry material segregation can not be accomplished.

In particular, the properties and behavior of fine powders (<70 μm) are especially interesting. Dry particulate mixing generally follows one of two theories based on the cohesive characteristics of the particle system. The *random mixing theory* (Williams 1968, Hershey 1975) assumes that free-flowing particles similar in size, density, and size distribution are randomly mixed according to a variety of mechanisms including diffusion and convection. The *ordered (or interactive) mixing theory* does not require equally sized or weighted particle distributions and utilizes the natural cohesive or interparticle interaction (adsorption, chemisorption, surface tension, frictional, electrostatic, or other forms of adhesion) to help explain homogeneity in the final particulate system (Hershey 1975, Yip and Hershey 1977a, 1977b, Egermann 1980, Lai et al. 1981).

The concept of ordered mixing is based on adhesion of fine particles to larger particles in the system. These cohesive properties and other surface phenomena tend to develop with increasing particle fineness and have been found to *order* rather than *randomize* the mixing process (Hershey 1975). This has been demonstrated in the pharmaceutical industry where the

importance of complete and uniform mixing of microdose quantities of specific drugs with inert carrier vehicles is important for dosage control and product quality assurance. These studies have been dominated by bi-particulate systems where the mono-size inert carrier particles are of the order of several hundred microns in diameter and the smaller drug particles are <5 to 100 microns in diameter. Ordered mixing is the result of uniform adhesion of the smaller particles to the larger particle, and was found to be present in several cases (Yip and Hershey 1977b, Bryan et al. 1979, Rees and Staniforth 1979, Lai et al. 1981, Ibrahim et al. 1989, Fan and Chen 1990).

Segregation or separation of the smaller particles from the final mixture was found to be achieved, but only to a limited extent based on the pore size of the larger carrier vehicle (Rees and Staniforth 1979), the concentration of the micronized particle fraction (Bryan et al. 1979, Lai et al. 1981), the energy input and bed height of the segregation apparatus (Lai et al. 1981), and from the presence of a size distribution in the larger carrier vehicle (Yip and Hershey 1977a).

The problem of efficient segregation of fine particulate systems has also been studied in gas-fluidized bed applications. As with bulk dry-powder mixing, interparticle forces was found to promote aggregation of fine particles (<70 μm), prevent their uniform dispersion, and result in channeling and

excessive entertainment in the off gas stream. The forces attributed to the cohesion of fine particles included van der Waals forces (Rumpf 1962, Baerns 1966, Chaouki et al. 1985, Bowling 1988, Visser 1989, Lam and Newton 1992, Baeyens 1992); electrostatic attraction (Rumpf 1962, Derjaguin et al. 1968, Bailey 1984, Briens et al. 1992); fluid bridges (Parker and Stevens 1959, Rumpf 1962); and a general crystallization or precipitation phenomena (Geldhart et al. 1984, Kono 1987).

In the work by Chaouki et al. (1985), mixed copper-alumina aerogels initially a few nanometers in size, agglomerated to form secondary and tertiary particles ultimately achieving particles on the order of a micron in diameter. The bulk material was found to be extremely amorphous with a specific surface area of ~400 m^2/g and a bulk density of only 66 kg/m^3. After fluidization above a minimal superficial gas velocity, the particles again agglomerated to form clusters on the order of 1000 μm in size. They postulated a model based on van der Waals forces as responsible for the agglomeration phenomena. In a later work, Li et al. (1990) also found that in high velocity gas-fluidized beds SiO_2 and Fe_2O_3-SiO_2 aerogels originally <20 μm in size agglomerated into stable clusters nominally 200 μm to 300 μm in diameter.

Since material properties, particle size distribution, and the particle environment define the mechanism of agglomeration, fine particle cluster

stability can vary widely. In investigating the role of electrostatic forces on the adhesion of polymer particles to solid surfaces, Derjaguin (1968) determined that it required an acceleration of 10^5-10^6 g to remove small particles (<30 μm) in a direction normal to the substrate surface. Others (Mantz 1988, Ranade et al. 1988, Thoma 1991, Jaraiz 1992) also attempted to quantify interparticle forces and agglomerate strength distributions to understand the fundamental nature of their formation and to develop methods for their dispersion. In many cases, partial to total dispersion of fine particulate systems can be achieved by vibration, the use of ultrasonic or high-decibel acoustic fields, and by the use of liquid media, or by combinations. It was generally concluded by Bowling (1988), however, that by immersing adherent particles in a liquid, the van der Waals force could be reduced by about a factor of two because the liquid shielded the attractive force. It was also determined that electrostatic effects also become negligible because of the larger magnitude of the static dielectric constant of the liquid medium compared to that of a gas or a vacuum.

Briens (1992) used surfactants in an ultrasonic bath to de-agglomerate materials prior to determining their particle size distribution by laser light diffraction. The work by Renade et al. (1988) and the review by Bowling (1988) conclude that for the microelectronics and semiconductor industries, the use of liquid media (possibly in combination with surfactants and

ultrasound) allowed for better cleaning of micron and sub-micron size particles from surfaces; and that non-contact cleaning was much less effective than the action of physical scrubbing.

Generally, in all of these investigations into fine dry powder interaction, some method of particle size determination was performed on the final mixture. In cases where fine particles (<70 μm) were a part of the final mixture, *never was dry sieving used* as the technique for determining the final size distribution. Nathier-Defour et al. 1993, Karuhn 1996, and Nushart 1996 agreed that below ~80 μm, the effectiveness of segregation by dry sieving became questionable. In work by Benoni et al. (1994), wet sieve analysis was performed on the fluidized bed material to determine if agglomerates were contributing to the entrainment flux. Wet sieving was the technique chosen because of its ability to disperse possible fine particle agglomerates in samples collected from the fluid bed off gas stream. Other researchers relied on dry particle image analysis to examine cluster formation, while still others used laser diffraction or sedigraph techniques for determining particle size distributions of fine particle assemblages.

3 EXPERIMENTAL PROCEDURE

3.1 Overview

As described in the Introduction, this research concentrated on studying the dissolution behavior of plutonium oxide in the HCl-Fe(II) system. The PuO_2 used in this study was prepared by oxalate precipitation of nitrate ion exchange eluate. The precipitate was decomposed to PuO_2 by calcination at a temperature of between 400°C and 450°C for 48 hr. The resulting surface area determined by a NOVA-1000 BET gas sorption surface area analyzer (Quantachrome Corporation, Syosset, NY) was ~28 m^2/g. Additional chemical analysis of the product oxide was performed and is presented in Table 3.1. The HCl concentration for these experiments was chosen at 7.0 *M*, and the iron concentration was set at a value of 40 *mM*. All experiments were conducted in an electrochemical 'H'-cell (Figures 3.1 and 3.2) with the two compartments separated by a medium porosity glass frit. Each compartment contained 75 ml of solvent with the agitated dissolution compartment containing the iron and the PuO_2. The initial solid plutonium oxide concentration was ~0.05 *M* (1.000 g PuO_2 in the 75 ml agitated compartment). Except for Arrhenius experiments, the temperature of the system was fixed at 50°C, and agitation was accomplished by a magnetic stirrer rotated at 500 rpm.

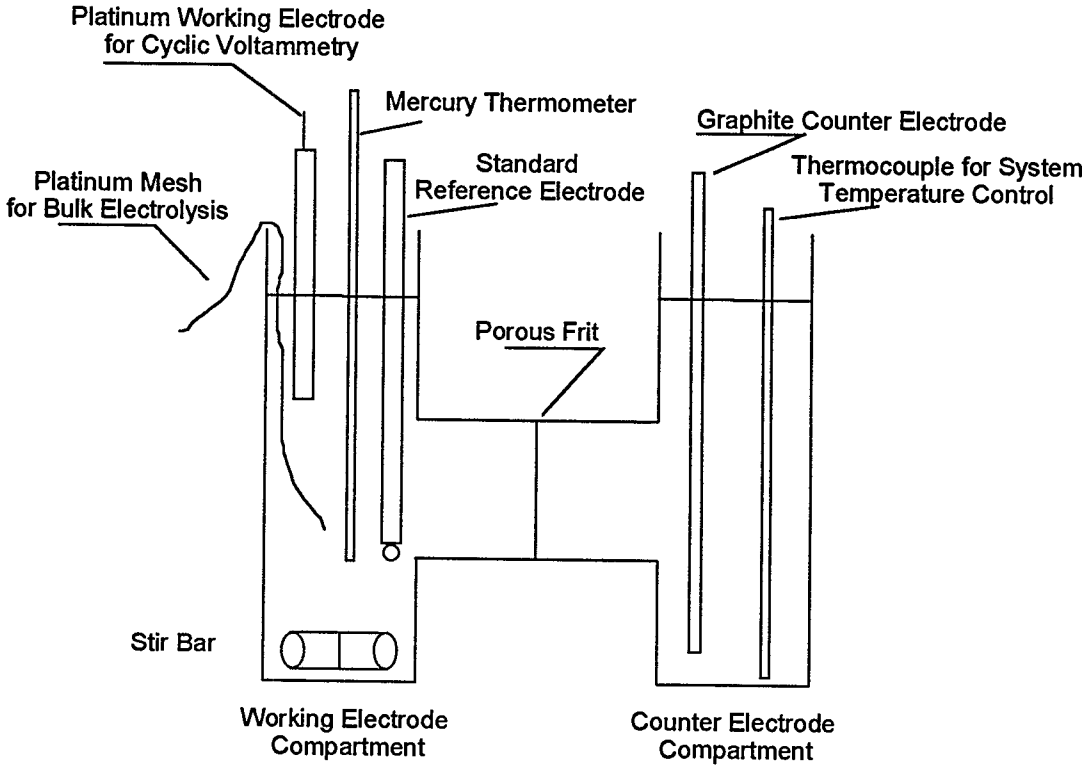

Figure 3.1. Schematic of the electrochemical cell used for studying PuO_2 dissolution in the HCl-Fe(II) system.

In contrast with other researchers investigating the reductive dissolution of PuO_2, bulk electrolysis was used to continually regenerate the Fe(II) electron transfer catalyst from the PuO_2 reduction byproduct Fe(III) to maintain the Fe(II) concentration constant for participation in the overall reaction

$$PuO_2 + 4H^+ + Fe^{+2}_{(aq)} \rightarrow Pu^{+3}_{(aq)} + 2H_2O + Fe^{+3}_{(aq)} \tag{1.1}$$

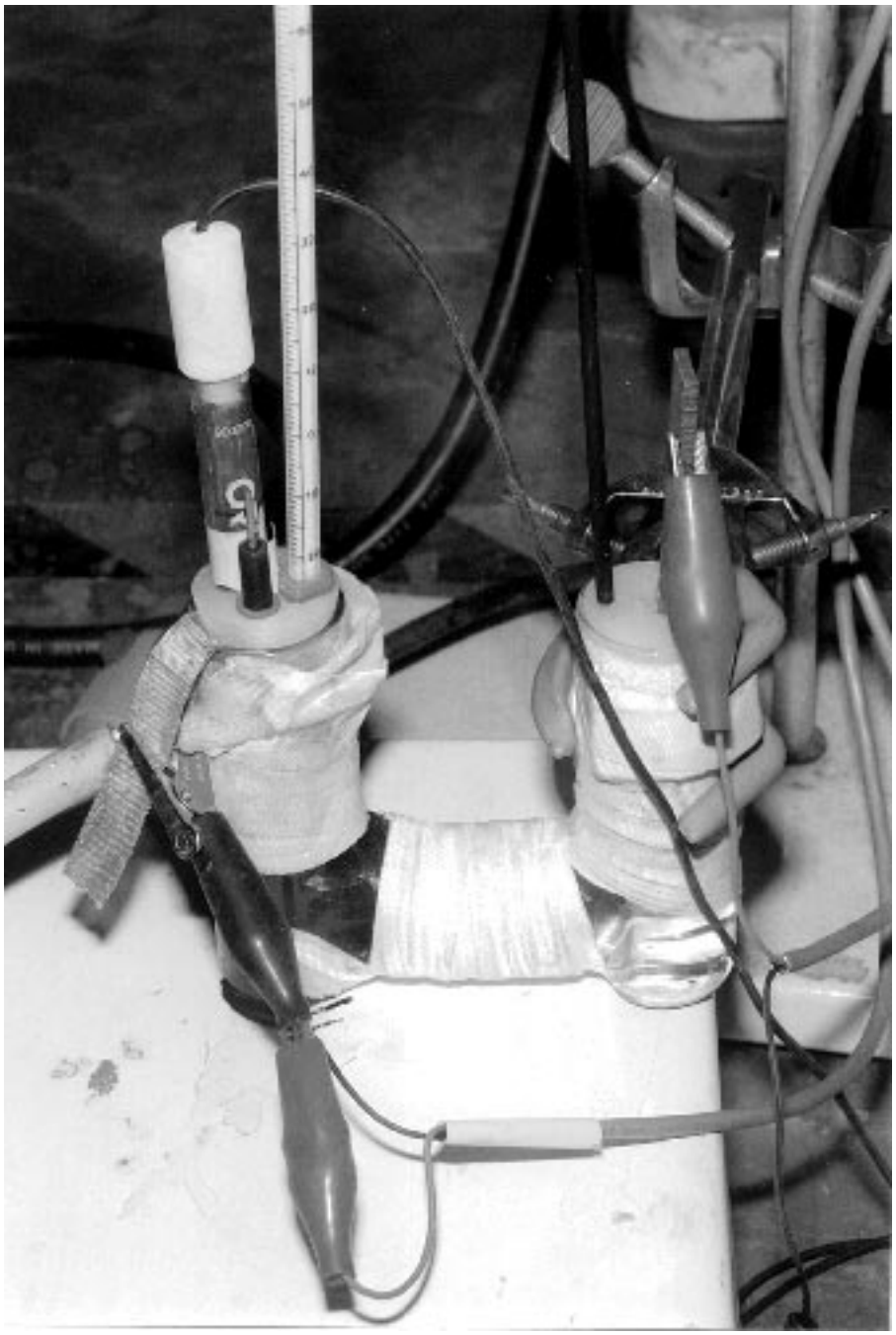

Fig.ure 3.2: The electrochemical cell used for studying PuO_2 dissoltion in the HCl-Fe(II) system.

Table 3.1. Analytical Composition of the PuO_2 used in this Study

Element	Concentration
Aluminum	25 ppm
Americium	927 ppm
Barium	<2 ppm
Beryllium	<1 ppm
Boron	<5 ppm
Bismuth	<1 ppm
Cadmium	<10 ppm
Calcium	500 - 5000 ppm
Carbon	1200 ppm
Chromium	40 ppm
Copper	10 ppm
Iron	140 ppm
Lead	100 ppm
Lithium	<1 ppm
Magnesium	40 ppm
Manganese	4 ppm
Molybdenum	<20 ppm
Nickel	20 ppm
Potassium	1 -10 wt. %
Plutonium	86.21 wt. %
Rubidium	<10 ppm
Silicon	270 ppm
Silver	10 ppm
Sodium	100 ppm
Strontium	50 ppm
Tin	<5 ppm
Uranium	520 ppm
Zinc	<5 ppm

This approach kept the inventory of Fe(II) in the system at a constant, yet relatively small value (40 *mM*) instead of requiring a considerable stoichiometric excess to drive the plutonium oxide reduction reaction to completion. Also, by maintaining the iron completely in a reduced state

eliminated one variable in the kinetic analysis since the effect of changing Fe(II) concentration on the dissolution rate can be ignored.

Cyclic voltammetry was used as an *in-situ* analytical technique to monitor the extent of the dissolution reaction with time. In linear potential sweep methods, of which cyclic voltammetry is a part, the peak current is linearly proportional to the concentration of the electroactive species in solution (Bard and Faulkner 1980).

$$i_p = (2.69 \cdot 10^5) n^{3/2} A D_o^{1/2} v^{1/2} C_o \tag{3.1}$$

where; i_p = peak current (A),

n = number of electrons involved in the reaction,

A = the surface area of the electrode (cm^2),

D_o = the diffusivity constant (cm^2/sec),

v = the potential scan rate (V/sec),

C_o = concentration (mol/cm^3).

A dissolution experiment was conducted by equilibrating the acid solvent to the desired temperature, adding the iron (as ferrous chloride tetrahydrate), conducting a background voltammogram of the HCl-Fe(II) solvent to obtain the background iron wave, adding the desired amount of PuO_2, and obtaining voltammograms of the resulting solution at periodic time

intervals. The voltammograms were repeated over the background iron wave to measure the growth of the plutonium concentration in solution as evidenced by the increasing peak current of the Pu(III)-Pu(IV) anodic and cathodic waves. A representative series of voltammograms illustrating this technique is shown in Figure 3.3. By continuing the dissolution experiment until all (>95%) of the PuO_2 was dissolved, the peak height of the final scan could be used to ratio against the other peak heights at intermediate times to determine the extent of the dissolution reaction at these times. Ninety five percent total dissolution was chosen arbitrarily to represent the end of an experiment and was determined by one of three techniques: (1) if two sequential, repetitive scans overlapped and therefore showed no concentration increase with time, (2) if >95% of the theoretical coulombs were passed to the dissolution cell (~356 C are theoretically required to dissolve 1.00 g of PuO_2), or (3) the instantaneous cell current was consistently <10 mA.

Based on Eq. 3.1, a ratio of the peak heights essentially are C/C_{max} data, or X (extent of reaction data) vs. time and can be evaluated by traditional kinetic approaches as illustrated in Figure 3.4. This experimental procedure was applied to PuO_2 that had been sieved to fairly narrow particle size fractions representing the makeup of the particle size distribution of the entire oxide assemblage. The entire oxide assemblage was similarly

evaluated to determine the extent of interference or influence particle size might have on the oxide dissolution rate.

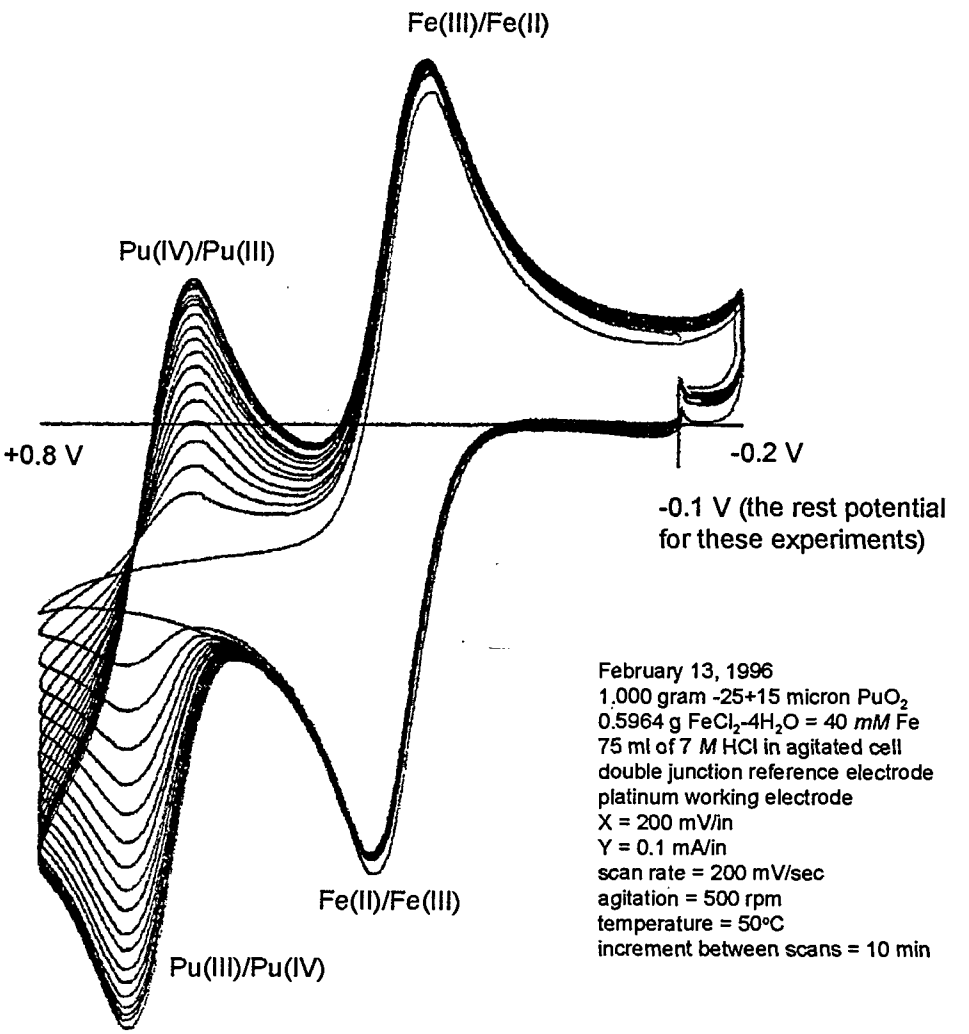

Figure 3.3. A series of cyclic voltammograms from the dissolution of plutonium dioxide in HCl-Fe(II) showing the increase in dissolved plutonium as dissolution proceeds.

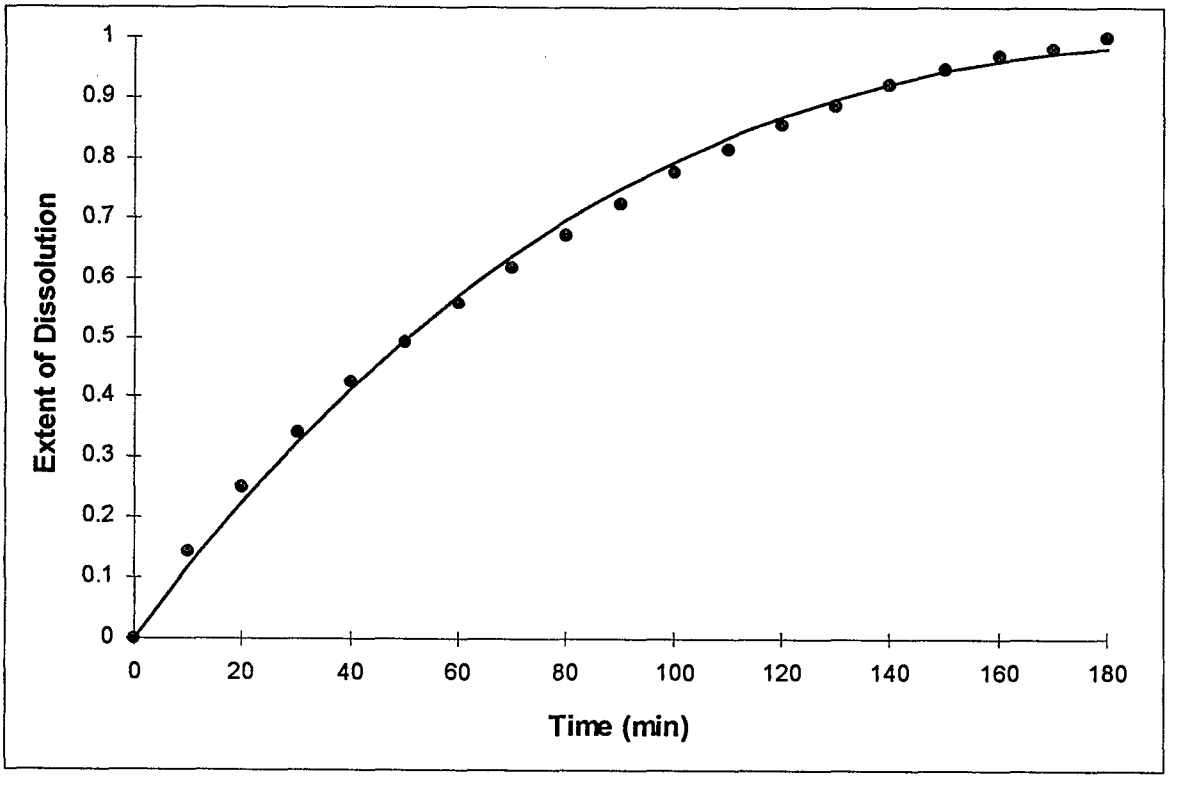

Figure 3.4. Dissolution rate data from cyclic voltammogram peak-height ratios.

3.2 Equipment

3.2.1 Electrochemical and Associated Equipment

The electrochemical cell used in these experiments was previously described in Figures 3.1 and 3.2, and was constructed from ~30 mm I. D. Pyrex® glass tubing (Corning, Inc., Science Products Division, Corning, NY, product number 235350). The cell had an overall height of ~12.5 cm and a

width of ~12.5 cm. The medium porosity fritted glass disk separating the two compartments had a maximum pore opening of 10 μm to 15 μm, sufficient to promote good electron mobility and support the necessary cell reactions.

In the agitated working electrode compartment, the following reactions occurred:

oxide dissolution (the overall cell reaction)

$$PuO_2 + 4H^+ + Fe^{+2}_{(aq)} \rightarrow Pu^{+3}_{(aq)} + 2H_2O + Fe^{+3}_{(aq)} \tag{1.1}$$

and bulk electrolysis (reduction) at the cathodic working electrode

$$Fe^{+3}_{(aq)} + e^- \rightarrow Fe^{+2}_{(aq)} \tag{3.2}$$

At the graphite counter electrode (anode), the following oxidation reaction occurred

$$2Cl^-_{(aq)} \rightarrow Cl_{2(g)} + 2e^- \tag{3.3}$$

The electrons generated by the oxidation of chloride to chlorine at the cathode were conducted to the agitated working electrode compartment to complete the electrochemical cell and to be used to maintain iron in the reduced state.

Bulk electrolysis occurred at a platinum mesh electrode ~12 mm wide having an immersed length of ~5 cm (procured from the Los Alamos National Laboratory precious metals stock). The precision area stationary electrode for cyclic voltammetry was also constructed from platinum (Bio Analytical

Systems, West Lafayette, IN, part number MF2071). The reference electrode used in these experiments was a double junction electrode supplied by Orion Research (Boston, MA, part number 900200) with saturated AgCl as the inner solution and 10% KNO_3 as the outer solution. The counter electrode was graphite (Electrosynthesis, Inc., Rochester, NY). The electrochemical cell was wrapped with ~12 mm wide heat tape (from Glas-Col Apparatus, Terre Haute, IN) which was maintained at a specified temperature using a J-Kem Scientific (Ellisville, MO) model 210 temperature controller with a 0.1°C set point capability. Temperature was monitored in the working electrode compartment using a calibrated mercury thermometer with a range of -20°C to 110°C (Van Waters and Rogers (VWR), Scientific, San Francisco, CA, part number 61016-068). Agitation was provided by a series 400 combination hot plate and stirrer (VWR Scientific) where the speed could be set digitally and the agitation time measured. The magnetic stirrer was a 25 mm. Starburst™ magnetic stirbar (VWR Scientific, part number 58947-824)

The electrochemical equipment for this system consisted of an EG&G Princeton Applied Research Corporation (Princeton, NJ) model 273 potentiostat/galvanostat, an EG&G Princeton Applied Research Corporation model 175 universal programmer, and a Bausch & Lomb (Houston Instruments Division, Inglewood, CA) Omnigraphic 2000 X-Y recorder. The potentiostat controlled the current range of the electrochemical cell during

both bulk electrolysis and cyclic voltammetry, displayed the instantaneous current (mA) drawn by the cell, and measured the total integrated charge passed to the cell (coulombs) during bulk electrolysis. The universal programmer controlled the potential sweep parameters (initial, maximum, minimum, and final potential values) for cyclic voltammetry; including the potential range and the scan rate. The recorder scaled the resulting current–potential data from the voltammogram and plotted the data in a form similar to Figure 3.2 shown previously. All thermocouple, power, and electrochemical signals were routed to and from the glovebox enclosure to prevent radioactive contamination of the major electrochemical and temperature control apparatus.

3.2.2 Particle Size and Sieving Equipment

Particle size distributions can be measured using any of several techniques; sieving, sedigraph, optical diffraction, optical transit times, or a combination of methods. Because of inherent differences in particle size measurement techniques, it is difficult to compare the results from two different instruments directly. Oxide particle size distribution for this study was obtained by two methods; a transit time measuring technique based on scanning laser microscopy provided by LASENTEC (Redmond, WA) in the form of their LAB-TEC™ 1000 instrument, and by sieving using a model L3P

ATM Sonic Sifter with a horizontal pulse attachment model L3N8 (from ATM Corporation, Milwaukee, WI). Since actual experimentation was necessary on gram quantities of PuO_2, the sieving not only provided an alternate method of determining particle size distribution, but also provided the dry particle sieve splits for subsequent kinetic evaluation.

The LAB-TEC™ 1000 fits into the category of transit time measurement techniques (LASENTEC 1992). In this technique, representative samples are obtained by a vibratory splitting procedure (riffling) and are dispersed in a dilute (1–3 wt.%) aqueous sodium pyrosulfate solution (a surfactant to eliminate agglomeration). The solvent is agitated slightly allowing no solution vortex to form prior to particle counting by scanning laser microscopy. When counting, the focal point is scanned across the particles producing pulses of back-scattered light which represent the length of time the focal spot illuminates the particle. The focal spot of the instrument does not scan across only the center of a particle (producing a direct measure of particle diameters); rather it scans and produces a distribution of chords which represent the lengths of particle segments in the distribution. This random chord distribution can be corrected statistically to produce a spherical equivalent mean distribution if the particles are generally spherical in shape. If the particles are irregular or definitely non-spherical, however, this correction can produce undesirable results.

The model L3P Sonic Sifter with a model L3N8 horizontal pulse attachment from ATM Corporation (see Figure 3.5) is a laboratory scale device that uses an oscillating air column augmented by mechanical tapping (accomplished by the horizontal pulse attachment) to achieve dry separation of fine and subsieve particle sizes (Suhm 1969, ATM 1995). Precision electroformed nickel sieves for the instrument are available in various sizes including sieves with openings of 5 μm. The instrument utilizes sonic energy to oscillate a confined air column at an operating frequency of up to 60 cycles per second. Elastomeric diaphragms are used to achieve a dust-tight enclosure and to promote oscillation of the air column. The mechanical pulsing, which can be applied both vertically and horizontally, was advertised by the manufacturer to be effective in deranging or breaking down the cohesive nature of many fine materials.

3.3 Procedure

Reagents were weighed using a Mettler AJ100 analytical balance (Mettler Toledo, Heightstown, NJ) with a precision of 0.1 mg. All weights were accurate to a value of ± 0.3 mg and all volumes were accurate to the nearest 0.5 ml using graduated cylinders. The source of iron was reagent grade $FeCl_2$-$4H_2O$ supplied by VWR Scientific. To achieve 40 *mM* Fe(II) in 75 ml of 7 *M* HCl, 0.5964 g of the hydrated salt was required.

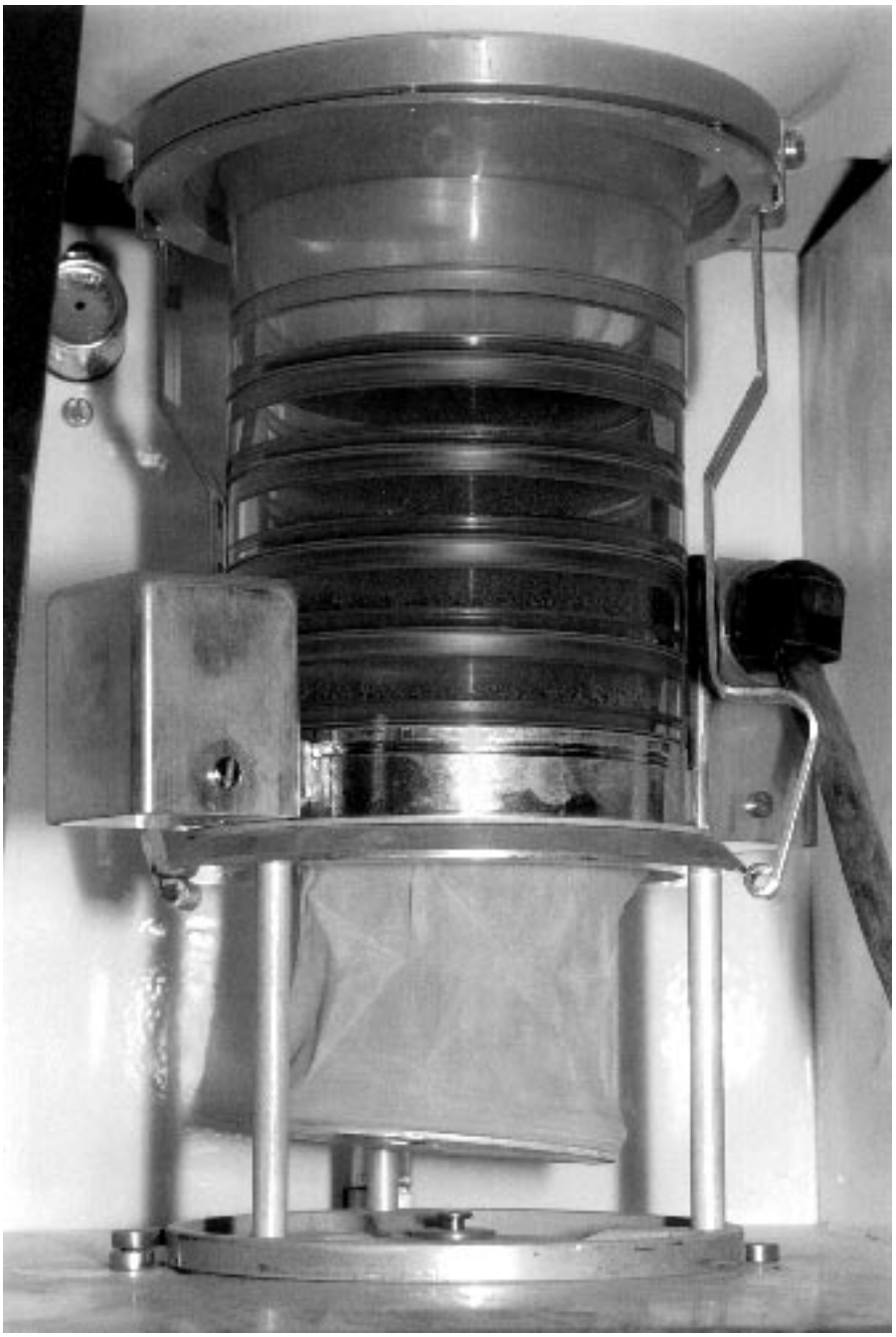

Fig.ure 3.5: The ATM Sonic Sieve apparatus used for obtaining screen fractions of the PuO_2 assemblage.

An experiment was started by initiating heat to the electrochemical cell containing the 7 *M* acid. During this heating period, the precision area platinum working electrode was gently polished using an alumina-water slurry and rouge cloth or a very fine-grit polishing paper to renew the metallic surface. The $FeCl_2$-$4H_2O$ and the PuO_2 reagents were also weighed during the heating period and moved to vicinity of the electrochemical cell. Cell temperature was controlled from the stagnant compartment containing the graphite anode. Although not the optimum method for temperature control, this was necessary since separate additions of reagents to the agitated compartment would have required removing the thermocouple for temperature control from solution for a few seconds. Previous experience illustrated that this caused the temperature controller to sense a temperature decrease and provide more power to the already equilibrated cell. This action produced a significant temperature spike, sometimes more than 5°C; which was totally unacceptable for this type of kinetic evaluation.

In an attempt to keep the temperature control in the agitated compartment, an alternative approach was investigated that consisted of momentarily turning off the controller during reagent addition. However, when turning the power back on, the controller immediately sent power to the heating element during the few seconds it took to reset itself and compare the setpoint to the actual temperature. This also produced unacceptable

temperature fluctuations. A workable alternative was found by controlling the cell temperature from the stagnant counter electrode compartment and monitoring the reaction temperature in the agitated compartment with a calibrated mercury thermometer. In this manner, the reaction temperature could be adjusted and controlled by manually trimming the controller as necessary. Use of this approach generally permitted an acceptable temperature control of $\pm 0.3°C$ throughout the experimental program.

When the cell reached the predetermined temperature (usually 50°C), the iron salt was added to the agitated compartment and bulk electrolysis was initiated to ensure the iron was reduced to Fe(II). This was accomplished by adjusting the cell potential in the potentiostat to -0.1 V, the cell current range to a maximum of 1 A, and supplying power to the electrochemical cell using the platinum mesh as the cathode and the graphite electrode as the anode. Bulk electrolysis of the Fe(II) salt would draw ~20 mA initially, and lower to <10 mA over a few minutes. At this point, the iron was reduced and preparation for the background cyclic voltammogram was complete.

In performing the background voltammogram, power to the cell was turned off, the current range setting on the potentiostat lowered to 1 mA, agitation to the cell turned off, the working electrode switched from the platinum mesh electrode to the precision area platinum working electrode, and power to the electrochemical cell reactivated. Upon activating the

universal programmer, the instrument would sweep the potential range at a scan rate of 200 mV/sec in the anodic direction to a maximum value of +0.8 V, reverse direction and sweep cathodically to a maximum value of -0.2 V and return to the rest potential of -0.1 V (refer to Figure 2.4). The X-Y plotter was scaled at an X-value of 200 mV/in and a Y-value of 100 μA/in. For the concentration range of reagents in the electrochemical cell, these instrument settings provided the appropriate window for recording cyclic voltammograms similar to those presented in Fig. 3.3.

After the baseline iron voltammogram was obtained, power to the electrochemical cell was again turned off, the current range returned to a maximum of 1 A, the cell agitation returned to its preselected value (500 rpm for these experiments), the working electrode changed from the precision area electrode to the platinum mesh for bulk electrolysis, and the plutonium oxide was added to the cell. After addition of the plutonium oxide, power to the electrochemical cell was enabled and the coulomb integrator on the potentiostat reset to zero. Voltammograms were then obtained at selected time intervals (normally 10 min) until the following criteria were met indicating completion of the experiment: the integrated coulombs were >95% of the theoretical amount required to dissolve 1 g PuO_2 (~356 coulombs), the instantaneous current drawn by the cell during bulk electrolysis was $\leq$10 mA,

and/or at least two successive voltammograms overlapped at their maximum peak heights indicating no concentration change with time.

As seen earlier in Figure 3.3, successive voltammograms were gathered as plutonium oxide dissolved in the system. Since peak heights are additive in this technique, the baseline voltammogram containing only iron was important for subsequently measuring the plutonium peak heights. Overall dissolution rate data were obtained from these voltammograms by measuring the peak height of the individual Pu(III)-Pu(IV) oxidation waves from the iron baseline decay point and obtaining the ratio of these heights to the maximum peak height at the completion of the experiment. Anodic, as opposed to cathodic, peak heights were used in this analysis because the bulk solution was in the reduced state due to the Fe(III)-Fe(II) cathodic reaction at the platinum mesh electrode. With the bulk solution reduced, more detail was available from the oxidation waves rather than from the cathodic reduction waves. As described earlier, concentration of electroactive species is linearly proportional to the peak current and these peak height ratios essentially translate directly to C/C_{max}, or X (extent of dissolution) data and can be evaluated by traditional methods.

When using cyclic voltammetry as an *in-situ* analytical technique, the iron wave was as an internal calibration or quality control reference point for each of the voltammograms where the growth of the anodic Pu(III)-Pu(IV)

wave was important. Ignoring a small amount of iron migration through the porous frit separating the two compartments, the iron concentration was essentially constant in the agitated side of the cell. Therefore, any significant changes in the shape of the curve or the position of the maximum anodic peak current pointed to potential problems with the precision area working electrode. If problems became evident with the electrode, they generally consisted of either an oxide layer beginning to form on the platinum surface that progressively altered the potential-current response during a voltammogram; or the degradation or separation of the epoxy mount surrounding the platinum wire constituting the electrode. Either of these problems ultimately led to changes in the precision surface area of the electrode and ultimately affected the potential-current response during voltammetry.

In many cases, changes in the working electrode were too subtle to affect the iron anodic wave and were only discovered after the dissolution data were plotted. In some experiments, the effects on the overall data quality were minimal while in other cases, problems with the working electrode or with fluctuations in the agitated cell temperature were significant enough to consider invalidating an entire experiment.

In the case of poor temperature control, temperature spikes in the agitated cell would occur as a result of thermal gradients being set up in the

stagnant compartment that provided inconsistent and inaccurate information to the thermocouple controlling the heat input to the cell. This resulted in spikes in the system temperature. The problem was further aggravated by acid fumes degrading the silicone rubber stopper holding the thermocouple in place. After a certain level of degradation, slight movement or jostling of the thermocouple during an experiment could agitate the solution in this compartment, set up thermal gradients, and generally result in a significant temperature spike measured by the mercury thermometer in the agitated compartment. These spikes had a magnitude of 3-5°C and could take up to 30 minutes to trim the temperature controller and return the system to normal. During the temperature upset, not only was the dissolution rate accelerated and the plutonium solution concentration elevated, but the resulting voltammogram peak heights were also shifted and influenced by the change in temperature. The overall result could be that portions of the resulting dissolution curve were biased high, affecting the slope of the linearized rate equation by biasing it high. Ultimately, this could cause precision and repeatability error in replicate experiments and affect the data quality of the entire experimental set. This problem was controlled (or minimized) by minimizing undue agitation of the stagnant compartment and frequent replacement of the rubber stoppers used to position and stabilize the control thermocouple in solution.

Another problem found to affect data quality was less obvious and dealt with degradation or fouling of the precision area working electrode. This was a subtle problem that normally did not manifest itself until comparison of replicated experiments was made. Successful cyclic voltammograms depended on having and maintaining a clean reproducible surface of the precision area working electrode. If this area changed or became fouled, the resulting scans were affected; generally causing a compression of successive waves and a shifting or separation of the position of anodic and cathodic peak values as the experiment progressed. Sometimes the effect was so severe that it appeared that the concentration of the electroactive species in solution was decreasing rather than increasing with time. This was clearly an unacceptable situation leading to a biased analysis of the rate data and other questions surrounding the quality of other experiments.

One apparent solution to the problem was to remove the electrode from solution and gently polish the platinum surface using an alumina-water slurry and rouge cloth or a very fine grit polishing paper. This was normally done at the beginning of an experiment to prepare the electrode. Unfortunately, this procedure subsequently proved to be unacceptable in the middle of an experiment because removing the electrode for cleaning caused a loss of temperature equilibration and the fresh platinum surface immediately after polishing was so reactive as to produce abnormal scans.

The following figures illustrate the extent of these types of working electrode problems.

Figure 3.6 is an example of the subtle nature of the shift in anodic peak location as an experiment proceeds. In this particular case, the data are acceptable, but the shift in the peak anodic current is illustrative of the progressive fouling of an electrode. As the experiment progressed, the peak anodic current peak moved slightly in the cathodic direction and then back anodically again. These data were retained because the individual plutonium waves were distinctive and contained sharp peaks. Also note that the reproducibility and position of the of the iron waves were also very good.

Figure 3.7 is an example of the severe shifting of the anodic and cathodic peak positions relative to each other. The peak heights of the background iron voltammogram are separated by over 200 mv while the foreground peak heights are separated by only about 75 mv. This problem was clearly identifiable after the initial voltammograms were taken, and was subsequently solved by replacing the precision area working electrode.

Figure 3.8 is another example of how subtle electrode fouling affects the active electrode surface area and ultimately, the quality of the final voltammograms. The compression of these voltammograms does not indicate the completion of an experiment, but rather illustrates how an oxide or compound coating building on the surface of the electrode during the

potential sweep, or just from being present in the solution, can affect data quality.

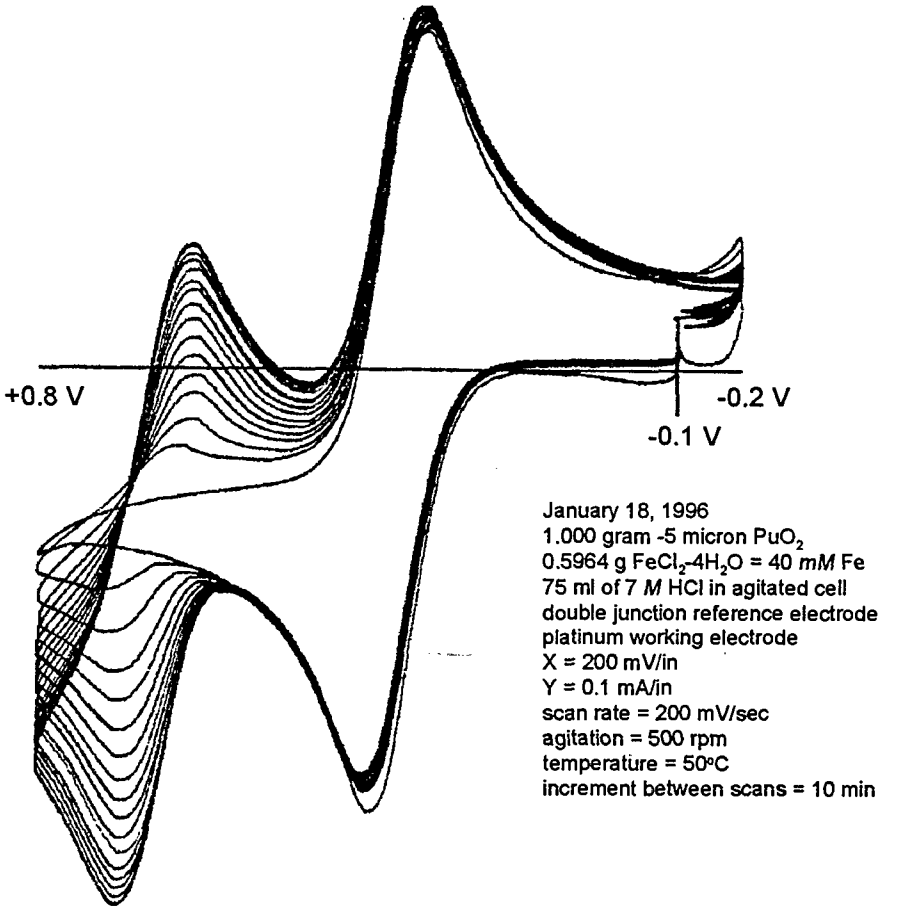

Figure 3.6. Subtle shifting in the position of the anodic peak current for plutonium indicating potential problems with the precision area working electrode.

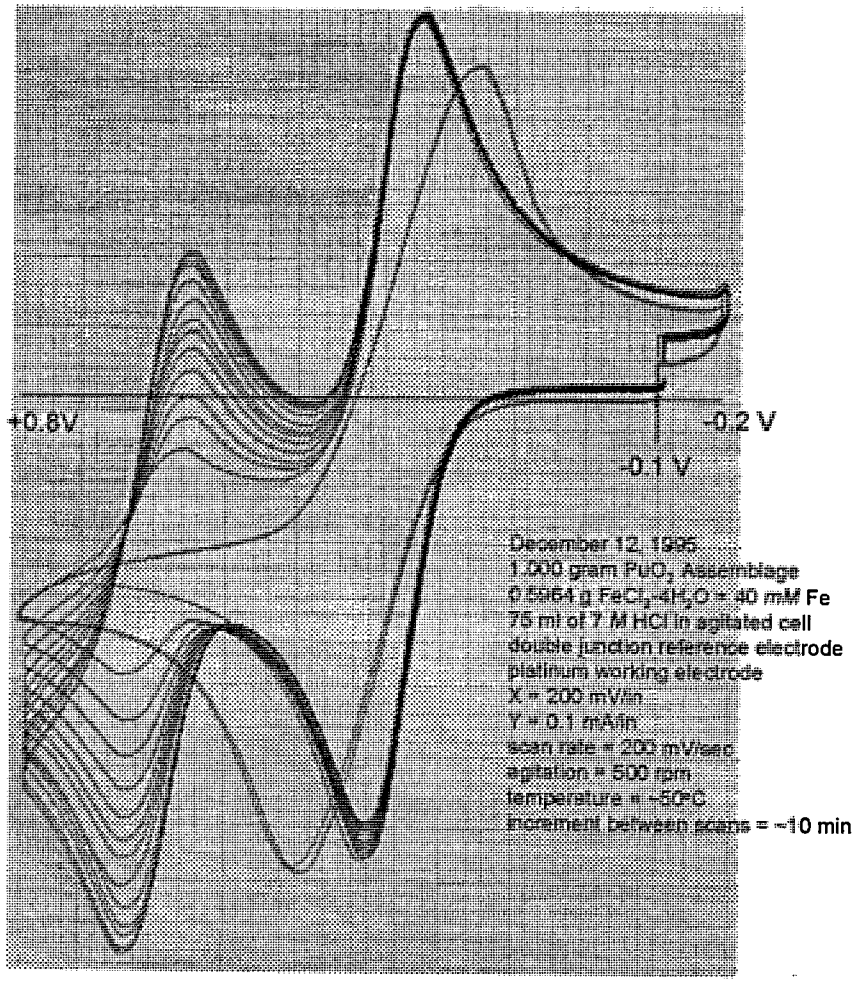

Figure 3.7. Evident problems with the precision area working electrode.

In Figure 3.8, the working electrode was removed from the cell and the surface polished after t_{13}. The next scan at t_{14} shows such a significant improvement in performance that not only this data point, but all of the previous scans are suspect. The magnitude of the problem was further illustrated by observing the successive scans at t_{15}-t_{17}, that show a decrease in anodic peak height as well as a systematic shift (anodically) in peak

position. As a result of the performance of this working electrode, this experiment was rejected from further analysis.

This problem of progressive fouling of the surface of the working electrode was ultimately solved by subjecting the electrode to a reducing potential near the knee of the reduction wave for solvent degradation.

$$2H^{+} + 2e^{-} \rightarrow H_2 \tag{3.4}$$

In this system, the value was determined experimentally to be ~-0.32 V (cathodic). By subjecting the working electrode to potential sweeps into this voltage region, the surface was regenerated *in situ* while maintaining electrode temperature equilibrium and not having to subject the electrode surface to excessive abrasive polishing. Note that it would also be possible to clean the electrode surface in the anodic region of solvent degradation (chloride–chlorine), but this region was not as attractive since dissolved chlorine in the working electrode compartment would tend to oxidize Fe(II) to Fe(III), with potentially undesireable effects on the oxide dissolution reaction. The reductive cleaning procedure was initiated when wave compression and peak shift was suspected. In Figure 3.8, this procedure would have been initiated possibly after t_7 and certainly after the appearance of the scan at t_{11}.

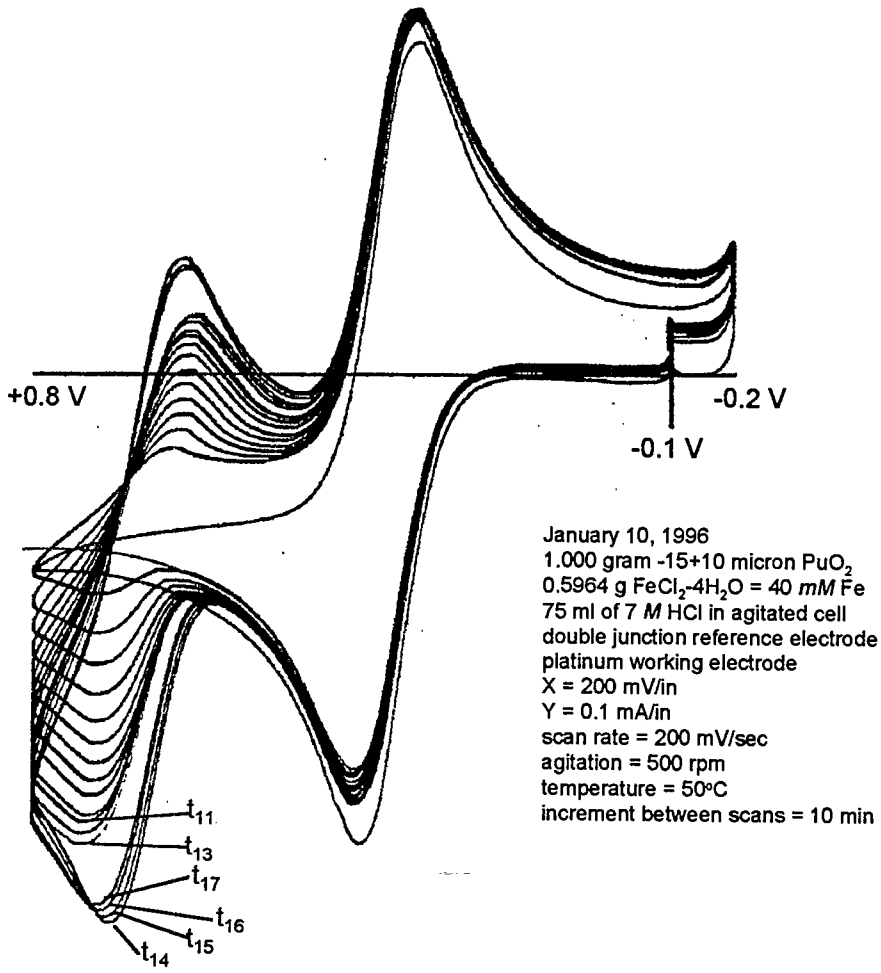

Figure 3.8. The more subtle, progressive fouling of a precision area working electrode.

4 RESULTS AND DISCUSSION

4.1 Overview

In light of the very different conclusions presented by the various researchers studying the dissolution of PuO_2 in nitric-hydrofluoric acid and other systems, this study approached the problem in a slightly different fashion. Narrow size fractions of the oxide assemblage were obtained in order to study their behavior under controlled conditions. One goal was to determine the heterogeneous model best describing the dissolution behavior of this sample of plutonium oxide and later to determine the effects, if any, of particle size on the appropriate model. This source of PuO_2 had a fairly narrow size distribution as determined by the LASENTEC scanning laser microscopy system discussed in Section 3.2.2. Approximately 95% of the material had a particle diameter <70 μm as shown in Figure 4.1.

Intuitively, one would expect the smaller size material to dissolve faster and to possibly be governed by a mixed model or a film diffusion controlled model since the individual small particles may be nearly buoyant in the solvent. In addition, one might expect that as surface reaction controlled dissolution proceeds, the particle size distribution would change, such that at some point, a distribution would be produced with a large fraction of very fine particles that would cause the heterogeneous model to shift between a

predominately surface controlled reaction to one governed by some mode of film diffusion control.

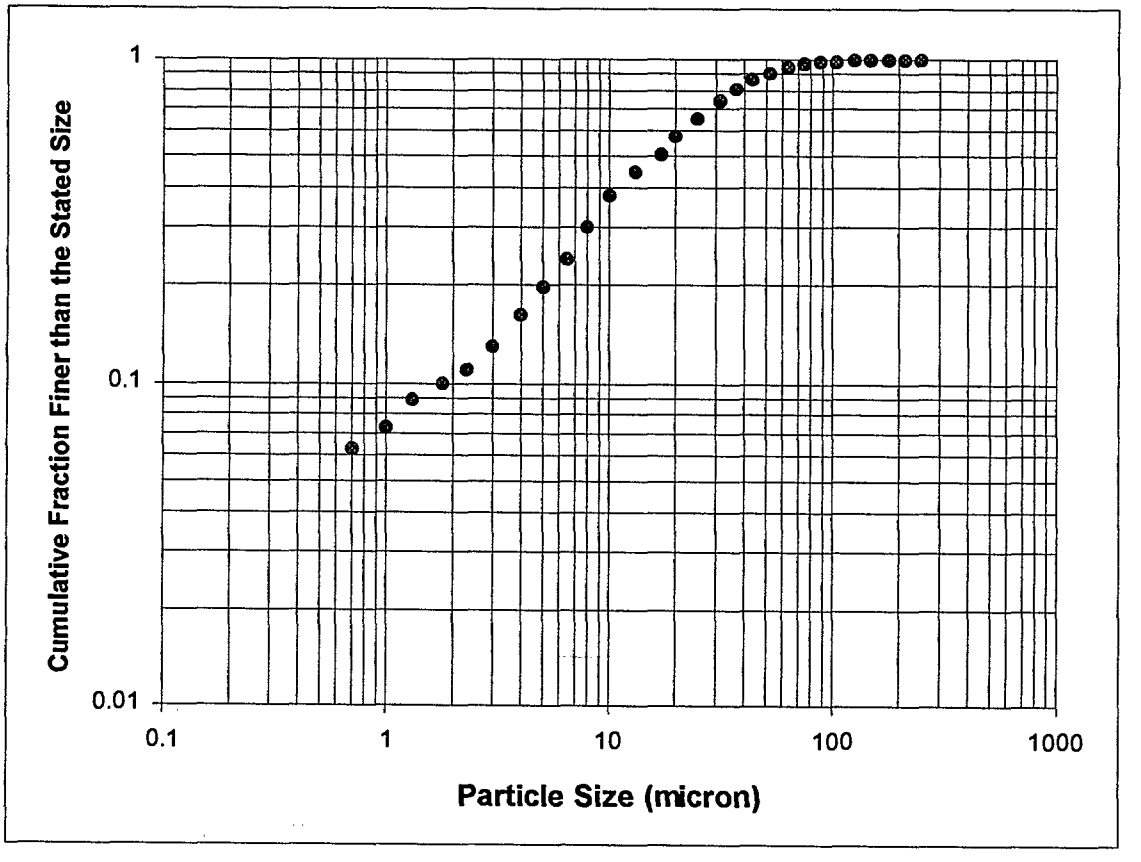

Figure 4.1. Spherical equivalent mean particle size distribution of the PuO_2 used in this study (number basis).

Without physical samples of narrowly sized PuO_2 for experimental purposes, these and other potentially interrelated effects could go unresolved. One solution to this problem was to sieve a sample of the

plutonium oxide described in Section 3.1 into ten narrowly sized fractions for the dissolution studies. Results of the sieving operation are presented in Table 4.1 and graphically in Figure 4.2. The size ranges presented in the table are interpreted as passing through the larger number screen and resting on the smaller number screen. For example; the sieve fraction designated as -15+10 is interpreted as passing through the 15 μm screen and resting on the 10 μm screen.

Table 4.1. Sieve Results from the ATM Sonic Sieve

Size Range (μm)	Amount Collected (grams)
<5	1.3004
-10+5	4.901
-15+10	9.3949
-25+15	10.4606
-38+25	4.9128
-53+25	1.488
-75+53	0.1773
-90+75	0.061
-125+90	0.095
>125	0.565
total	33.356

Samples of these different fractions were dissolved to determine the effect of particle size on dissolution rate and to determine the best heterogeneous model describing the dissolution of this high surface area PuO_2. Operating parameters were limited in these experiments; acid and iron

concentrations were fixed as was the temperature and the agitation rate as described previously in Section 3.1. Later, these experiments were compared with several dissolution experiments using the entire oxide particle assemblage.

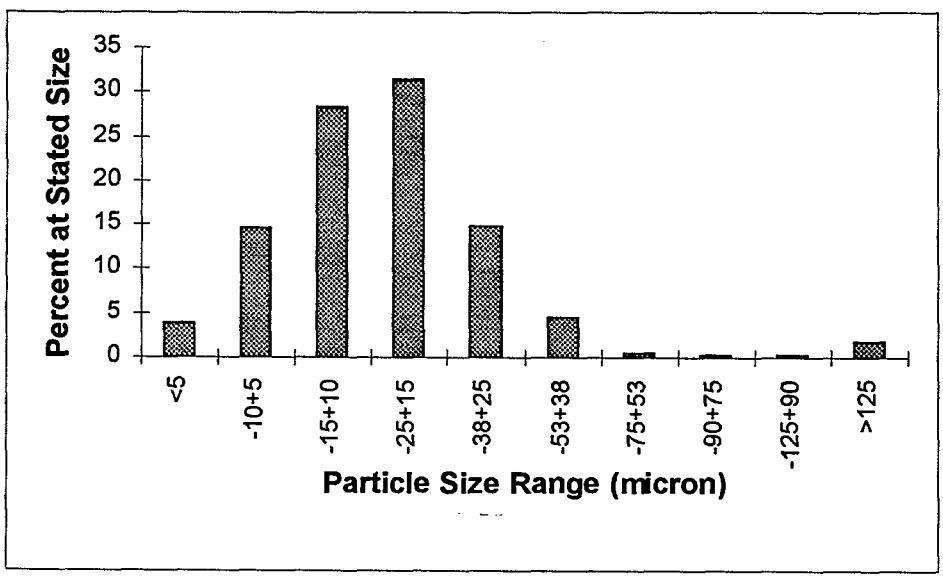

Figure 4.2 PuO_2 size distribution data from sieving (weight basis).

As discussed previously in Section 2.3.2, several heterogeneous models have been developed to describe fluid-solid reactions. It was not the intent of this research to develop a new description for the dissolution of PuO_2 if an adequate model already existed. Therefore, rate data from cyclic voltammogram peak height ratios were analyzed with the simple nonporous

shrinking spherical particle models where both film diffusion or surface reaction could be considered rate limiting. Again, these relationships are:

$$\frac{t}{\tau_{rxn}} = 1-(1-X)^{1/3} \tag{2.8}$$

for surface chemical reaction controlling;

$$\frac{t}{\tau_{spf}} = 1-(1-X)^{2/3} \tag{2.19}$$

for small particles in the Stoke's regime where Reynolds numbers are very low and film diffusion controls; and

$$\frac{t}{\tau_{lpf}} = 1-(1-X)^{1/2} \tag{2.28}$$

for the situation where film diffusion is controlling but the solid particles are large and the initial Reynolds number was high. In Eq. 2.8, 2.19, and 2.28, τ was the time required for complete dissolution of the particles and X was the extent of reaction or conversion at any time.

Evaluating and testing the applicability of these models consisted of plotting a modified reaction extent

$$\frac{t}{\tau} = 1-(1-X)^{n} \tag{4.1}$$

against time, where n was 1/3, 2/3, or 1/2 depending on the rate controlling step being tested. The more linear these plots were, the better the model represented the dissolution phenomena of PuO_2 in the HCl-Fe(II) system.

Figure 4.3 is an example of the result of plotting this modified reaction extent for the three models (note that all three models share the same point in time at the extremes of the experimental space; X = 0 and X = 1). Examining the data from an assemblage dissolution experiment (Figure 4.3) indicates that both surface reaction control and large particle film diffusion control may be appropriate to represent the data. In this particular case, however, the film diffusion control models have a more systematic deviation from linear behavior at early reaction times than the data representing surface chemical reaction control. Based on the systematic variation from linear behavior, it is concluded that representation by surface chemical reaction is the more accurate representation. It is also not surprising to see the surface reaction model deviate towards film diffusion control at larger values of X where the dissolution reaction times, in this example, are in excess of 140 min. For this reason, all regression analyses included only the early rate data, and did not include the last one to three data points in each series. See Appendix A for a description of the data points excluded from each experiment.

Figure 4.4 is a slightly different comparison of the three models against the actual experimental data. The model expressions were rearranged so that extent of reaction was in terms of time rather than the dissolution time being a function of extent. The resulting expressions for the various models took the general form

$$X = 1 - \left(1 - t/\tau\right)^{1/n} \tag{4.2}$$

In Eq. 4.2, t is the dissolution time and τ is the time required for complete dissolution of the material. In this case, τ is also the inverse of the slope of the appropriate linear regression line shown earlier in Figure 4.3. As before, n is the appropriate exponent for the model of interest; 1/3, 2/3, or 1/2, for surface reaction, Stoke's regime or small particle film diffusion, or large particle film diffusion control, respectively.

Although this is only a representative example of the dissolution of a sample of the oxide assemblage, it is typical of the results from all experiments completed in this program. From these results, it is concluded that surface chemical reaction controls the overall dissolution rate. It may be argued, however, that while the rate is initially governed by surface chemical reaction control; at later times film diffusion control begins to dominate, indicating that a mixed model may also be an appropriate representation of the entire dissolution phenomena.

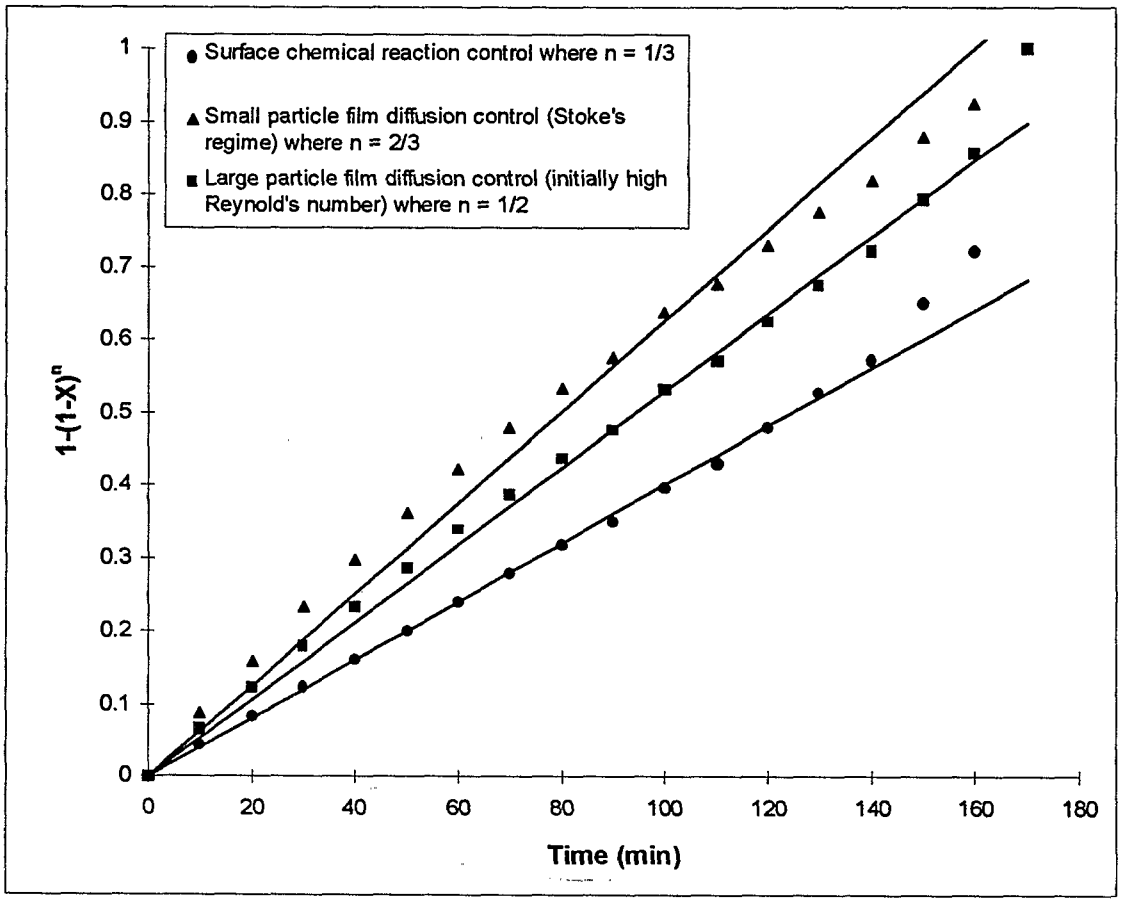

Figure 4.3. Linearization of experimental rate data showing the applicability of various nonporous shrinking sphere models.

This level of modeling complexity was avoided because of two major observations: at early reaction times, the dissolution phenomena was dominated by surface chemical reaction control as discussed previously; and there was also evidence of a large apparent activation energy for the reaction indicating that chemical reaction controls dissolution (see Section 4.3). It is also interesting to note that although the example shown in Figures 4.3 and

4.4 is a sample of the oxide assemblage with a definite particle size distribution as seen in Figure 4.1, the dissolution rate data in Figure 4.4 show no distinct nonlinearity at early dissolution times as might be expected with the smaller fractions dissolving easier and faster, by whatever method, than the larger fractions.

Although Table 4.2 excludes Arrhenius experiments for comparison, the table presents the results of the twenty eight 50°C experiments comprising the program and compares the results of sieve fraction dissolution with assemblage dissolution. In addition to recognizing the similarity in the value of the slope of the linearized surface chemical reaction controlled model between assemblage and sieve fraction experiments, the value of the linear correlation coefficient for the chemical reaction controlled model is generally higher and indicative of a better fit than either of the two film controlled models. This reason combined with the lack of systematic deviation from the regression line also promote the conclusion that for the majority of the dissolution reaction time (t < 140 min.), surface chemical reaction control best describes the dissolution reaction. After approximately 140 minutes, however, film diffusion control begins to dominate as evidenced by greater deviations of the reaction control model toward diffusion control (Figure 4.3).

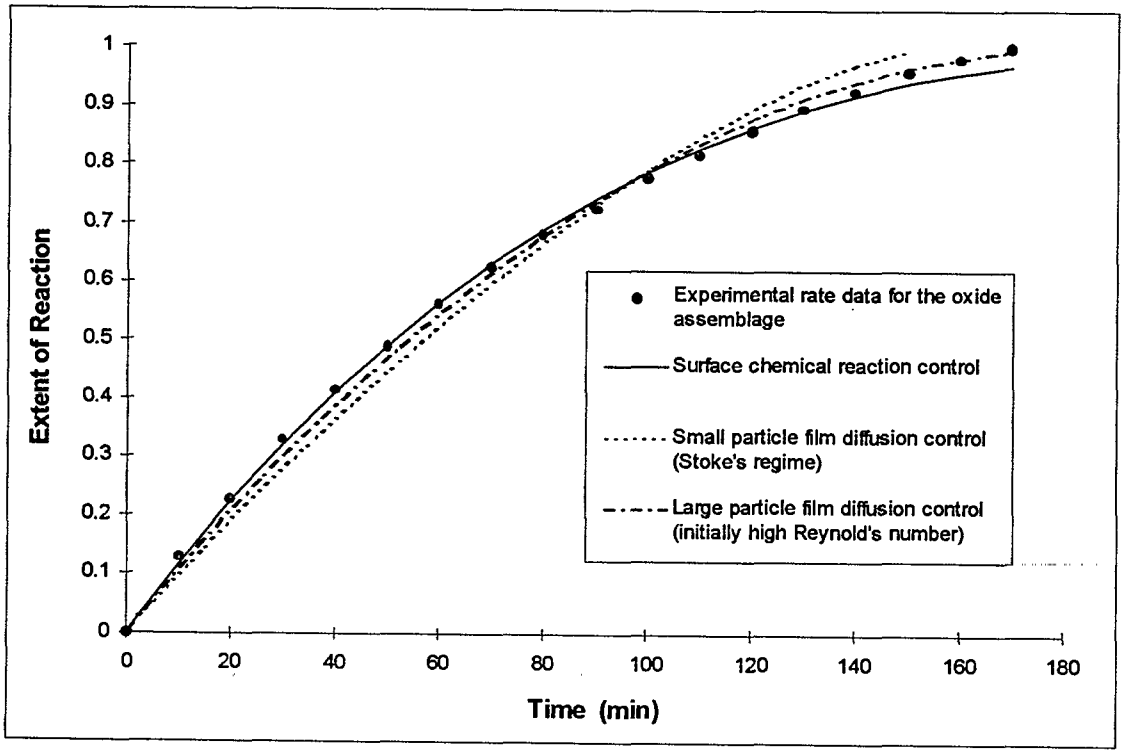

Figure 4.4. Comparison of nonporous shrinking sphere dissolution models with actual dissolution data for PuO_2 assemblage.

Table 4.2. Comparison of Linear Correlation Coefficients Between Chemical Reaction Control and Film Diffusion Control for the 50°C Dissolution Experiments.

Experiment Date	Particle Size Range (μm)	Surface Reaction Slope $(min)^{-1}$	Linear Correlation Coefficients		
			r^2_{rxn}	r^2_{spf}	r^2_{lpf}
1/18/96	<5	0.00441	0.997	0.982	0.997
1/17/96	-10+5	0.00480	0.993	0.952	0.982
2/14/96	-10+5	0.00370	0.995	0.986	0.996
2/15/96 am	-10+5	0.00468	0.982	0.979	0.990
2/26/96	-10+5	0.00398	0.994	0.954	0.981
1/16/96 pm	-15+10	0.00439	0.995	0.971	0.989
1/10/96 am	-15+10	0.00356	0.993	0.960	0.980
1/10/96 pm	-15+10	0.00454	0.995	0.987	0.993
2/28/96	-25+15	0.00459	0.994	0.966	0.990
2/13/96	-25+15	0.00409	0.995	0.968	0.994
1/9/96	-25+15	0.00446	0.996	0.966	0.990
2/27/96 pm	-38+25	0.00492	0.999	0.964	0.990
2/8/96	-38+25	0.00443	0.995	0.950	0.982
12/20/95	-38+25	0.00495	0.997	0.973	0.991
2/27/96 am	-53+38	0.00476	0.996	0.951	0.981
11/17/95	assemblage	0.00404	0.996	0.988	0.992
11/20/95	assemblage	0.00476	0.990	0.966	0.987
11/21/95	assemblage	0.00562	0.995	0.979	0.992
11/29/95	assemblage	0.00465	0.990	0.992	0.986
11/30/95	assemblage	0.00426	0.950	0.987	0.973
12/1/95	assemblage	0.00538	0.986	0.935	0.969
12/12/95	assemblage	0.00504	0.988	0.971	0.991
12/13/95 am	assemblage	0.00418	0.999	0.959	0.989
12/13/95 pm	assemblage	0.00366	0.998	0.967	0.990
12/19/95	assemblage	0.00435	0.997	0.981	0.997
1/16/96 am	assemblage	0.00400	0.999	0.980	0.995
2/15/96 pm	assemblage	0.00434	0.985	0.913	0.957
2/23/96	assemblage	0.00437	0.997	0.947	0.982

4.2 Particle Size Analysis

As described previously in Section 3.2.2, particle size distribution for the plutonium oxide used in this study was determined by two different methods. One was a transit time measurement based on scanning laser microscopy, while the other was physical separation by sifting the oxide through precision electroformed sieves into discrete particle size fractions. The results from the two techniques are shown in Figure 4.5 as a histogram comparing the two distributions.

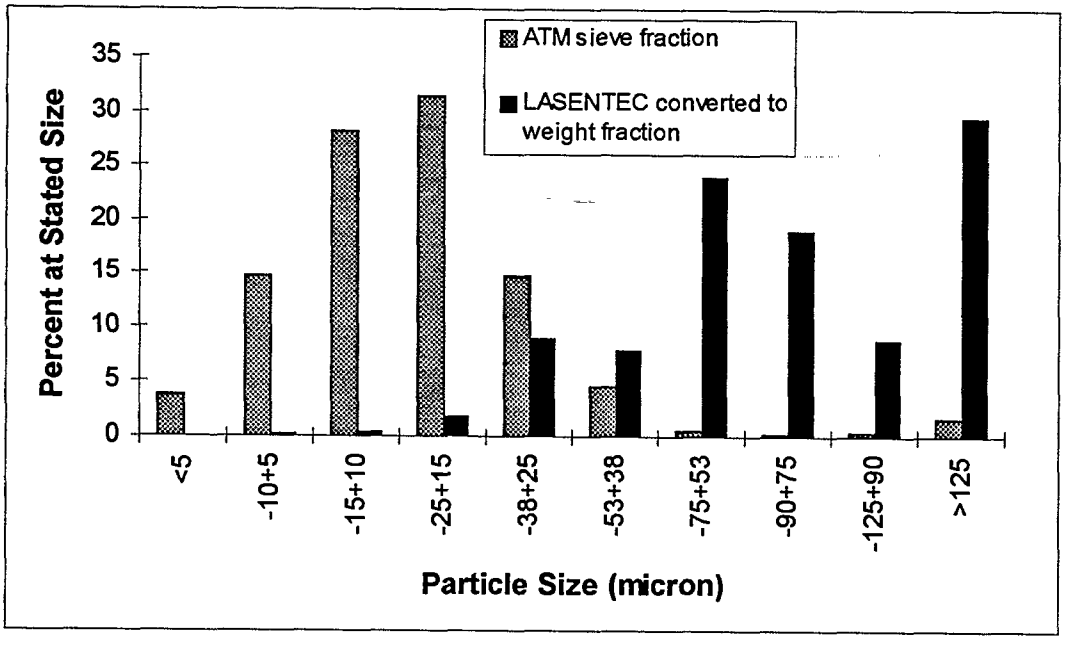

Figure 4.5. Particle size distribution data from scanning laser microscopy and dry sieving for the plutonium oxide assemblage used in this study.

Figure 4.5 compares the mass (or volume) distribution from the sieve analysis with a number distribution (spherical equivalent mean) that has been converted to mass (or volume). The difference between the two distributions is significant, but as mentioned in Section 3.2.2, it is not unusual to obtain different results from different instruments or techniques.

The PuO_2 for these experiments originated from the decomposition of plutonium oxalate at 400°C to 450°C, was extremely amorphous, and had a surface area of ~28 m^2/g. Examining Figure 4.6 shows the irregular, possibly delicate nature of the material, comprised of what appears to be small, loosely organized crystallites. The reason for the high surface area is evident, as well as a lack of organized structure indicative of precipitates not calcined to high temperature.

The transit time measurement technique for determining particle size distribution consisted of dispersing the representative sample in a dilute aqueous sodium pyrosulfate solution to eliminate agglomeration (Section 3.2.2), and slightly agitated prior to particle counting. This was in contrast to the sifting procedure where the oxide sample was subjected to sonic and mechanical forces causing material to pass through and collect on the various screens.

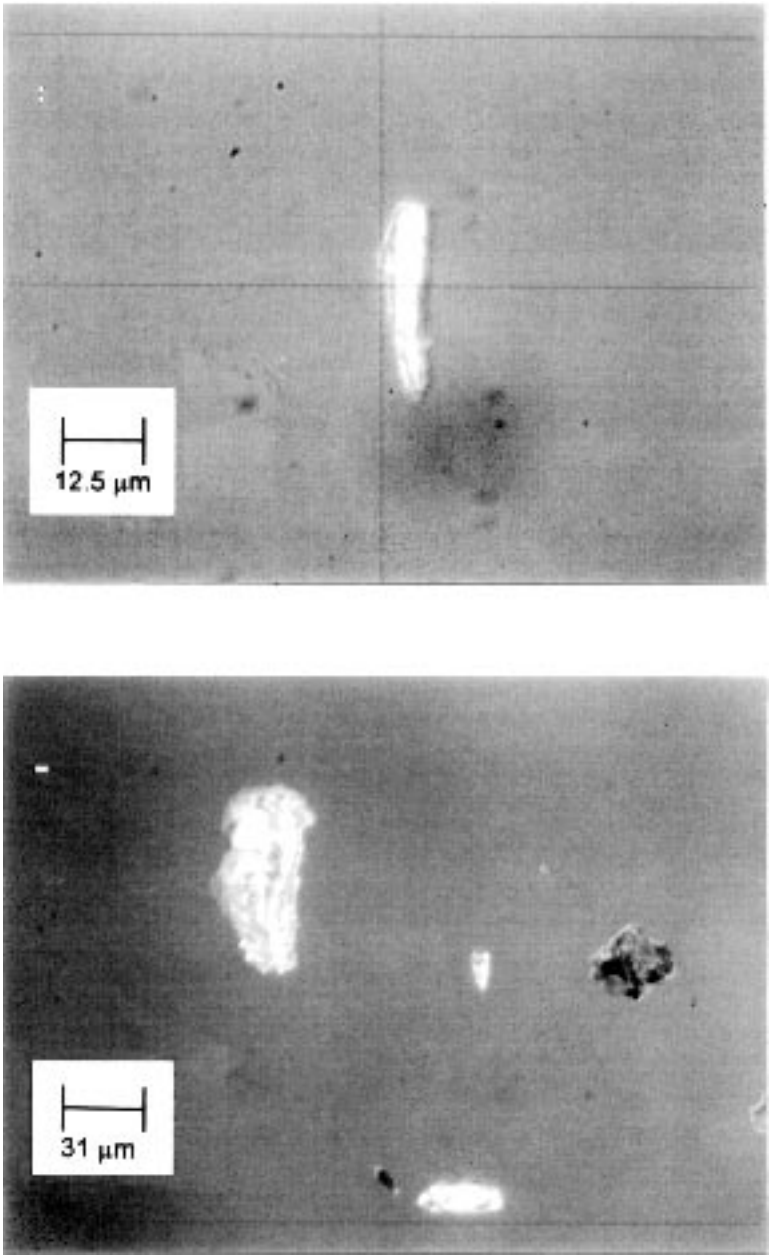

Fig.ure 4.6: Illustration of the amorphous and possible fragile nature of the PuO_2 used in this study.

In light of the possibility that dry segregation of this fine oxide material would be incomplete due to cohesive interparticle attraction (Section 2.6), samples of oxide produced from the ATM Sonic Sifter were submitted for analysis by scanning laser microscopy. Results from analyzing three separate screen fractions (-38+25 μm, -25+15 μm, and -15+10 μm) were obtained and the results presented in Figure 4.7 and Table 4.3 with the original oxide assemblage included for comparison. From Figure 4.7, it is evident that the discussion presented in Section 2.6 is applicable to some extent here, and further illustrates the enormous difficulty that powder handling technologists and other researchers have with fine, dry particle systems.

In examining Figure 4.7, the most apparent observation is that the dry sieving operation achieved no discrete segregation of the fine oxide powder assemblage. The similarity between the distributions of these sieve fractions compares very well with the original assemblage and further illustrates the problem of dry sieving fine powders. One observation that is unusual, however, is that in all three of the sieve splits, there is a significant fraction of oversize material present, with material sizes >3-4 times the diameter of the sieve openings being reported.

Since the distributions in Figure 4.7 are representations based on spherical equivalent mean number distributions, any needle-like structures

present in the samples may be represented as oversize fraction if the material were detected by the laser microscope in its major dimension. In addition, if cohesive interactive forces are significant, then small material on a given screen could conceivably interact to form stable oversize clusters or agglomerates. In this case, however, it is unlikely that either the frequency of formation of stable clusters would so closely duplicate the frequency of occurrence in the unsieved oxide assemblage; or that these newly-formed particles would be stable in the aqueous dispersion required for transit time particle size distributions.

The presence of needle-like structures orienting themselves parallel to the sonic field in the oscillating air column of the ATM sifter has been noted in previous work (Karuhn 1996) when using this instrument to separate foodstuffs. The work by Karuhn involved the dry sieving of foodstuffs where it was observed that a fiberous constituent was found to readily segregate from other nonfiberous bulk materials. Apparently, the combination of an oscillating air column and the sonic field produced an orientation that allowed these types of particles to migrate through progressively finer sieve openings.

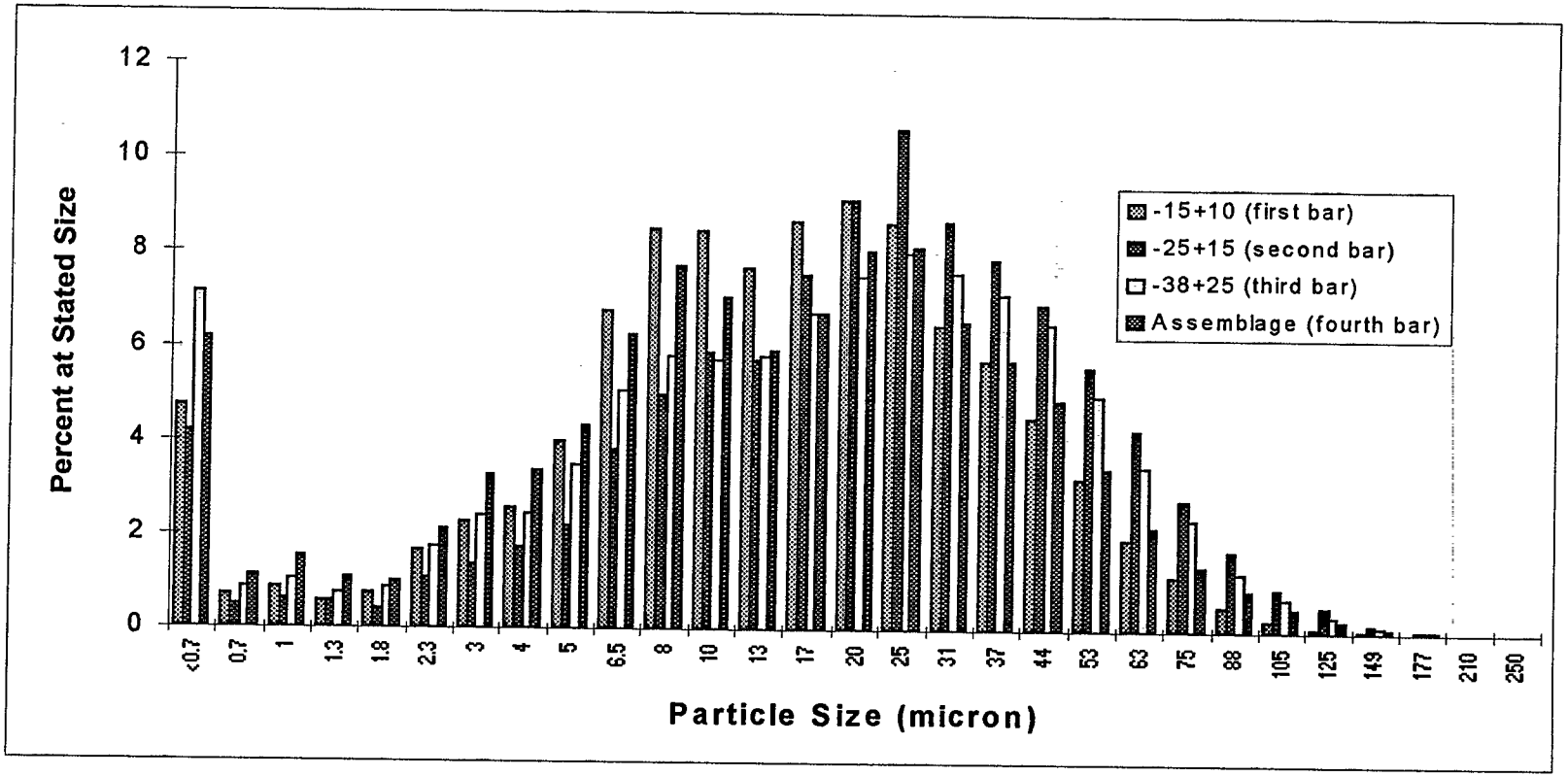

Figure 4.7. Scanning laser microscopy particle size distribution on discrete oxide fractions produced from sieving compared with the original assemblage (spherical equivalent mean number distribution).

Table 4.3: Spherical Equivalent Mean Particle Size Data for ATM Screen Fractions and the Original PuO_2 Assemblage.

overall mean size (μm)	20.9	23.6	23	22.5	21.9	30.8	26.7
Channel Size (μm)	Split 1 (%)	Split 2 (%)	Split 3 (%)	average (%)	-15+10 (%)	-25+15 (%)	-38+25 (%)
<0.7	7.549	5.3831	5.6752	6.2024	4.7279	4.1947	7.1497
0.7	1.1136	1.0401	1.1945	1.1160	0.7178	0.4862	0.8878
1	1.5821	1.4614	1.5949	1.5461	0.8834	0.6383	1.0458
1.3	1.0747	1.1156	1.075	1.0884	0.5995	0.5722	0.7644
1.8	1.0753	0.9831	0.969	1.0091	0.7478	0.4249	0.8806
2.3	2.1703	1.9918	2.1334	2.0985	1.6419	1.0697	1.7597
3	3.4277	3.059	3.3264	3.2710	2.2732	1.3852	2.3953
4	3.4106	3.346	3.3313	3.3626	2.5621	1.7455	2.4534
5	4.5266	4.27	4.1825	4.3263	3.9923	2.2003	3.4984
6.5	6.701	5.9831	6.1178	6.2673	6.7752	3.8236	5.0819
8	8.3412	7.2773	7.5797	7.7327	8.494	4.9898	5.7972
10	7.4375	6.9867	6.7734	7.0658	8.4541	5.8938	5.7147
13	6.1549	6.0239	5.6268	5.9352	7.664	5.7219	5.8111
17	6.681	6.7896	6.7559	6.7421	8.6729	7.5472	6.7073
20	7.6463	8.1042	8.4344	8.0616	9.1336	9.1357	7.5115
25	7.3765	8.5044	8.5785	8.1531	8.6315	10.611	7.9944
31	5.9266	7.0502	6.6742	6.5503	6.4967	8.6741	7.5941
37	5.3391	6.0249	5.8872	5.7504	5.7176	7.8949	7.1454
44	4.6367	5.0865	5.0288	4.9173	4.529	6.9291	6.5103
53	3.1851	3.5503	3.5418	3.4257	3.254	5.6189	4.9854
63	2.1045	2.3527	2.1823	2.2131	1.9558	4.2829	3.4935
75	1.2312	1.4807	1.4592	1.3903	1.1531	2.7667	2.3705
88	0.7454	1.0008	0.8857	0.8773	0.5503	1.6899	1.2415
105	0.3494	0.608	0.5324	0.4966	0.2453	0.9314	0.6892
125	0.1526	0.3283	0.2887	0.2565	0.093	0.5315	0.3526
149	0.0473	0.1328	0.1242	0.1014	0.0266	0.1847	0.1245
177	0.0109	0.0465	0.0308	0.0294	0.004	0.0405	0.0224
210	0.0019	0.0123	0.0112	0.0084	0.0006	0.0105	0.0051
250	0.0007	0.0067	0.0047	0.0040	0.0001	0.005	0.003
total	99.999	100.00	99.999	99.9998	99.997	100.00	99.991

The PuO_2 used in this study was observed with needle-like structure present in the assemblage. Figure 4.8 is a micrograph where it can be clearly seen that this type of structure was present. This information in conjunction with evidence presented in Section 2.6 regarding the cohesive interparticle attraction of fine materials lend credibility to the particle size distributions presented in Figure 4.7 and Table 4.3.

4.3 Kinetic Analysis

In spite of the difficulty in obtaining sieve fractions of near mono-size oxide to determine the effect of particle size on the dissolution rate, dissolution experiments with the sieve fractions were performed and compared with data from the original assemblage to provide additional confirmation that segregating the original assemblage was not possible by dry sieving. In addition, Arrhenius experiments on the oxide assemblage were performed at five additional temperatures to determine the apparent activation energy of the dissolution reaction for comparison with literature values.

Without any prior knowledge of a reacting fluid-particle system, one might expect to observe an increase in reaction rate as a function of the increased surface area available from a large fraction of small particles in a given powder assemblage.

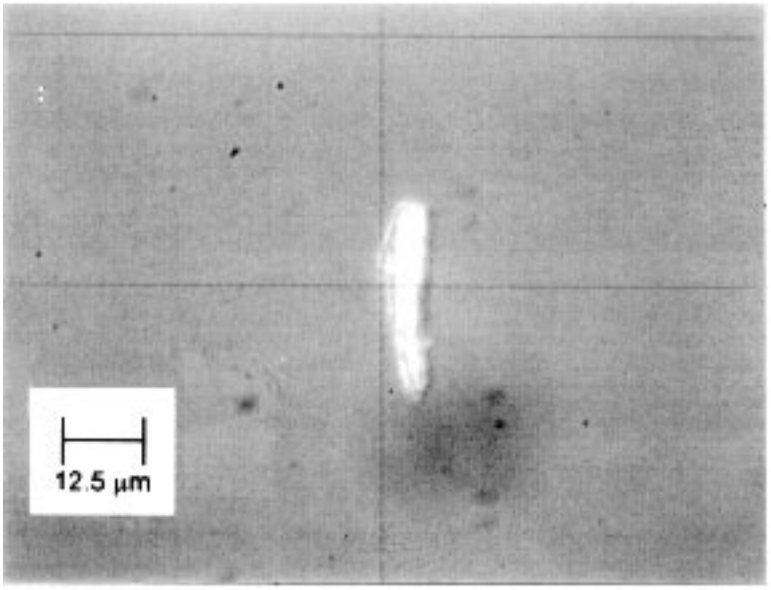

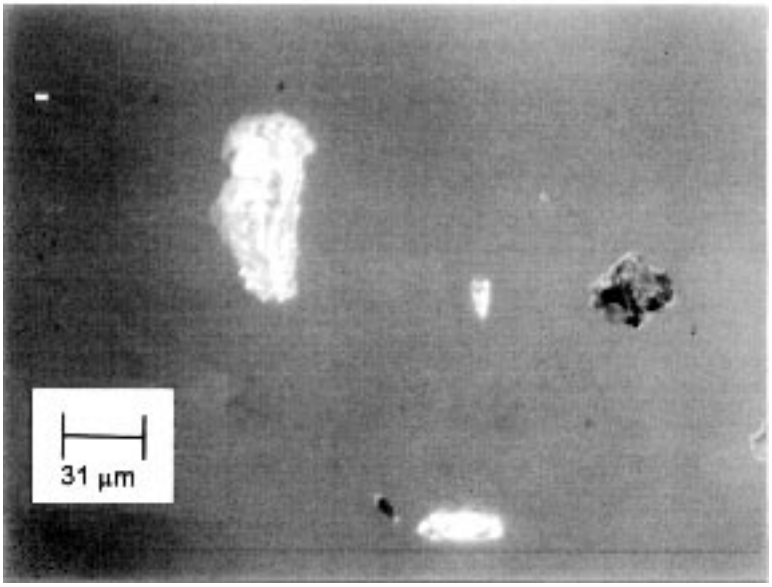

Fig.ure 4.8: Appearance of needle-like structures in the original PuO_2 particle assemblage.

From Eq. 2.8

$$\tau_{rxn} = \frac{\rho_B R}{b k_s C_{Af}} = \frac{1}{m} \tag{4.3}$$

where m is the slope of the linearized rate expression.

Examining Eq. 4.3 indicates that

$$m = \frac{const}{R} \tag{4.4}$$

As the nominal particle size, R of the sample decreases, therefore, the value of m should increase. To test this hypothesis, the sieve fractions were evaluated separately and compared with the dissolution behavior of the oxide assemblage. Overall, however, the phenomena of an increase in dissolution rate being inversely proportional to the particle size was not observed. There were differences in the behavior of the different sieve fractions and the assemblage, but they were not systematic nor were they consistent throughout the range of size fractions examined, and were attributed to experimental variability. Figure 4.9 illustrates the difference in the slope of the linearized rate data (assuming surface reaction control) from the various sieve fractions and includes the results of an assemblage experiment for comparison. Figure 4.10 presents the same data in a slightly different form and further illustrates the similarity between the extent of dissolution of the oxide assemblage and the different size sieve fractions.

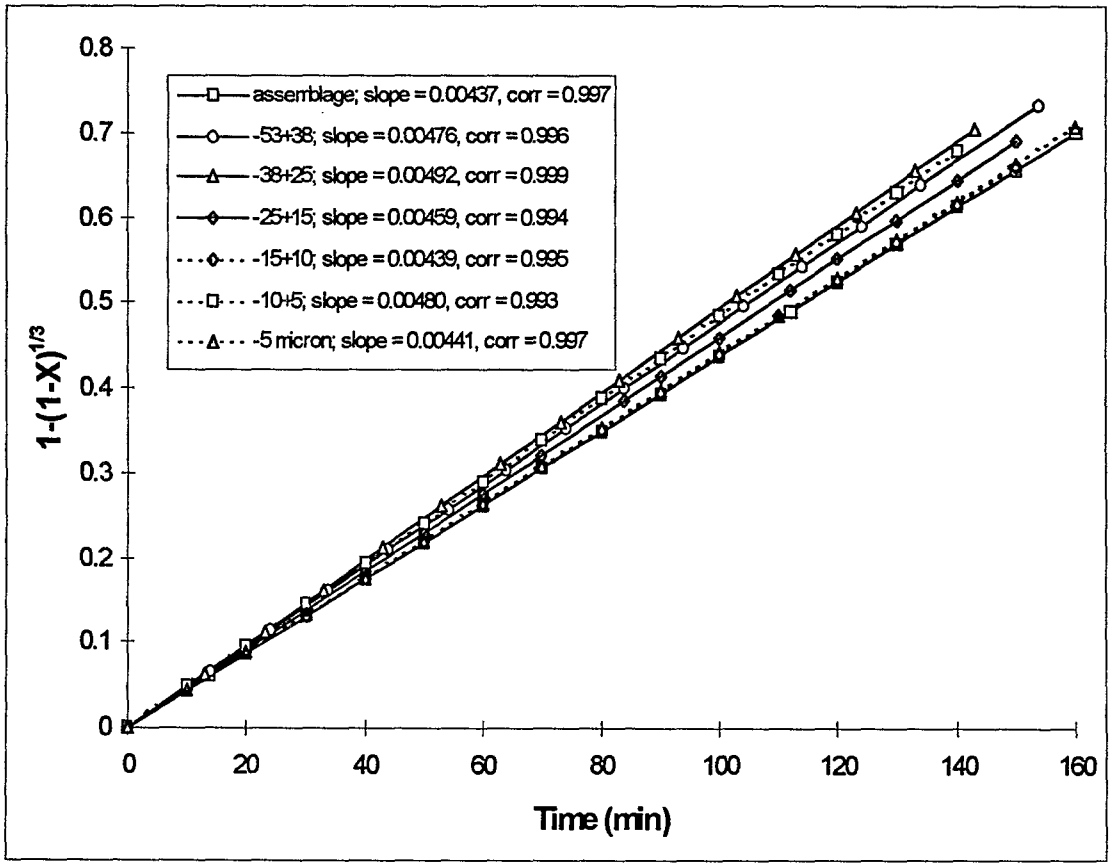

Figure 4.9. Assuming surface chemical reaction control, this figure illustrates the difference in the slope of the linearized rate expression among the varying oxide particle sizes compared with the oxide assemblage.

The lines connecting data in Figure 4.10 were determined using the surface reaction controlled model and plotting Eq. 4.2 against time; where τ_{rxn} was the evaluated as the inverse of the slope of the linearize data taken from Figure 4.9.

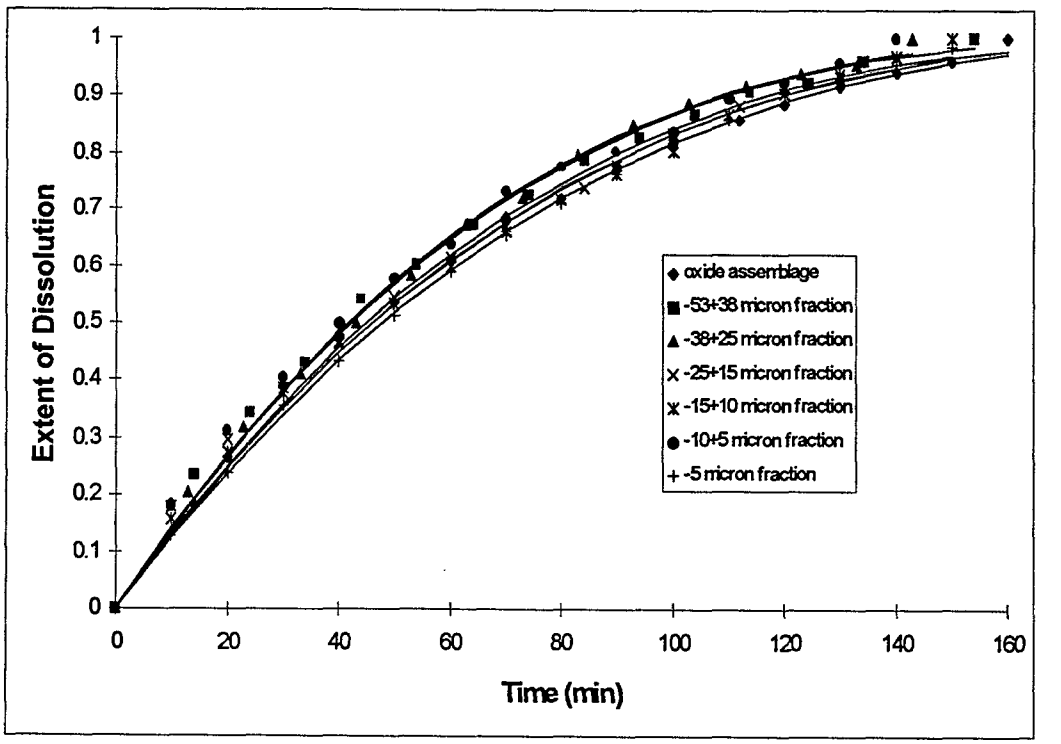

Figure 4.10. The extent of dissolution of varying oxide particle size fractions compared with the entire plutonium oxide assemblage.

Because the dissolution performance of these oxide fractions were so similar, the case for enhanced data quality became important in performing further data reduction and analysis to see whether a particle size influence on the dissolution rate might be hidden in noisy data. As discussed previously in the Procedure (Section 3.3), several factors could adversely affect the cyclic voltammograms used to describe the rate data; most notable of these were lack of adequate temperature control and a progressive and

sometimes subtle fouling of the surface of the precision area working electrode.

The experimental program for evaluating the dissolution performance of this oxide assemblage and the various sieve fractions consisted of 28 dissolution experiments (see Appendix A for a description of the individual experiments); thirteen were conducted on the assemblage and fifteen on the various sieve fractions. Of these 28 experiments, eleven were determined to be of substandard quality and were rejected from the data set (reasons for their rejection are also included in Appendix A). Results of this data quality screen are shown in Figures 4.11 and 4.12. These figures show the slope of the linearized rate data obtained from the surface reaction control expression for the various experiments plotted against the screen fraction of the oxide used in the experiment. Figure 4.11 shows the slope data from the entire 28 experiments; while Figure 4.12 shows the results after eliminating data based on its apparent, yet subjective overall quality. The confidence interval on Figure 4.12 was derived from the variability of the seven surviving assemblage experiments and can be written for the slope of the surface chemical reaction controlled model as:

$$\text{95\% Confidence Interval: } 0.004186 \leq m_{rxn} \leq 0.004685 \qquad (4.5)$$

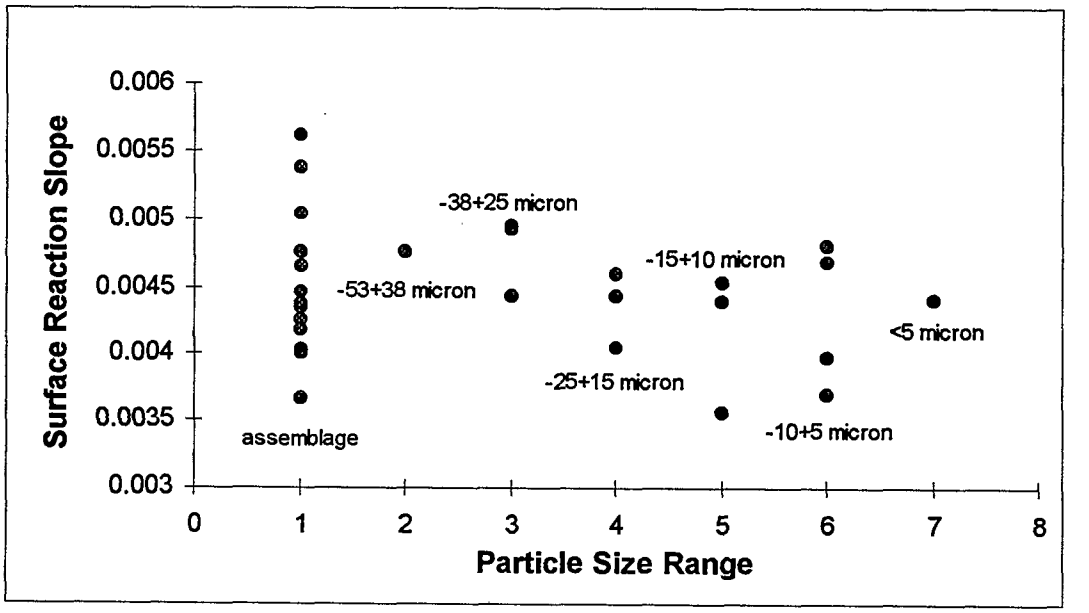

Figure 4.11. Values of the slope for surface chemical reaction control from all experiments showing data variability.

Although the confidence interval given by Eq. 4.5 and illustrated graphically in Figure 4.12 does not bracket the entire set of sieve fraction dissolution data, examining the set of surviving experimental runs indicates that slope data from the sieve fractions does not exhibit any type of generally increasing trend as predicted by Eq. 4.4. In fact, a general comparison of all of the data, including the assemblage experiments indicate that there is little, if any difference between the dissolution behavior of the oxide sieve fractions and the oxide assemblage itself.

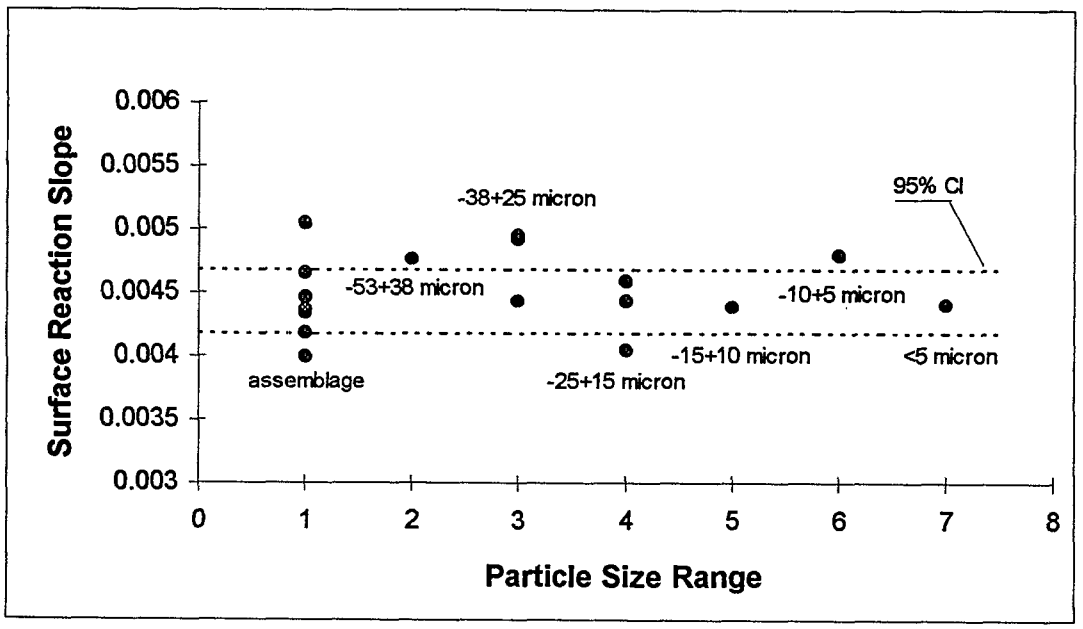

Figure 4.12. Results of screening surface reaction controlled slope data from all experiments for data quality problems. Included is the 95% confidence interval determined from the standard error in the assemblage experiments.

This comparison, and the lack of any increase in slope as the particle size decreases further illustrates the inability to dry segregate this oxide as previously shown in Figure 4.7. Although it appears that dry sieving was not an effective method for segregating this oxide into mono-size fractions, it also might be concluded from the dissolution behavior of the assemblage material, that segregation for kinetic purposes may not have been necessary.

Prior to initiating the experimental program, one of the original hypotheses was that in order to study the fundamental nature of PuO_2 dissolution kinetics, the effect of particle size had to be eliminated. This was

necessary in order to test several models such that the best fit of the experimental data would lead to the most appropriate model for describing the phenomena. Sieving into near mono-size fractions was the apparent solution to this hypothesized problem. After the experimental program was completed, however, analysis of the data indicated no difficulty with representing this fine particle assemblage with the simple surface chemical reaction controlled model since no apparent nonlinearity at early reaction times was observed that would indicate that small particle fractions might be influencing or confusing analysis of the rate data (Figure 4.3) .

In spite of not being able to successfully sieve the oxide, scanning laser microscopy as well as independent kinetic information confirmed no real difference in the particle size distributions between the screen fractions and the original assemblage (see Table 4.3 and Figure 4.7). The data presented in Table 4.2 and the systematic deviation of experimental data from the linearized form of the film control models shown in Figure 4.3 both indicate that surface chemical reaction control was the best description of the dissolution process for all experiments in the program.

Table 4.4 presents an evaluation of all experimental slope data using simple statistics. Computing the average slope for all 28 experiments shown in Figure 4.11 and comparing it to the average of the 17 surviving experiments after screening the data (Figure 4.12) and the average of the 13

assemblage experiments (Figure 4.11) illustrates essentially no difference among the values ($\overline{m_{all}}$ = 0.00448 min^{-1}; $\overline{m_{surv}}$ = 0.00452 min^{-1}; $\overline{m_{assembly}}$ = 0.00444 min^{-1}).

The only effect eliminating some of the experimental data had towards improving data quality was in reducing the standard error of the data spread. The 17 surviving experiments had a 30% - 40% lower standard error than the entire set of 28 experiments.

Table 4.4. Comparison of Slope Data from the Linearized Surface Chemical Reaction Expression for All Experiments and the Calculation of First Order Rate Constants.

Parameter	All Data	Assemblage Data	Survivor Data
Average Slope for Surface Chemical Reaction (min^{-1})	0.00448	0.00444	0.00452
Standard Deviation of Slope Data (min^{-1})	0.000485	0.000337	0.000304
Calculated Rate Constant (cm/sec)$\cdot 10^5$	3.38±0.37	3.35±0.25	3.41±0.23

Also included in Table 4.4 is a calculation of the rate constant from the average slope values and using the value of τ_{rxn} defined earlier in Section 2.3.2.1 as well as by Eq. 4.3. In the calculation, the initial radius was estimated as the average of the six sets of data presented in Table 4.3 (the mean diameter of the three sieve fractions as well as three repeat analyses

of the same sample of assemblage material). The average particle diameter was found to be 24.5 μm with a standard deviation of 3.7 μm from the six sets of data. In calculating the first order rate constant:

$$\tau_{rxn} = \frac{\rho_B R}{b k_s C_{Af}} = \frac{1}{m} \tag{4.3}$$

where ρ_B = molar density of PuO_2 in the solid material (mol/cm^3; estimated from the molecular weight (271 g/mol) and the bulk density (~2g/cm^3) to give a molar density of $7.38 \cdot 10^{-3}$ mol/cm^3).

R = initial particle radius (cm; estimated as 24.5 μm = $2.45 \cdot 10^{-3}$ cm).

b = stoichiometric ratio (moles of solid PuO_2 reacted per mole of Fe(II) reactant (from Eq. 1.1 and Eq. 2.5, this value is 1.0)).

k_s = first order rate constant for the surface reaction (cm/sec).

C_{Af} = bulk solution concentration of Fe(II), (mol/cm^3; and from Eq. 1.1 and Eq. 2.5 this value is 0.04 *M*).

Applying these values to Eq. 4.3 and converting the slope of the linearized surface reaction controlled expression to seconds yields:

$$k_s = \frac{m(7.38 \cdot 10^{-3})(2.45 \cdot 10^{-3})1000}{0.04 \cdot 60} = (7.534 \cdot 10^{-3})m \tag{4.6}$$

This expression was used to calculate the rate constants presented in Table 4.4.

Further examination of the data presented in Table 4.4 indicates no real significant difference in the rate constants calculated from the various subsets of the experimental data. Attempts to conduct a more thorough data screening apparently did not affect the overall quality of the final calculation to any large extent. As suspected after particle size distributions were determined on the various sieve splits (Figure 4.7), the kinetic evaluations confirmed the observation that dry sieving was not effective in segregating this material. Table 4.5 is presented to illustrate the surface reaction slope data for all 28 experiments presented earlier in Figure 4.11. Also included is an indication of whether the data were rejected or used in Figure 4.12.

Throughout this experimental analysis the default variable for comparison has been the slope of the linearized surface chemical reaction controlled rate expression. This has been in part, due to the slightly better fit offered by this relationship compared with the film diffusion controlled models as presented earlier in Figure 4.3 and Table 4.2. This assumption was also further verified by a nonlinear least squares technique (Mason, Gunst, and Hess 1989) and the classical Arrhenius analysis.

Nonlinear least squares was performed on Eq. 4.2 for surface chemical reaction control and compared to several of the experimental data sets found in Appendix A.

$$X = 1 - \left(1 - t/\tau\right)^{1/n} \tag{4.2}$$

The intent was to compare the values of $1/n$ and τ with the values obtained from the linearized form of the surface chemical reaction controlled model. Significant deviation from values predicted by the model would indicate a potential error in the conclusion that oxide dissolution was indeed surface chemical reaction controlling. Table 4.6 is a summary of the data comparing the nonlinear least squares results with the values predicted by the surface reaction controlled model.

The experimental data chosen for Table 4.6 were selected at random for this comparison. Although there is scatter among the various experiments, this reflects the scatter shown previously in Figures 4.11 and 4.12. Comparison, however, of the nonlinear least squares parameters with the parameters derived from the linearization of the surface reaction model generally compare well and support the conclusion that surface chemical reaction governs the dissolution process.

Table 4.5. All Data for the Slope of the Surface Reaction Relationship for the Dissolution of Various PuO_2 Sieve Fractions and the Oxide Assemblage.

Particle Size Range (μm)	Surface Reaction Slope $(min)^{-1}$	Linear Correlation Coefficient	Status
<5	0.00441	0.997	
-10+5	0.00480	0.993	
-10+5	0.00370	0.995	reject
-10+5	0.00468	0.982	reject
-10+5	0.00398	0.994	reject
-15+10	0.00439	0.995	
-15+10	0.00356	0.993	reject
-15+10	0.00454	0.995	reject
-25+15	0.00459	0.994	
-25+15	0.00409	0.995	
-25+15	0.00446	0.996	
-38+25	0.00492	0.999	
-38+25	0.00443	0.995	
-38+25	0.00495	0.997	
-53+38	0.00476	0.996	
assemblage	0.00404	0.996	reject
assemblage	0.00476	0.990	reject
assemblage	0.00562	0.995	reject
assemblage	0.00465	0.990	
assemblage	0.00426	0.950	reject
assemblage	0.00538	0.986	reject
assemblage	0.00504	0.988	
assemblage	0.00418	0.999	
assemblage	0.00366	0.998	reject
assemblage	0.00435	0.997	
assemblage	0.00400	0.999	
assemblage	0.00434	0.985	
assemblage	0.00437	0.997	

Table 4.6. Comparison of Parameters Obtained from Linearizing the Surface Reaction Control Model with Parameters Obtained from Nonlinear Least Squares Estimation

Experiment	Sieve Fraction	$1/n_{rxn}$	τ_{rxn} (min)	$1/n_{nlls}$	τ_{nlls} (min)	ssq_{resid}
1/18/96	-5 μm	3	227	2.44	197	0.0016
1/17/96	-10+5 μm	3	207	4.32	271	0.0059
1/16/96 pm	-15+10 μm	3	228	3.10	229	0.0066
2/13/96	-25+15μm	3	244	3.06	252	0.0042
12/20/95	-38+25 μm	3	202	3.08	203	0.0064
2/27/96 am	-53+38 μm	3	210	4.22	269	0.0031
1/16/96 am	assemblage	3	250	2.59	222	0.0022
2/23/96	assemblage	3	229	4.13	289	0.0032
11/20/95	assemblage	3	218	5.23	337	0.0087
12/1/95	assemblage	3	186	4.06	230	0.0119
2/15/96 am	assemblage	3	213	2.63	202	0.0059

Parametric values close to 1.5 or 2.0 for the value of $1/n_{nlls}$ would have reflected Stoke's regime diffusion control for small particles or large particle film diffusion control, respectively. The sum of squares of the residuals, ssq_{resid}, was calculated from the sums of the squares of the differences

between experimental extents of reaction and the extents calculated from Eq. 4.2; where both $1/n_{nils}$ and τ_{nils} were varied until ssq_{resid} was minimized.

An illustration of the difference in the fitted data between the two techniques is presented in Figure 4.13. The data illustrated in the figure are from the poorest quality experiment evaluated and presented in Table 4.6. In spite of the difference between the two models, it can still be argued that there is no real difference between the underlying dissolution rate controlling mechanism used to describe the phenomena. The difference between the two data fitting techniques is due solely to the poor quality of the raw experimental data (see Appendix A for the voltammogram and the experimental data).

Figure 4.14 is a plot of residuals between the experimental extent of reaction and the extent of reaction calculated from the linearization of the reaction control model. There is an apparent trend in the five data sets presented in the figure that may indicate a more complex nature to the dissolution phenomena. Although the deviations are small, generally less than ±3%, there are three regions of interest in the figure. The region between 0 minutes and ~60 minutes where the model tends to under estimate the experimental values; the region between ~60 minutes and ~130 minutes, where the model over estimates the experiment; and the latter

stages of the dissolution reaction after ~130 minutes where the model again under estimates the experiment.

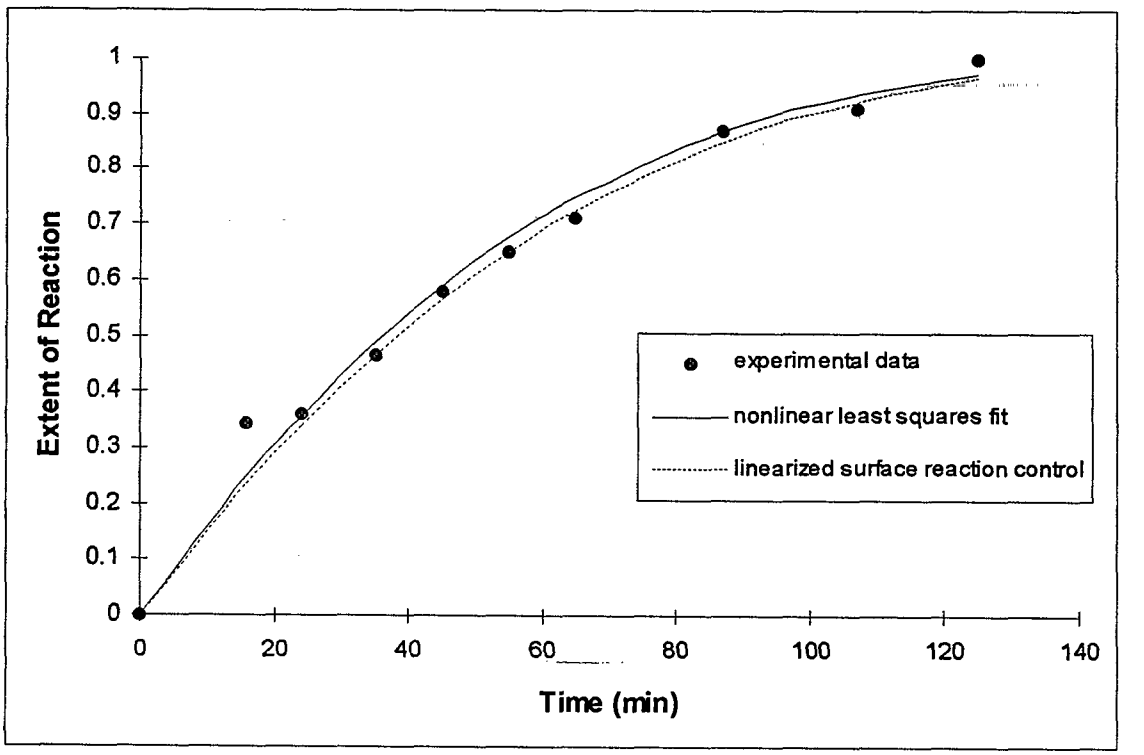

Figure 4.13: Comparison of nonlinear least squares and linearized surface reaction models with experimental data for December 1, 1995.

The phenomena occurring in the first region is why the model slightly over estimates in the second region; whereas the under estimation in the final region is due to the change in reaction mechanism from surface reaction control to a diffusion controlled mechanism.

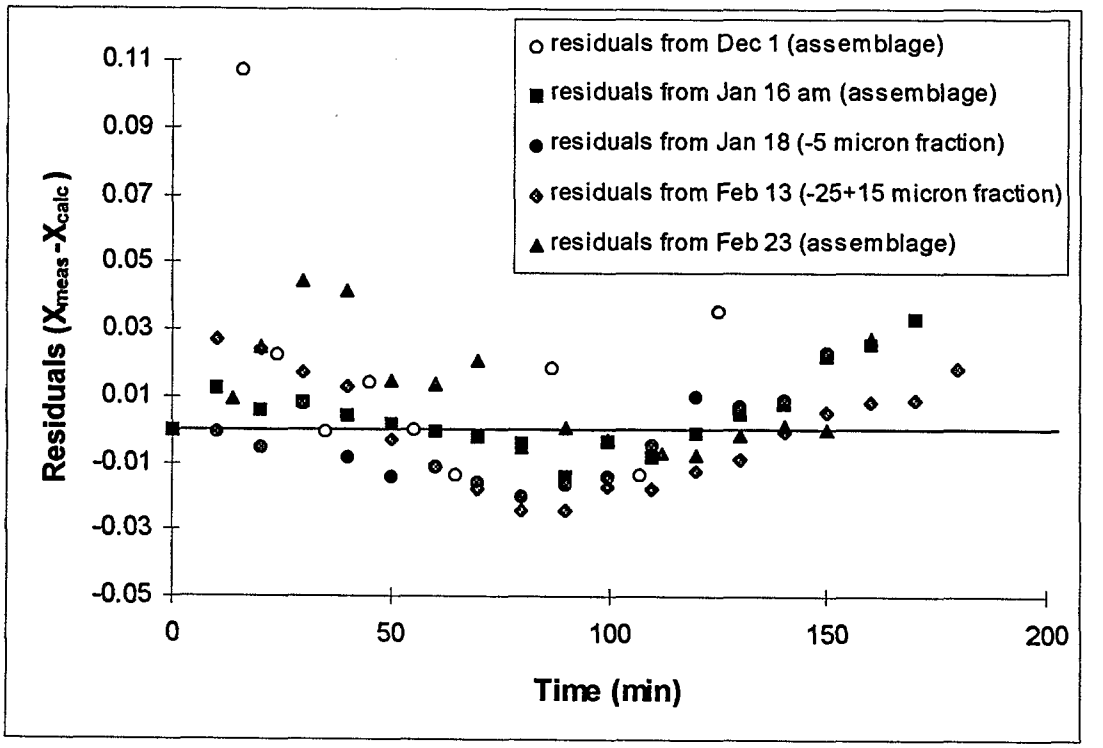

Figure 4.14. A plot of residuals from five sets of data presented previously in Table 4.4.

The model under estimation occurring in the first region can be attributed to a combination of a slight temperature overshoot in the early stages of an experiment leading to an increase in dissolution rate, and an increase in the rate due to dissolution of the fines fraction present in the oxide source (Figure 4.1 indicates ~10% of the oxide had a size <2 μm). Irrespective of the dominant cause, the slight increase in dissolution rate early in an experiment combined with a change in mechanism late in the experiment causes the linear model to compensate; under estimate in the

early and late stages of the experiment, and over estimate values in the middle region. These overall deviations, however, are small and the dissolution phenomena can still be very adequately represented by surface chemical reaction control.

A final indication that the rate controlling mechanism for PuO_2 dissolution is surface chemical reaction control comes from the classic Arrhenius analysis. In addition to better defining the complete rate equation, the magnitude of the activation energy E_a, can be used to indicate the rate controlling mechanism of the reaction (see Section 2.4). Machuron-Mondard (1990) and Barney (1976) reported activation energies for the plutonium oxide dissolution reaction to be 65 kJ/mol and 54 kJ/mol, respectively. Both of these values are much higher than ~40 kJ/mol, which has been described as the end of the transition region between diffusion control and surface reaction control as the rate limiting step for this type of reaction (Habashi 1969, Terry 1983, Machuron-Mondard 1990).

For the Arrhenius evaluation, dissolution experiments were conducted at 6 temperatures, 28°C, 40°C, 50°C, 60°C, 65°C, and 75°C using the entire oxide assemblage as the feed material. Other conditions were constant as described previously in the experimental procedure (Section 3.1). Figure 4.15 and Table 4.7 shows the results of the linearizing the Arrhenius relationship (Eq. 2.53) using a rate constant evaluated from the slope of the chemical

reaction controlled rate expression. The data in the figure suggest that at the higher temperatures, maybe >60°C, the reaction becomes diffusion controlled.

Table 4.7. Surface Chemical Reaction Control Rate Constants at the Various Arrhenius Temperatures

Temp (°C)	Slope from Linearized Rate Expression, m	$k_s = (7.534 \cdot 10^{-3}) \cdot m$	ln k_s
28	0.00038	$2.86 \cdot 10^{-6}$	-12.77
28	0.00056	$4.20 \cdot 10^{-6}$	-12.38
40	0.00154	$1.16 \cdot 10^{-5}$	-11.36
40	0.00131	$9.87 \cdot 10^{-6}$	-11.53
50	0.00465	$3.50 \cdot 10^{-5}$	-10.26
50	0.00504	$3.80 \cdot 10^{-5}$	-10.18
50	0.00418	$3.15 \cdot 10^{-5}$	-10.37
50	0.00447	$3.37 \cdot 10^{-5}$	-10.30
50	0.00400	$3.01 \cdot 10^{-5}$	-10.41
50	0.00434	$3.27 \cdot 10^{-5}$	-10.33
50	0.00437	$3.29 \cdot 10^{-5}$	-10.32
60	0.00759	$5.72 \cdot 10^{-5}$	-9.769
65	0.01104	$8.32 \cdot 10^{-5}$	-9.394
75	0.01241	$9.35 \cdot 10^{-5}$	-9.277

Several analyses of the data from Table 4.7 are presented in Table 4.8 for different temperature ranges in an attempt to determine the transition temperature region between chemical reaction and diffusion control. From the data in Table 4.8 and Figure 4.15, it appears the transition region is

greater than 50°C, therefore providing additional supporting evidence to the conclusion that the oxide dissolution reaction is surface chemical reaction controlled.

Table 4.8. Values of the Apparent Activation Energy for Different Oxide Dissolution Temperature Ranges.

Temperature Range	Apparent Activation Energy (kJ/mol)	Linear Correlation Coefficient
28°C – 50°C	84.4±1.9	0.982
28°C – 65°C	76.6±2.2	0.971
50°C – 75°C	43.1±2.0	0.944
60°C – 75°C	28.9±8.0	0.792

The apparent activation energy representing the largest temperature range (28°C – 65°C), is calculated to be 76.6±2.2 kJ/mol which is well within the surface chemical reaction controlled regime discussed previously in Section 2.4. The intercept when linearizing these data in this temperature range is the pre-exponential factor k_o defined earlier in Eq. 2.53, and can be calculated as $5.95 \cdot 10^7$ cm/sec. The uncertainty in the activation energy values presented in Table 4.8 represent the 95% confidence interval on the slope from linear regression models considering the four different temperature ranges. It is also not surprising that the magnitude of these uncertainty values would also follow directly, the trend established by the linear correlation coefficients reported in Table 4.8.

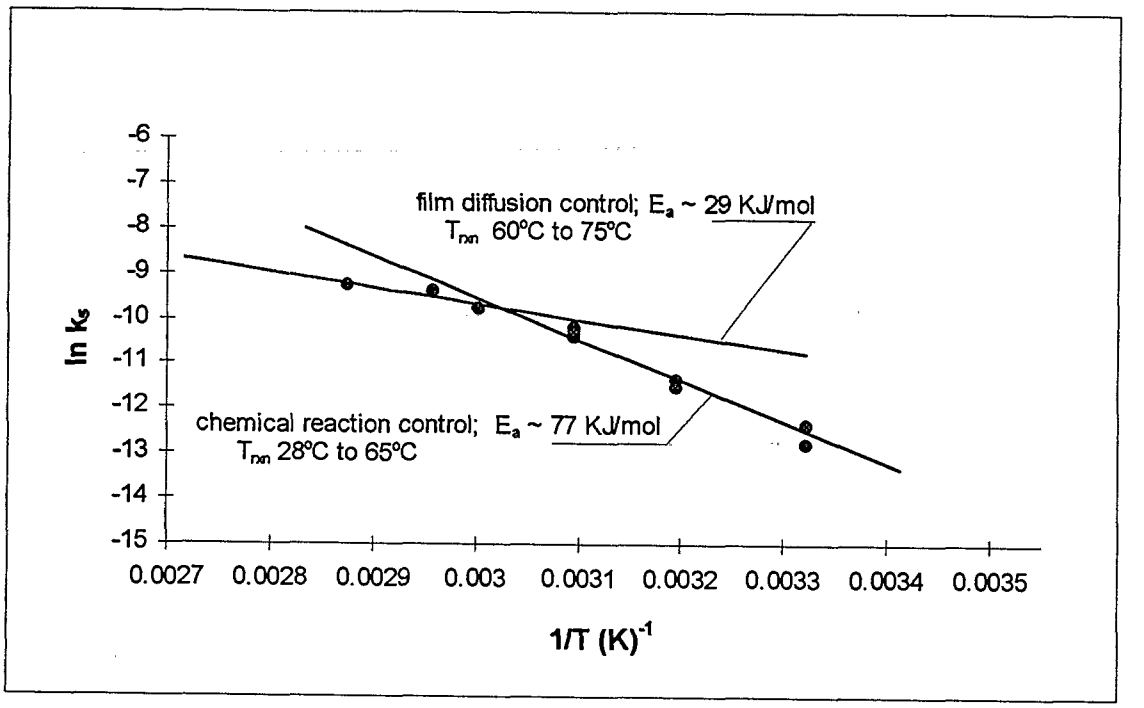

Figure 4.15. Arrhenius data for the dissolution of PuO_2 in the HCl-Fe(II) system containing 7 M HCl and 40 mM Fe(II).

5 CONCLUSIONS AND RECOMMENDATIONS

5.1 Conclusions

As a result of this investigation into the dissolution of PuO_2 in a non-traditional HCl-Fe(II) system, there were several conclusions to be drawn:

1. The dissolution of this low-fired, high-surface area PuO_2 in 7 *M* HCl using 40 *mM* Fe(II) as an electron transfer catalyst at 50°C with agitation at 500 rpm followed the classic nonporous shrinking sphere model under surface chemical reaction control with a conversion-time relationship given by:

$$\frac{t}{\tau_{rxn}} = 1-(1-X)^{1/3} \tag{2.8}$$

2. In addition to the reaction being well described by Eq. 2.8, Arrhenius evaluation of the dissolution reaction between 28°C and 65°C also indicated chemical reaction control due to the magnitude of the activation energy. This value of 76.6±2.2 kJ/mol was well within the surface chemical reaction controlled regime and compared well with the previously reported values of Machuron-Mondard (1990) and Barney (1976) who reported activation energies for PuO_2 to be 65 kJ/mol and 54 kJ/mol, respectively. These values, and the value determined from this work, are much higher than ~40 kJ/mol, reported by Habashi (1969), Terry (1983),

and Machuron-Mondard (1990) as the end of the transition region between diffusion control and surface reaction control as the rate limiting step for this type of reaction.

3. The pre-exponential factor k_o was calculated as $5.95 \cdot 10^7$ cm/sec from Arrhenius intercept data.
4. Due to cohesive interparticle forces, it was not possible to dry-sieve the PuO_2 used in this study and produce sieve fractions with narrow, near mono-size particle size distributions. This conclusion was first noticed when samples of screen fractions were re-analyzed with a LASENTEC LAB-TEC™ 1000 instrument performing transit time measurements based on scanning laser microscopy. The results were later confirmed by dissolution experiments ultimately showing no difference between the kinetic behavior of oxide collected as screen fractions and the unscreened powder assemblage.
5. Because of the kinetic behavior described in Section 4.3, it was concluded that this material behaved as mono-size material. Screening of the assemblage was not necessary to study the fundamental nature of the kinetics governing the dissolution reaction. This was evidenced by the linearity of the assemblage dissolution experiments described in Section 4.0 when examined

with the nonporous shrinking sphere model under chemical reaction control.

6. Cyclic voltammetry as an *in-situ* analytical technique for monitoring these types of heterogeneous chemical reactions was found to generally work quite well. There were electrode cleaning techniques that needed development for the application, but once demonstrated, the cyclic voltammetry was found to be robust and fairly insensitive to either minor temperature or electrode fouling problems. The relative insensitivity of cyclic voltammetry was demonstrated in Table 4.2, where the final calculated rate constants were found to generally be the same regardless of the quality of experimental data used in the calculation.

7. Reduction of the reaction product Fe(III) to a necessary reactant Fe(II), by bulk electrolysis at a platinum mesh cathode was effective for keeping the reagent concentration constant. This allowed the use of small amounts of reagent and simplified the resulting kinetic analysis by eliminating the need to account for changing Fe(II) concentration.

5.2 Recommendations

As a result of this work, the following recommendations for additional study in this area include:

1. Sieving, although it was not necessary for the study of this fine particle system; it would be appropriate to develop a sieving technique to produce narrow distributions of these fine particles for further kinetic studies.
2. Because of the significant deviation of the surface chemical reaction control model at late reaction times toward a film diffusion control model, it would be appropriate to evaluate a mixed reaction–diffusion model for better representing the entire dissolution phenomena throughout the entire reaction time frame.
3. Certainly, a complementary investigation to this work would be a parametric study of the major factors affecting dissolution performance. In this case, a central composite statistical design could be developed to investigate the empirical influence of acid and iron concentration on the dissolution rate, as well as a thorough evaluation of the influence of temperature. The experimental program would require ~20 experiments; eight for the full factorial portion; six axial points; and a minimum of six for the center point replicates. Unfortunately, however, there would only

be three Arrhenius temperatures where acid and iron concentrations were the same (the center points and the two axial temperature points), but the standard error around the center point replicates could be used as an estimate of the standard error of the activation energy.

4. To complete the study of PuO_2 dissolution in the HCl-Fe(II) system, a study of the influence of calcination temperature on the dissolution would definitely be warranted. It is well known that as the calcination temperature increases, the oxide develops a more ordered morphology converting from amorphous to a more regular crystalline structure with a significant reduction in surface area as well. This phenomena has been known to significantly increase the time required for complete dissolution and a thorough evaluation of this effect and methods to overcome its influence is required. It is likely that a statistical approach, similar to Recommendation 2, for studying this effect would be an appropriate start.
5. In conjunction with the previous two Recommendations, alternative reductants for use in hydrochloric acid should be selected and evaluated for use in creating more aggressive conditions for high-fired PuO_2 dissolution.

REFERENCES

Allen, T., 1990. *Particle Size Measurement*, Chapman and Hall, New York.

ATM 1995. "Model L3P Sonic Sifter Operating Manual, " ATM Corporation, Milwaukee, WI.

Baerns, M., 1966. "Effect of Interparticle Adhesive Forces on Fluidization of Fine Particles," *Industrial and Engineering Chemistry Fundamentals*, V5 (4), 508.

Baeyens, J., D. Geldart, and S. Y. Wu, 1992. "Elutriation of Fines from Fluidized Beds of Geldart A-Type Powders – Effect of Adding Super Fines," *Powder Technology*, 71, 71.

Bailey, A. G. 1984. "Electrostatic Phenomena During Powder Handling," *Powder Technology*, 37, 71.

Bard, A. J. and L. R. Faulkner, 1980. *Electrochemical Methods-Fundamentals and Applications*, John Wiley and Sons, New York.

Barney, G. S., 1976. "The Kinetics of Plutonium Oxide Dissolution in Nitric/Hydrofluoric Acid Mixtures," Atlantic Richfield Hanford Company report ARH-SA-255.

Benedict, M., T. H. Pigford, and H. W. Levi, 1981. *Nuclear Chemical Engineering*, second edition, McGraw-Hill.

Benoni, D., C. L. Briens, T. Baron, E. Duchesne, and T. M. Knowlton, 1994. "A Procedure to Determine Particle Agglomeration in a Fluidized Bed and its Effect on Entrainment," *Powder Technology*, 78, 33.

Berger, P., 1990. " A Study of the Dissolution Mechanism by Chemical and Electrochemical Oxidation-Reduction of Actinide Oxides (UO_2, NpO_2, PuO_2, and AmO_2) in an Acid Aqueous Medium," Doctoral Thesis, The University of Paris VI, CEA-R-5575.

Bjorklund, C. W. and E. Staritzky, 1954. "Some Observations on the Reactivity of Plutonium Dioxide," Los Alamos Scientific Laboratory report LA-1869.

Bowling, R. A., 1988. "A Theoretical Review of Particle Adhesion," in *Particles on Surfaces 1–Detection, Adhesion, and Removal*, K. L. Mittal, ed., Plenum Press, NY, 129.

Bray, L. A. and J. L. Ryan, 1982. "Catalyzed Electrolytic Dissolution of Plutonium Dioxide," in *Actinide Recovery from Waste and Low-Grade Sources*, Vol 6, J.D. Navratil and W.W. Schulz, eds., Harwood Academic Publishers, London, 129.

Bray, L. A. and J. L. Ryan, and E. J. Wheelwright, 1986. "Dissolution of Plutonium Dioxide using HCl-HF," Pacific Northwest Laboratory report PNL-6027.

Briens, C. L., M. A. Bergougnou, I. I. Inculet, T. Baron, and J. D. Hazlett, 1992. "Size Distribution of Particles Entrained from Fluidized Beds: Electrostatic Effects," *Powder Technology*, 70, 57.

Bryan, L., Y. Rungvejhavuttivittaya, and P. J. Stewart, 1979. "Mixing and Demixing of Microdose Quantities of Sodium Salicylate in a Direct Compression Vehicle," *Powder Technology*, 22, 147.

Chaouki, J., C. Chavarie, D. Klvana, and G. Pajonk, 1985. "Effect of Interparticle Forces on the Hydrodynamic Behaviour of Fluidized Aerogels," *Powder Technology*, 43, 117

Crossley, D. and G. W. C. Milner, 1969. "The Dissolution of Plutonium Dioxide in Hydrochloric Acid at High Temperature and Pressure," United Kingdom Atomic Energy Authority Research Group report AERE-R 6217.

Dahlby, J. W., R. R. Geoffrion, and G. R. Waterbury, 1975. "The Sealed-Reflux Dissolution System, " Los Alamos Scientific Laboratory report LA-5776.

Derjaguin, B. V., I. N. Aleinikova, and Y. P. Toporov, 1968. "On the Role of Electrostatic Forces in the Adhesion of Polymer Particles to Solid Surfaces," *Powder Technology*, 2, 154.

Egermann, H., 1980. "Effects of Adhesion on Mixing Homogeneity Part 1: Ordered Adhesion – Random Adhesion," *Powder Technology*, 27, 203.

Ellinger, F. H., W. N. Miner, D. R. O'Boyle, and F. Schonfeld. 1968. "Constitution of Plutonium Alloys," Los Alamos Scientific Laboratory report LA-3870.

Fan, L. T. and Y. M. Chen, 1990. "Recent Developments in Solids Mixing," *Powder Technology*, 61, 255.

Fogler, H. S., 1992. *Elements of Chemical Reaction Engineering*, second edition, Prentice-Hall, Englewood Cliffs, New Jersey.

Froment, G. F., and K. B. Bischoff, 1990. *Chemical Reactor Analysis and Design*, second edition, John Wiley and Sons, New York.

Geankoplis, C. J., 1983. *Transport Processes and Unit Operations*, Second Edition, Prentice-Hall, Inc., Englewood Cliffs, New Jersey.

Geldhart, D., N. Harnby, and A. C. Wong, 1984. "Fluidization of Cohesive Powders," *Powder Technology*, 37, 25.

Gilman, W. S., 1965. "A Review of the Dissolution of Plutonium Dioxide," Mound Laboratory report MLM-1264.

Gilman, W. S., 1968. "A Review of the Dissolution of Plutonium Dioxide, Part II," Mound Laboratory report MLM-1513.

Gosser, D. K., 1994. *Cyclic Voltammetry, Simulation and Analysis of Reaction Mechanisms*, VCH Publishers, New York.

Habashi, F., 1969. *Principles of Extractive Metallurgy, Vol. 1, General Principles*, Gordon and Breach Science Publishers, New York.

Harmon, H. D., 1975a. "Dissolution of PuO_2 with Cerium(IV) and Fluoride Promoters," Savannah River Laboratory report DP-1371.

Harmon, H. D., 1975b. "Evaluation of Fluoride, Cerium(IV), and Cerium(IV)-Fluoride Mixtures as Dissolution Promoters for PuO_2 Scrap Recovery Processes," Savannah River Laboratory report DP-1383.

Harris, D. C., 1991. *Quantitative Chemical Analysis*, third edition, W.H. Freeman and Co., New York.

Hershey, J. A. 1975. "Ordered Mixing: A New Concept in Powder Mixing Practice," *Powder Technology*, 11, 41.

Hibbert, D. B., 1993. *Introduction to Electrochemistry*, MacMillan Press, London.

Ibrahim, S. A., E. Hafez, T. H. El-Faham, and F. A. Mohamed, 1989. "Dissolution Enhancement of Thiacetazone: II – Via Ordered Mixing Technique," *Powder Technology*, 58, 107.

Ishida, M. and C. Y. Wen, 1968. "Comparison of Kinetic and Diffusional Models for Solid-Gas Reactions," *AICHE J.* 14 (2), 311.

Ishida, M. and C. Y. Wen, 1971. "Comparison of Zone-Reaction and Unreacted-Core-Shrinking Model in Solid-Gas Reactions–I Isothermal Analysis," *Chemical Engineering Science*, V26, 1031.

Jaraiz, E., S. Kimura, and O. Levenspiel, 1992. "Vibrating Beds of Fine Powders: Estimation of Interparticle Forces From Expansion and Pressure Drop Experiments," *Powder Technology*, 72, 23.

Karuhn, R. F., Particle Technology Laboratories, Westmont, IL, 1996. *Personal Communication.*

Katz, J. J., G. T. Seaborg, and L. R. Morss, 1986. *The Chemistry of the Actinide Elements*, second edition, V.1, Chapman and Hall.

Kono, H. O., C. C. Huang, E. Morimoto, T. Nakayama, and T. Hikosaka, 1987. "Segregation and Agglomeration of Type C Powders from Homogeneously Aerated Type A-C Powder Mixtures During Fluidization," *Powder Technology*, 53, 163.

Lai, F., J. A. Hershey, and J. N. Staniforth, 1981. "Segregation and Mixing of Fine Particles in an Ordered Mixture," *Powder Technology*, 28, 17.

Lam, K. K., and J. M. Newton, 1992. "Influence of Particle Size on the Adhesion Behavior of Powders after Application of an Initial Press-On Force," *Powder Technology*, 73, 117.

LASENTEC, 1992." LAB-TEC™ 1000 Users Manual," LASENTEC, Redmond, WA.

Levenspiel, O., 1972. *Chemical Reaction Engineering*, second edition, John Wiley and Sons, New York.

Li, H., H. Legas, C. M. H. Brereton, J. R. Grace, and J. Chaouki, 1990. "Hydrodynamic Behavior of Aerogel Powders in High Velocity Fluidized Beds," *Powder Technology*, 60, 121.

Machuron-Mandard, X., 1991. "Study of the Kinetics and the Mechanism of the Dissolution Reaction of Plutonium Dioxide by the Cr(II) ion in Acid Solution," Doctoral Thesis, University of Paris VI, CEA-R-5579.

Madic, C., P. Berger, and X. Machuron-Mandard, 1992. "Mechanisms of the Rapid Dissolution of Plutonium Dioxide in Acidic Media under Oxidizing and Reducing Conditions," *Transuranium Elements - A Half Century*, L. R. Morss and J. Fuger, eds., Symposium Proceedings, 200th ACS National Meeting, Washington, D. C., 457.

Mantz, K. W., J. K. Beddow, and P. B. Butler, 1988."Adhesion and Removal of Particulate Contaminants in a High Decibel Acoustic Field," *Powder Technology*, 55, 133.

Mason, R. L., R. f. Gunst, and J. L. Hess, 1989. *Statistical Design and Analysis of Experiments–with Applications to Engineering and Science*, John Wiley and Sons, New York.

Molen, G. F., 1967. "Dissolution of Plutonium Oxide," The Dow Chemical Company, Rocky Flats Division report RFP-922.

Naito, K., T. Tsuji, T. Matsui, T. Fujino, T. Yamashita, and K. Ohuchi, 1992. "Defect Chemistry of Plutonium Oxides," *Transuranium Elements - A Half Century*, L. R. Morss and J. Fuger, eds., Symposium Proceedings , 200th ACS National Meeting, Washington, D. C., 440.

Nathier-Defour, N., L. Bougeard, M. F. Devaux, D. Bertrand, and F. Le Deschault de Monredon, 1993. "Comparison of Sieving and Laser Diffraction for the Particle Size Measurements of Raw Materials Used in Foodstuff," *Powder Technology*, 76, 191.

Nushart, S. E., ATM Corporation, Milwaukee, WI, 1996. *Personal Communication.*

Park, J. Y. and O. Levenspiel, 1975. "The Crackling Core Model for the Reaction of Solid Particles," *Chemical Engineering Science*, V30, 1207.

Parker, H. W. and W. F. Stevens, 1959. "Effect of Liquid on Interparticle Forces in Gas-Fluidized Beds," *AIChEJ.*, V5 (3), 314.

Petersen, R. G., 1985. *Design and Analysis of Experiments*, Mercel Dekker, New York.

Peterson, E. E., 1957. "Reaction of Porous Solids," *AICHE J.*, V3 (4), 443.

Ranade, M. B., V. B. Menon, M. E. Mullins, and V. L. Debler, 1988. "Adhesion and Removal of Particles: Effect of Medium," in *Particles on Surfaces 1 - Detection, Adhesion, and Removal*, K. L. Mittal, ed., Plenum Press, NY, 179.

Ranz, W. E. and W. R. Marshall, 1952. "Evaporation from Drops – Part II," *Chem. Engr. Prog.*, V48 (4), 173.

Rees, J. E. and J. N. Staniforth, 1979. "Characterization of Ordered Mixes Using X-Ray Microanalysis," *Powder Technology*, 23, 135.

Rumpf, H., 1962. "The Strength of Granules and Agglomerates," in *Agglomeration*, W. A. Knepper (ed), Interscience Publishers, 379.

Ryan, J. L. and L. A. Bray, 1980. "Dissolution of Plutonium Dioxide - A Critical Review," *Actinide Separations*, J.D. Navratil and W.W. Schultz eds., ACS Symposium Series, 177th ACS National Meeting, Honolulu, HI, 499.

Ryan, J. L., L. A. Bray, E. J. Wheelwright, and G. H. Bryan, 1992. "Catalyzed Electrolytic Plutonium Oxide Dissolution - The Past Seventeen Years and Future Potential," *Transuranium Elements - a Half Century*, L.R. Morss and J, Fuger eds., ACS Symposium Series, 200th ACS National Meeting, Washington, D.C., 289.

Shakila, A. M., T. G. Srinivasan, and K. N. Sabharwal, and P. R. V. Rao, 1987. "Dissolution of PuO_2 in HNO_3-HF-N_2H_4 Medium," *Nuclear Technology*, 79, 116.

Shakila, A. M., T. G. Srinivasan, and K. N. Sabharwal, 1989. "Dissolution of PuO_2 in Hydrochloric Acid - Effect of Reducing Agents," *Nuclear Technology*, 88, 290.

Shying, M. E., T. M. Florence, and D. J. Carswell, 1970. "Oxide Dissolution Mechanisms - I; The Role of Fluoride in the Thoria/Nitric/Hydrofluoric Acid System," *J. Inorg. Nucl. Chem.*, 32, 3493.

Shying, M. E., T. M. Florence, and D. J. Carswell, 1972. "Oxide Dissolution Mechanisms – II; A Mechanism for the Thoria/Nitric/Hydrofluoric Acid System," *J. Inorg. Nucl. Chem.*, 34, 213.

Smith, J. M., 1970. *Chemical Engineering Kinetics*, second edition, McGraw-Hill, New York.

Sohn, H. Y., 1976. "Kinetics of Non-Catalytic Fluid-Solid Reactions in Chemical and Extractive Metallurgical Processes: Part II, Reaction of a Single Porous Particle," *Hwahak Konghak*, V14 (2), 65.

Sohn, H. Y. and M. E. Wadsworth, 1979. *Rate Processes of Extractive Metallurgy*, Plenum Press, New York.

Suhm, H. O., 1969. "Oscillating Air Column for the Dry Separation of Fine and Subsieve Particle Sizes," *Powder Technology*, 2, 356.

Szekely, J., J. W. Evans, and H. Y. Sohn, 1976. *Gas-Solid Reactions*, Academic Press, New York.

Takeuchi, T., C. K. Hanson, and M. E. Wadsworth, 1971. "Kinetics and Mechanism of the Dissolution of Thorium Oxide in Hydrofluoric Acid and Nitric Acid Mixtures," *J. Inorg. Nucl. Chem.*, 34, 213.

Tallent, O. K. and J. C. Mailen, 1977a. "Study of the Dissolution of Refractory PuO_2 in Nitric-Hydrofluoric Acid Dissolvents at 100°C," *Nucl. Technol.*, 32, 167.

Tallent, O. K. and J. C. Mailen, 1977b. "Effects of Metal Ion Impurities on PuO_2 Dissolution in Nitric-Hydrofluoric Acid Solution" *Nucl. Technol.*, 34, 416.

Terry, B., 1983. "Specific Chemical Rate Constants for the Acid Dissolution of Oxides and Silicates," *Hydrometallurgy*, 11, 315.

Thoma, S. G., M. Ciftcioglu, and D. M. Smith, 1991. "Determination of Agglomerate Strength Distributions. Part 1: Calibration via Ultrasonic Forces," *Powder Technology*, 68, 53.

Uriarte, A. L. and R. H. Rainey, 1965. "Dissolution of High-Density UO_2, PuO_2, and UO_2-PuO_2 Pellets in Inorganic Acids," Oak Ridge National Laboratory report ORNL-3695.

Visser, J., 1989. "Invited Review: Van der Waals and other Cohesive Forces Affecting Powder Fluidization," *Powder Technology*, 58, 1.

Wen, C. Y., 1968. "Noncatalytic Heterogeneous Solid Fluid Reaction Models," *Industrial and Engineering Chemistry*, V60 (9), 34.

Williams, J. C., 1968. "The Mixing of Dry Powders," *Powder Technology*, 2, 13.

Wilson, A. S., 1961. U. S. Patent 3005682.

Yip, C. W., and J. A. Hershey, 1977a. "Segregation in Ordered Powder Mixtures," *Powder Technology*, 16, 149.

Yip, C. W., and J. A. Hershey, 1977b. "Perfect Powder Mixtures," *Powder Technology*, 16, 189.

Zawodzinski, C., W. H. Smith, and K. R. Martinez, 1993. "Kinetic Studies of the Electrochemical Generation of Ag(II) Ion and the Catalytic Oxidization of Selected Organics," Proceedings of the Symposium on Environmental Aspects of Electrochemistry and Photoelectrochemistry, V93 (18), *Electrochemical Society*, 170.

Zawodzinski, C., 1996. 'Mediated Electrochemical Oxidation of Isopropanol," Doctoral dissertation, The University of New Mexico, in preparation.

APPENDIX: EXPERIMENTAL DATA

The data in this Appendix summarize experiments from the entire experimental program described in this report. In addition to data at 50°C, seven additional experiments used in the Arrhenius evaluation of the activation energy of the chemical reaction are included, as well as two experiments where the acid concentration was low, as determined by titration. The disposition of individual experiments is also briefly discussed, as well as a description of any problem causing the experiment to be rejected from further analysis. This subset of rejected experiments comprise the difference in the data presented in Figures 4.11 and 4.12 in the body of the text.

February 1, 1994: This early assemblage experiment was used only in the Arrhenius evaluation of the reaction activation energy. The slope of the plot of the surface chemical reaction controlled model ($1-(1-X)^{1/3}$ vs. t) was determined to be 0.00154 min^{-1} with a linear correlation coefficient of 0.978. In attempting to determine the best fit linearized form of the three nonporous shrinking sphere models, the last two points were omitted from this data set (these regression data were not presented in Table 4.2).

Table A-1: Experimental Data for February 1, 1994; Arrhenius Data at 40°C.

Time (min)	Extent of Reaction	Total Coulombs	Temperature (°C)
0	0	0	43
30	0.069	50	39
54	0.271	100	43
83	0.414	150	43
128	0.506	200	40
203	0.663	265	39
248	0.746	300	38
314	0.920	350	41
395	1.000	393	41

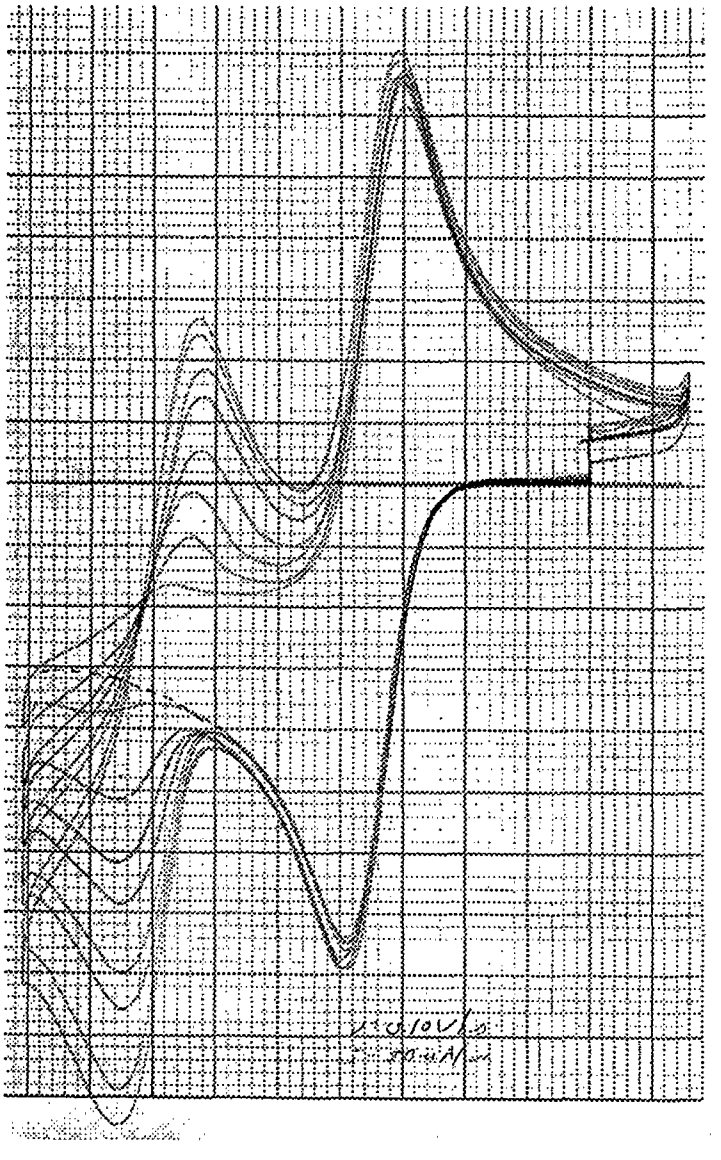

February 1, 1994
1.000 gram PuO_2 assemblage
0.8005 g $FeCl_3$-$6H_2O$ = 40 *mM* Fe
75 ml of 7 *M* HCl in agitated cell
standard calomel reference electrode
platinum working electrode
X = 200 mV/in
Y = 0.05 mA/in
rest potential = -0.1 V
scanned potential range = -0.27 V to +0.95 V
scan rate = 100 mV/sec
agitation = 600 rpm
temperature = 40°C

Figure A-1: Experimental data for February 1, 1994; Arrhenius data at 40°C.

February 14, 1994: This early assemblage experiment was used only in the Arrhenius evaluation of the reaction activation energy. The slope of the plot of the surface chemical reaction controlled model was determined to be 0.000379 min^{-1} with a linear correlation coefficient of 0.987. In attempting to determine the best fit linearized form of the three nonporous shrinking sphere models, the last point was omitted from this data set (these regression data were not presented in Table 4.2).

The scale notation on the potential axis is incorrect, see the figure legend for the correct potential scan range.

Table A-2: Experimental Data for February 14, 1994; Arrhenius Data at 28°C.

Time (min)	Extent of Reaction	Total Coulombs	Temperature (°C)
0	0	0	27
60	0.064	37	28
120	0.110	61	28
307	0.342	128	28
496	0.477	182	28
1356	0.845	375	28
1550	0.948	399	28
1790	1.000	424	28

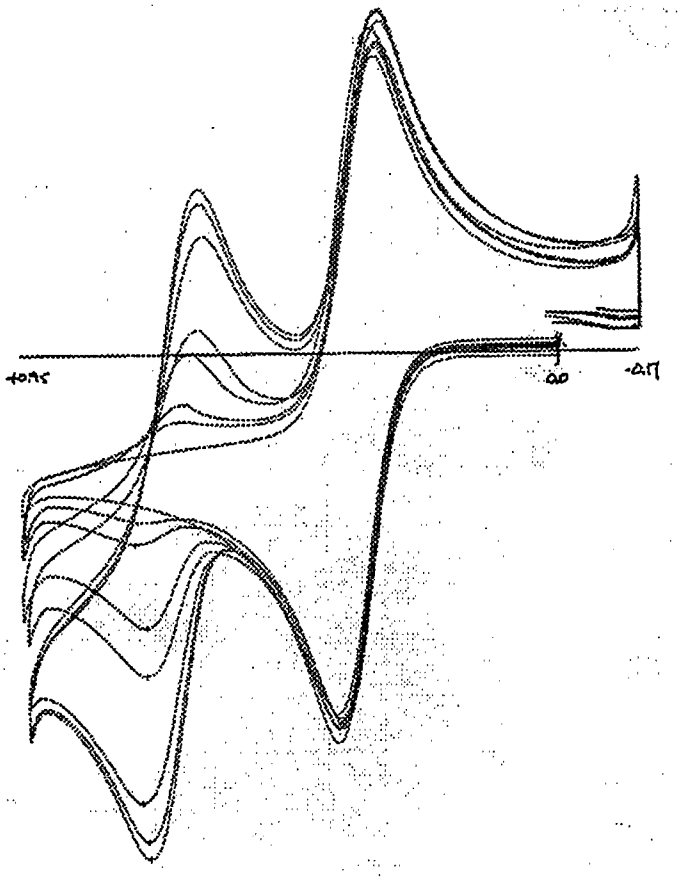

February 14, 1994
1.000 gram PuO_2 assemblage
0.8005 g $FeCl_3$-$6H_2O$ = 40 *mM* Fe
75 ml of 7 *M* HCl in agitated cell
standard calomel reference electrode
platinum working electrode
X = 200 mV/in
Y = 0.05 mA/in
rest potential = -0.1 V
scanned potential range = -0.27 V to +0.95 V
scan rate = 100 mV/sec
agitation = 600 rpm
temperature = ambient = 28°C

Figure A-2: Experimental data for February 14, 1994; Arrhenius data at 28°C.

February 28, 1994: This early assemblage experiment was used only in the Arrhenius evaluation of the reaction activation energy. The slope of the plot of the surface chemical reaction controlled model was determined to be 0.000558 min^{-1} with a linear correlation coefficient of 0.998. In attempting to determine the best fit linearized form of the three nonporous shrinking sphere models, the last point was omitted from this data set (these regression data were not presented in Table 4.2).

The scale notation on the potential axis is incorrect, see the figure legend for the correct potential scan range.

Table A-3: Experimental Data for February 28, 1994; Arrhenius Data at 28°C.

Time (min)	Extent of Reaction	Total Coulombs	Temperature (°C)
0	0	0	27
86	0.145	61	28
232	0.319	122	29
318	0.404	153	29
1263	0.976	382	28
1506	1.000	406	28

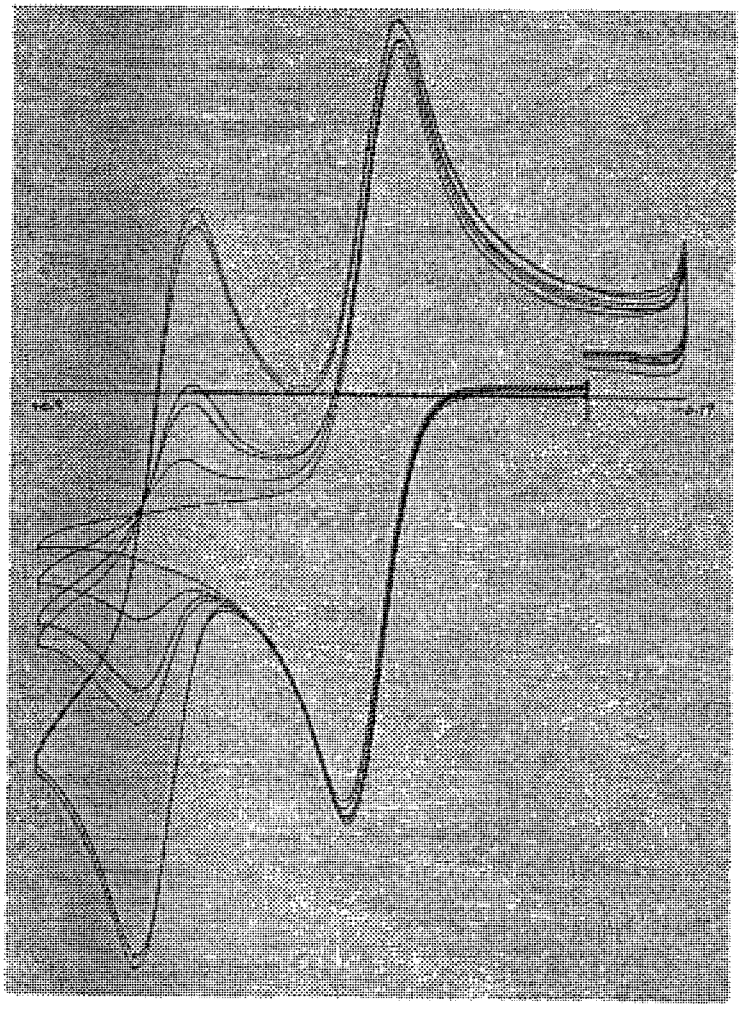

February 28, 1994
1.000 gram PuO_2 assemblage
0.8005 g $FeCl_3$-$6H_2O$ = 40 *mM* Fe
75 ml of 7 *M* HCl in agitated cell
standard calomel reference electrode
platinum working electrode
X = 200 mV/in
Y = 0.05 mA/in
rest potential = -0.1 V
scanned potential range = -0.27 V to +0.95 V
scan rate = 100 mV/sec
agitation = 600 rpm
temperature = ambient = 28°C

Figure A-3: Experimental data for February 28, 1994; Arrhenius data at 28°C.

March 14, 1994: This early assemblage experiment was used only in the Arrhenius evaluation of the reaction activation energy. The slope of the plot of the surface chemical reaction controlled model was determined to be 0.00131 min^{-1} with a linear correlation coefficient of 0.972. In attempting to determine the best fit linearized form of the three nonporous shrinking sphere models, the last point was omitted from this data set (these regression data were not presented in Table 4.2).

The scale notation on the potential axis is incorrect, see the figure legend for the correct potential scan range.

Table A-4: Experimental Data for March 14, 1994; Arrhenius Data at 40°C.

Time (min)	Extent of Reaction	Total Coulombs	Temperature (°C)
0	0	0	38
36	0.060	50	37
82	0.248	100	39
170	0.456	175	40
285	0.718	268	40
350	0.879	314	40
482	1.000	372	39

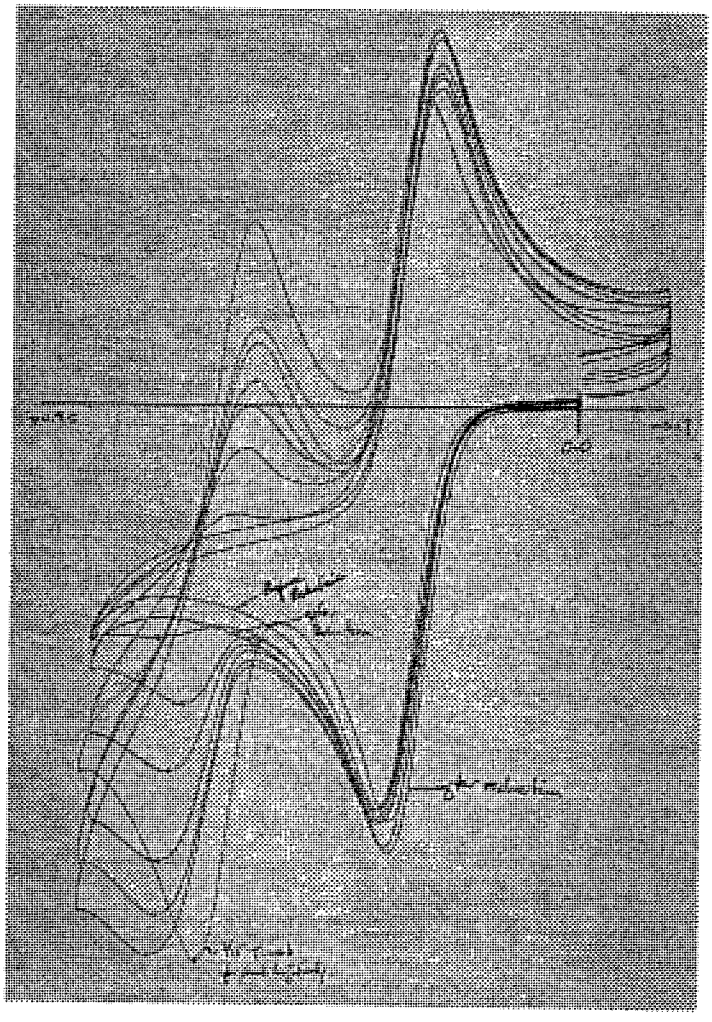

March 14, 1994
1.000 gram PuO_2 assemblage
0.8005 g $FeCl_3$-$6H_2O$ = 40 *mM* Fe
75 ml of 7 *M* HCl in agitated cell
standard calomel reference electrode
platinum working electrode
X = 200 mV/in
Y = 0.05 mA/in
rest potential = -0.1 V
scanned potential range = -0.27 V to +0.95 V
scan rate = 100 mV/sec
agitation = 600 rpm
temperature = 40°C

Figure A-4: Experimental data for March 14, 1994; Arrhenius data at 40°C.

November 17, 1995: This assemblage experiment marks the first scoping run of the series of experiments at 50°C. The data were rejected because of a lack of sufficient data, however, the experiment produced a slope for the surface chemical reaction controlled model of 0.00404 min^{-1}, having a linear correlation coefficient of 0.996. In attempting to determine the best fit linearized form of the three nonporous shrinking sphere models, the last point was omitted from this data set (see the regression coefficient data presented in Table 4.2).

Table A-5: Experimental Data for November 17, 1995.

Time (min)	Extent of Reaction	Temperature (°C)
0	0	49
30	0.318	50
45	0.449	52
60	0.551	50
255	1.000	50

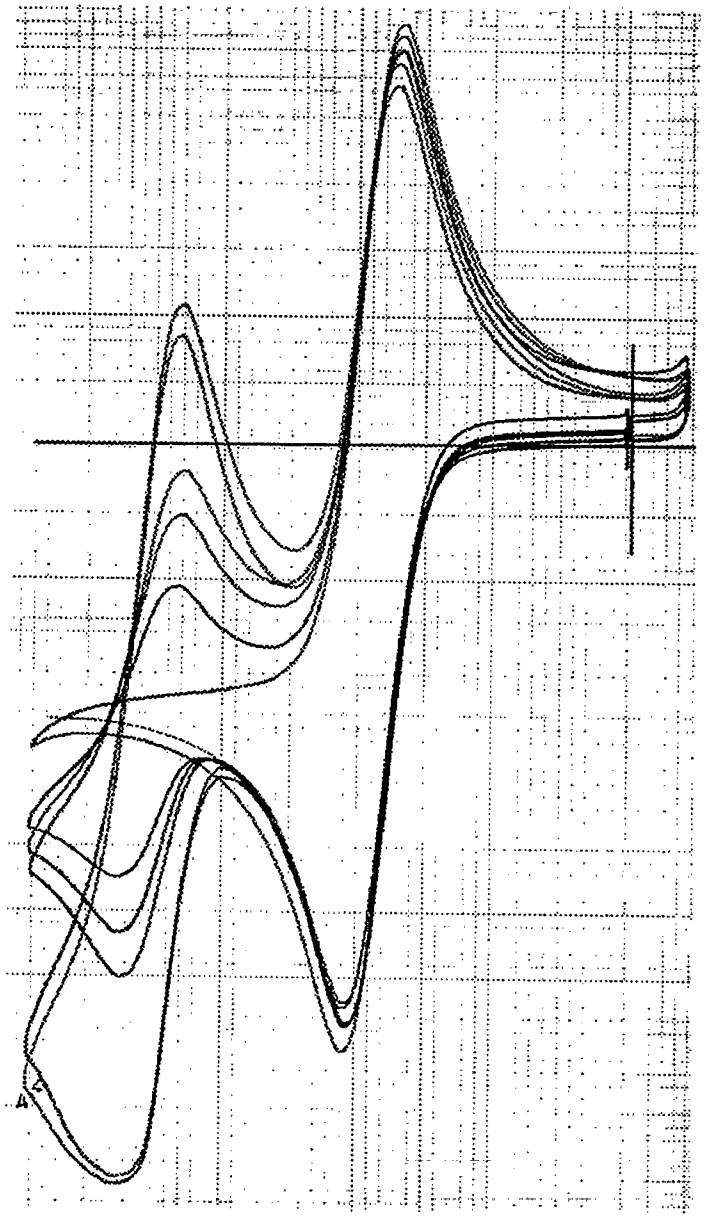

November 17, 1995
1.000 gram PuO_2 assemblage
0.5964 g $FeCl_2$-$4H_2O$ = 40 *mM* Fe
75 ml of 7 *M* HCl in agitated cell
double junction reference electrode
platinum working electrode
X = 200 mV/in
Y = 0.05 mA/in
rest potential = -0.1 V
scanned potential range = -0.2 V to +0.8 V
scan rate = 100 mV/sec
agitation = 500 rpm
temperature = 50°C

Figure A-5: Experimental Data for November 17, 1995.

November 20, 1995: The data for this assemblage experiment were rejected from further analysis due to inadequate temperature control and degradation of working electrode at the end of the experiment, however, the experiment produced a slope for the surface chemical reaction controlled model of 0.00476 min^{-1}, having a linear correlation coefficient of 0.990. In attempting to determine the best fit linearized form of the three nonporous shrinking sphere models, the last point was omitted from this data set (see the regression coefficient data presented in Table 4.2).

Table A-6: Experimental Data for November 20, 1995.

Time (min)	Extent of Reaction	Total Coulombs	Temperature (°C)
0	0	0	51
15	0.191	56	51.8
32	0.330	106	50.4
47	0.457	144	50.2
63	0.574	177	50
83.4	0.713	217	50
100	0.819	246	49.8
125	0.926	285	49.2
180	1.000	347	50

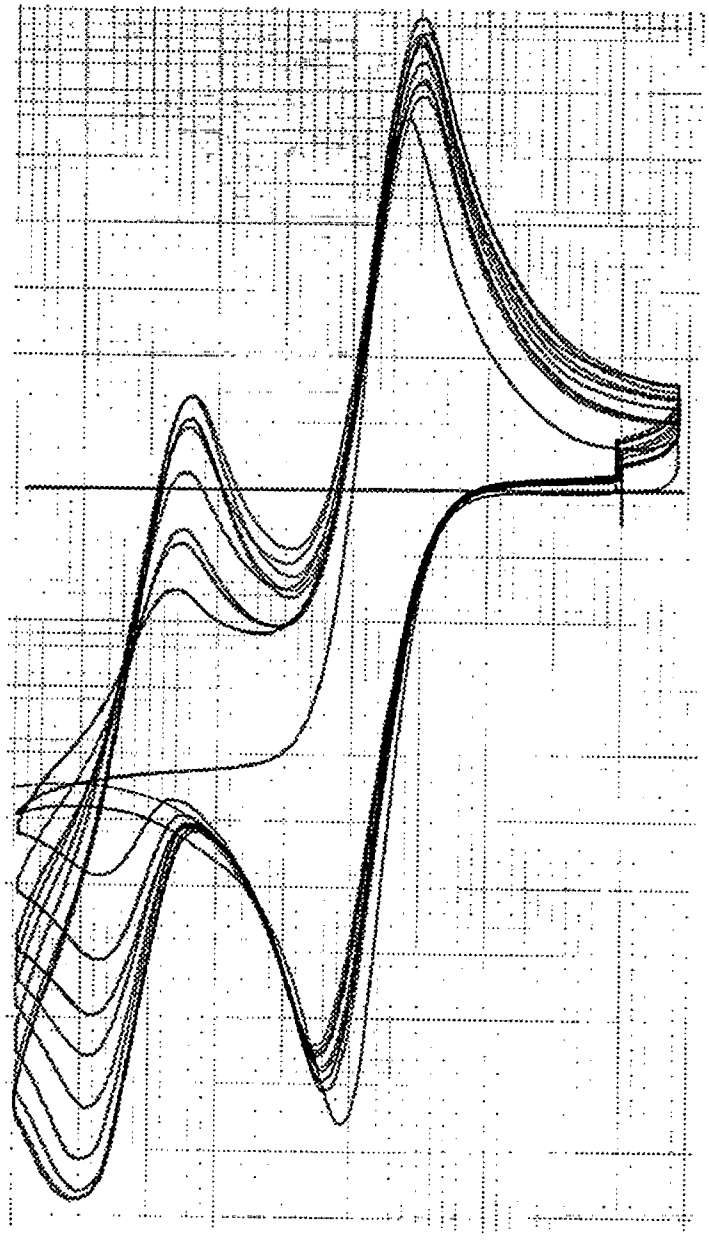

November 20, 1995
1.000 gram PuO_2 assemblage
0.5964 g $FeCl_2$-$4H_2O$ = 40 *mM* Fe
75 ml of 7 *M* HCl in agitated cell
double junction reference electrode
platinum working electrode
X = 200 mV/in
Y = 0.05 mA/in
rest potential = -0.1 V
scanned potential range = -0.2 V to +0.8 V
scan rate = 100 mV/sec
agitation = 500 rpm
temperature = 50°C

Figure A-6: Experimental Data for November 20, 1995.

November 21, 1995: The data for this assemblage experiment were rejected from further analysis due to inadequate temperature control, however, the experiment produced a slope for the surface chemical reaction controlled model of 0.00562 min^{-1}, having a linear correlation coefficient of 0.995. In attempting to determine the best fit linearized form of the three nonporous shrinking sphere models, the last point was omitted from this data set (see the regression coefficient data presented in Table 4.2).

With this experiment, there was a change in the magnetic stirrer from a Nalgene Starhead™ 22 mm magnetic stirbar (Nalge Co., a subsidiary of Sybron Corp., Rochester, NY part number 6600-0022), to the VWR Starburst™ magnetic stirbar described in section 3.2.1.

Table A-7: Experimental Data for November 21, 1995.

Time (min)	Extent of Reaction	Total Coulombs	Temperature (°C)
0	0	0	49.5
15	0.237	68	52.5
30	0.408	128	50.8
45	0.534	170	50.2
62	0.684	209	49.9
80	0.822	246	50.1
96	0.901	277	49.9
165	1.000	360	50

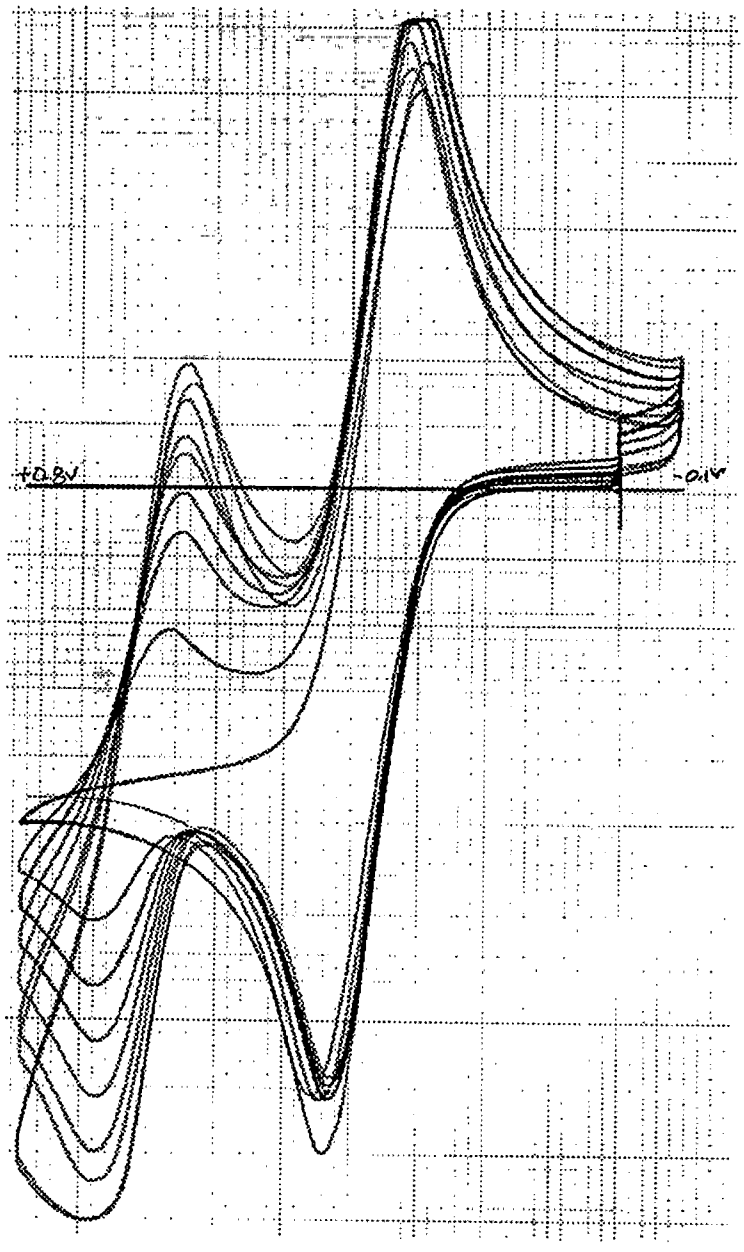

November 21, 1995
1.000 gram PuO_2 assemblage
0.5964 g $FeCl_2$-$4H_2O$ = 40 *mM* Fe
75 ml of 7 *M* HCl in agitated cell
double junction reference electrode
platinum working electrode
X = 200 mV/in
Y = 0.05 mA/in
rest potential = -0.1 V
scanned potential range = -0.2 V to +0.8 V
scan rate = 100 mV/sec
agitation = 500 rpm with new magnetic stirrer design
temperature = 50°C

Figure A-7: Experimental Data for November 21, 1995.

November 29, 1995: This assemblage experiment produced a slope for the surface chemical reaction controlled model of 0.00465 min^{-1}, having a linear correlation coefficient of 0.990. In attempting to determine the best fit linearized form of the three nonporous shrinking sphere models, the last two points were omitted from this data set (see the regression coefficient data presented in Table 4.2).

Table A-8: Experimental Data for November 29, 1995.

Time (min)	Extent of Reaction	Total Coulombs	Temperature (°C)
0	0	0	50.2
15	0.214	55	50.5
35	0.421	111	50
53	0.553	153	50
71	0.654	189	50
87	0.780	219	50
111	0.906	261	50
124	0.981	280	50
146	1.000	301	50.2

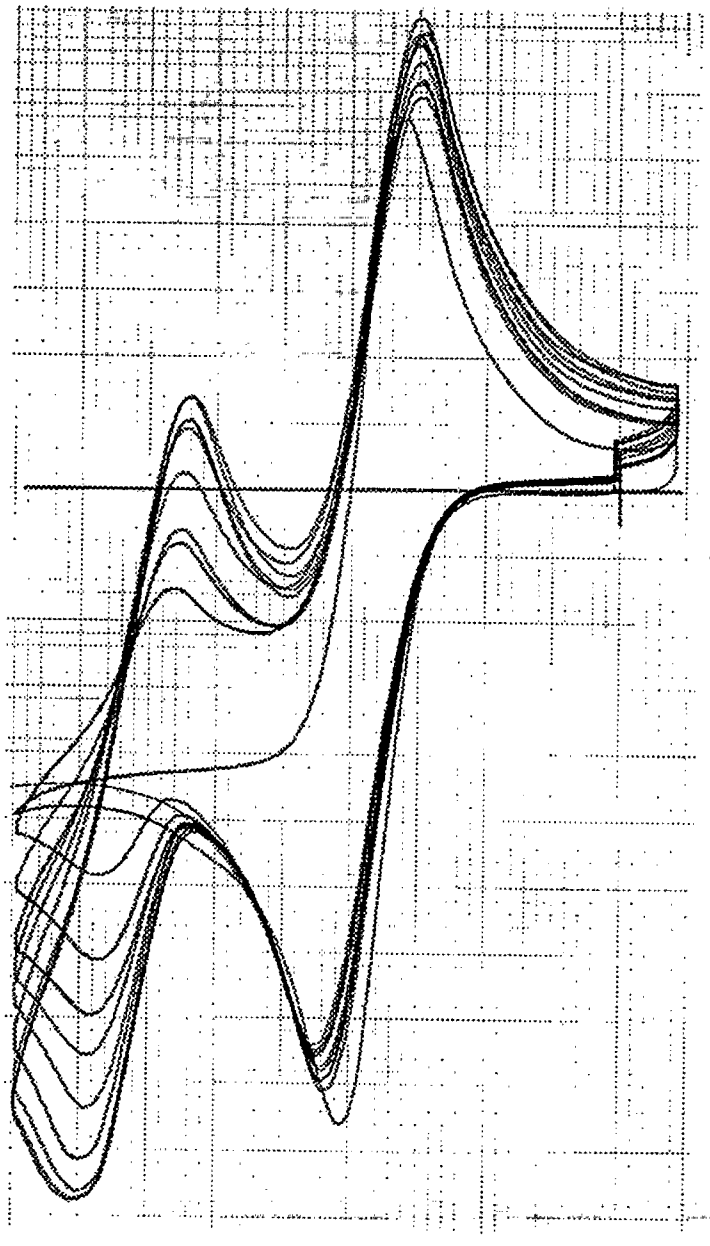

November 29, 1995
1.000 gram PuO_2 assemblage
0.5964 g $FeCl_2$-$4H_2O$ = 40 *mM* Fe
75 ml of 7 *M* HCl in agitated cell
double junction reference electrode
platinum working electrode
X = 200 mV/in
Y = 0.05 mA/in
rest potential = -0.1 V
scanned potential range = -0.2 V to +0.8 V
scan rate = 100 mV/sec
agitation = 500 rpm
temperature = 50°C

Figure A-8: Experimental Data for November 29, 1995.

November 30, 1995: The data for this assemblage experiment were rejected from further analysis due to inadequate temperature control, working electrode, and reference electrode problems, however, the experiment produced a slope for the surface chemical reaction controlled model of 0.00426 min^{-1}, having a linear correlation coefficient of 0.950. In attempting to determine the best fit linearized form of the three nonporous shrinking sphere models, the last two points were omitted from this data set (see the regression coefficient data presented in Table 4.2).

Table A-9: Experimental Data for November 30, 1995.

Time (min)	Extent of Reaction	Total Coulombs	Temperature (°C)
0	0	0	49.8
10	0.142	36	50
20	0.243	68	50.2
35	0.373	110	49
50	0.479	141	48
65	0.538	170	50
80	0.657	201	50
105	0.888	234	50
124	0.964	267	50
154	1.000	312	50

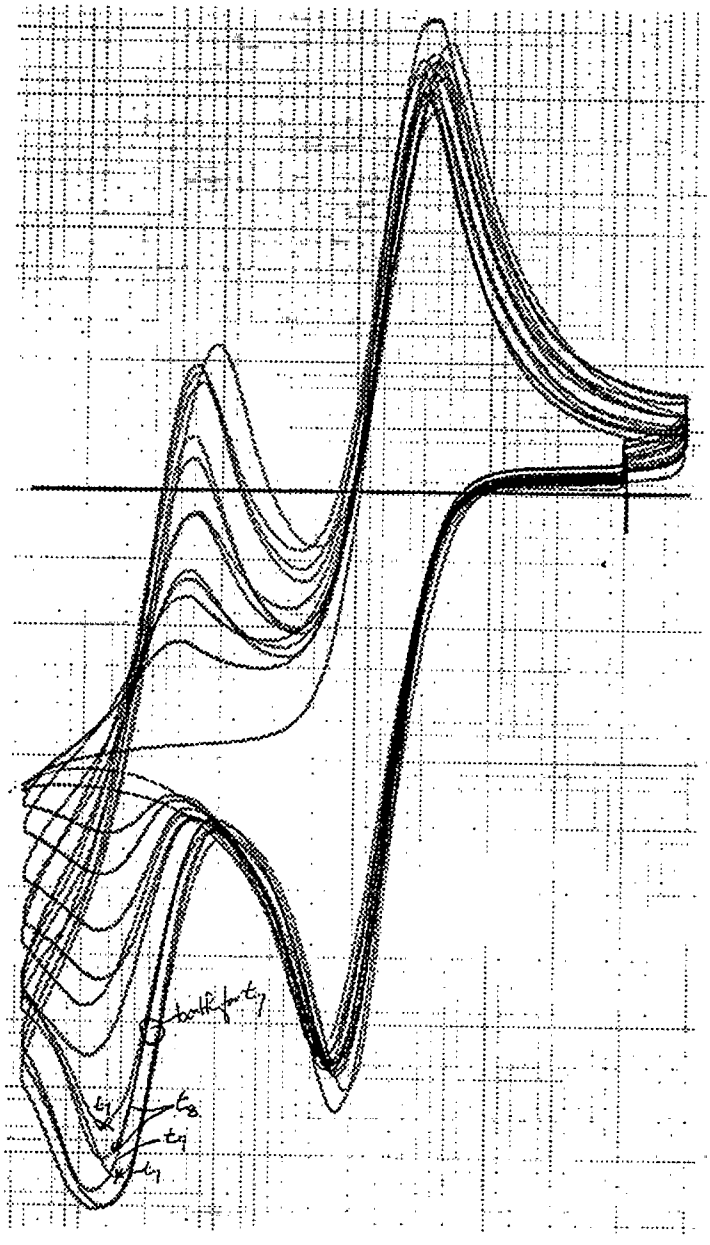

November 30, 1995
1.000 gram PuO_2 assemblage
0.5964 g $FeCl_2$-$4H_2O$ = 40 *mM* Fe
75 ml of 7 *M* HCl in agitated cell
double junction reference electrode
platinum working electrode
X = 200 mV/in
Y = 0.05 mA/in
rest potential = -0.1 V
scanned potential range = -0.2 V to +0.8 V
scan rate = 100 mV/sec
agitation = 500 rpm
temperature = 50°C

Figure A-9: Experimental data for November 30, 1995.

December 1, 1995: The data for this assemblage experiment were rejected from further analysis due to working electrode problems, however, the experiment produced a slope for the surface chemical reaction controlled model of 0.00538 min^{-1}, having a linear correlation coefficient of 0.986. In attempting to determine the best fit linearized form of the three nonporous shrinking sphere models, the last point was omitted from this data set (see the regression coefficient data presented in Table 4.2).

Table A-10: Experimental Data for December 1, 1995.

Time (min)	Extent of Reaction	Total Coulombs	Temperature (°C)
0	0	0	50
16	0.343	66	50.2
24	0.361	106	51
35	0.464	130	50.5
45	0.578	151	50
55	0.651	173	50
65	0.711	220	50
87	0.868	248	50.2
107	0.910	273	50
125	1.000	307	50.5

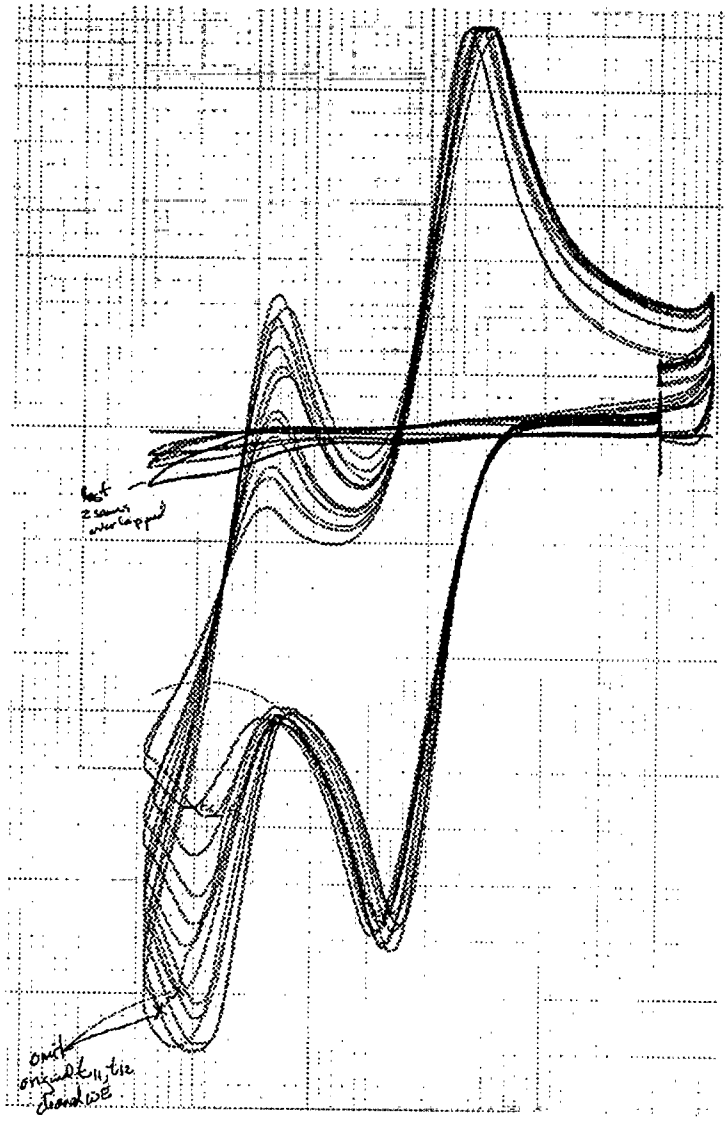

December 1, 1995
1.000 gram PuO_2 assemblage
0.5964 g $FeCl_2$-$4H_2O$ = 40 *mM* Fe
75 ml of 7 *M* HCl in agitated cell
double junction reference electrode
platinum working electrode
X = 200 mV/in
Y = 0.05 mA/in
rest potential = -0.1 V
scanned potential range = -0.2 V to +0.8 V
scan rate = 100 mV/sec
agitation = 500 rpm
temperature = 50°C

Figure A-10: Experimental data for December 1, 1995.

December 12, 1995: The data for this assemblage experiment produced a slope for the surface chemical reaction controlled model of 0.00504 min^{-1}, having a linear correlation coefficient of 0.988. In attempting to determine the best fit linearized form of the three nonporous shrinking sphere models, the last point was omitted from this data set (see the regression coefficient data presented in Table 4.2).

Table A-11: Experimental Data for December 12, 1995.

Time (min)	Extent of Reaction	Total Coulombs	Temperature (°C)
0	0	0	50.3
15	0.242	53	50.5
26	0.371	99	50.3
36	0.470	130	51
48	0.561	162	50.2
58	0.623	187	50.5
68	0.697	208	51
78	0.742	226	50
93	0.818	257	50
103	0.879	273	50
113	0.932	290	50.3
123	0.962	302	50
143	1.000	332	50

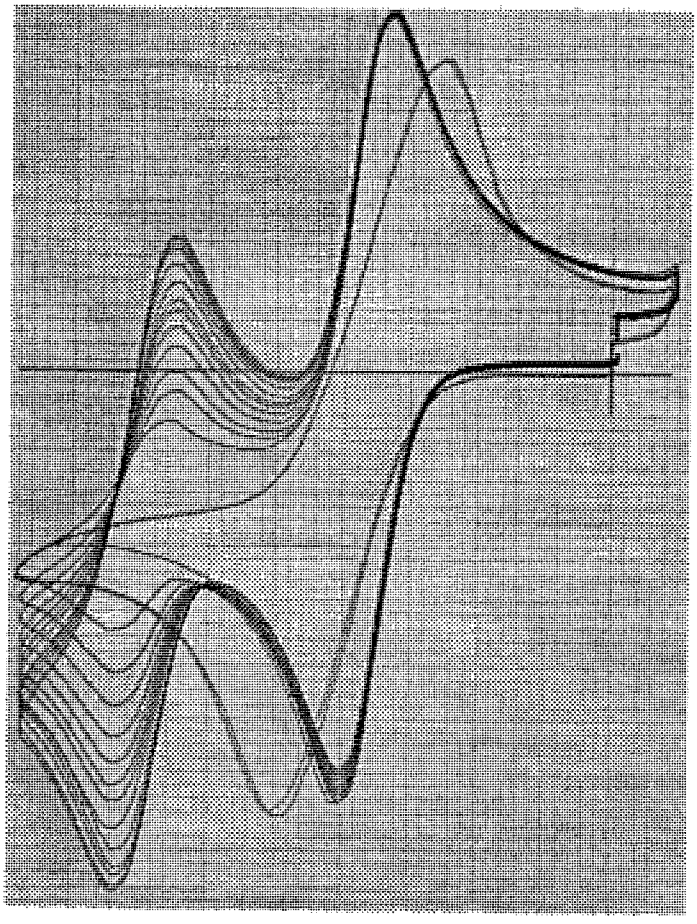

December 12, 1995
1.000 gram PuO_2 assemblage
0.5964 g $FeCl_2$-$4H_2O$ = 40 *mM* Fe
75 ml of 7 *M* HCl in agitated cell
double junction reference electrode
platinum working electrode
X = 200 mV/in
Y = 0.1 mA/in
rest potential = -0.1 V
scanned potential range = -0.2 V to +0.8 V
scan rate = 200 mV/sec
agitation = 500 rpm
temperature = 50°C

Figure A-11: Experimental data for December 12, 1995.

December 13, 1995 am: The data for this assemblage experiment produced a slope for the surface chemical reaction controlled model of 0.00418 min^{-1}, having a linear correlation coefficient of 0.999. In attempting to determine the best fit linearized form of the three nonporous shrinking sphere models, the last point was omitted from this data set (see the regression coefficient data presented in Table 4.2).

Table A-12: Experimental Data for December 13, 1995 am.

Time (min)	Extent of Reaction	Total Coulombs	Temperature (°C)
0	0	0	49.7
10	0.135	39	49.7
20	0.257	78	50
30	0.351	111	50.2
40	0.439	140	50
50	0.514	164	50.2
60	0.574	187	50
70	0.642	210	50
80	0.710	231	50
95	0.777	258	50
105	0.824	276	50
115	0.865	293	50
125	0.892	307	50
135	0.912	322	50
146	0.939	334	50
172	1.000	356	49.7

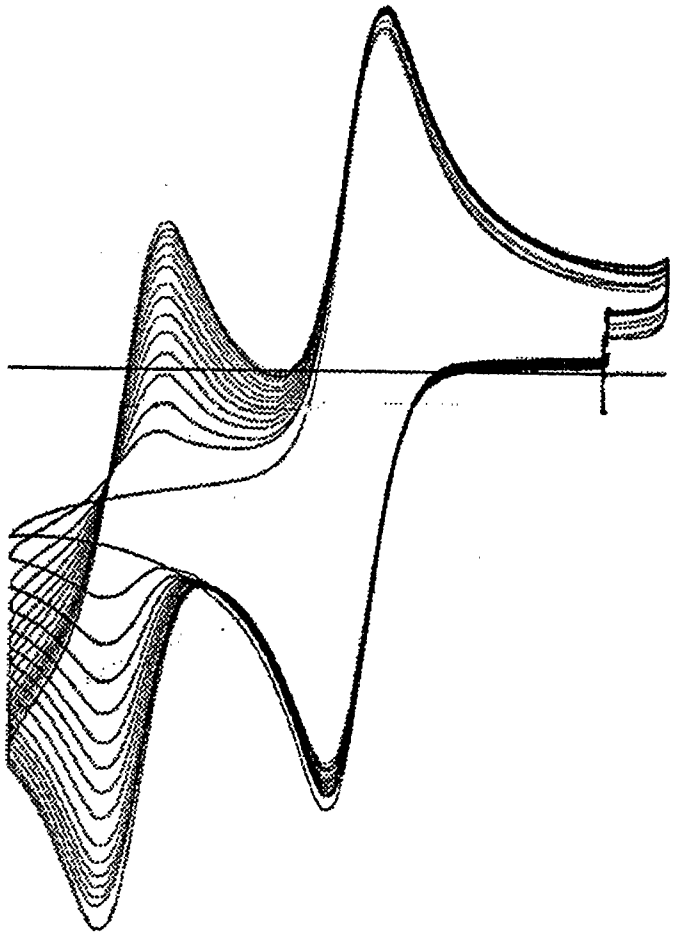

December 13, 1995 am
1.000 gram PuO_2 assemblage
0.5964 g $FeCl_2$-$4H_2O$ = 40 *mM* Fe
75 ml of 7 *M* HCl in agitated cell
double junction reference electrode
platinum working electrode
X = 200 mV/in
Y = 0.1 mA/in
rest potential = -0.1 V
scanned potential range = -0.2 V to +0.8 V
scan rate = 200 mV/sec
agitation = 500 rpm
temperature = 50°C

Figure A-12: Experimental data for December 13, 1995 am.

December 13, 1995 pm: The data for this assemblage experiment were rejected from further analysis due working electrode problems, however, the experiment produced a slope for the surface chemical reaction controlled model of 0.00366 min^{-1}, having a linear correlation coefficient of 0.998. In attempting to determine the best fit linearized form of the three nonporous shrinking sphere models, the last point was omitted from this data set (see the regression coefficient data presented in Table 4.2).

Table A-13: Experimental Data for December 13, 1995 pm.

Time (min)	Extent of Reaction	Total Coulombs	Temperature (°C)
0	0	0	49.8
10	0.113	34	50
20	0.218	68	50
30	0.317	101	50.3
40	0.394	128	50
50	0.458	151	50
60	0.521	175	50
70	0.578	196	50
80	0.634	215	50
90	0.704	234	50
100	0.746	253	50
110	0.782	271	50.2
120	0.824	288	50
130	0.866	307	50
140	0.894	319	50
150	0.908	330	50
160	0.922	340	50
170	0.944	348	50
190	1.000	362	50

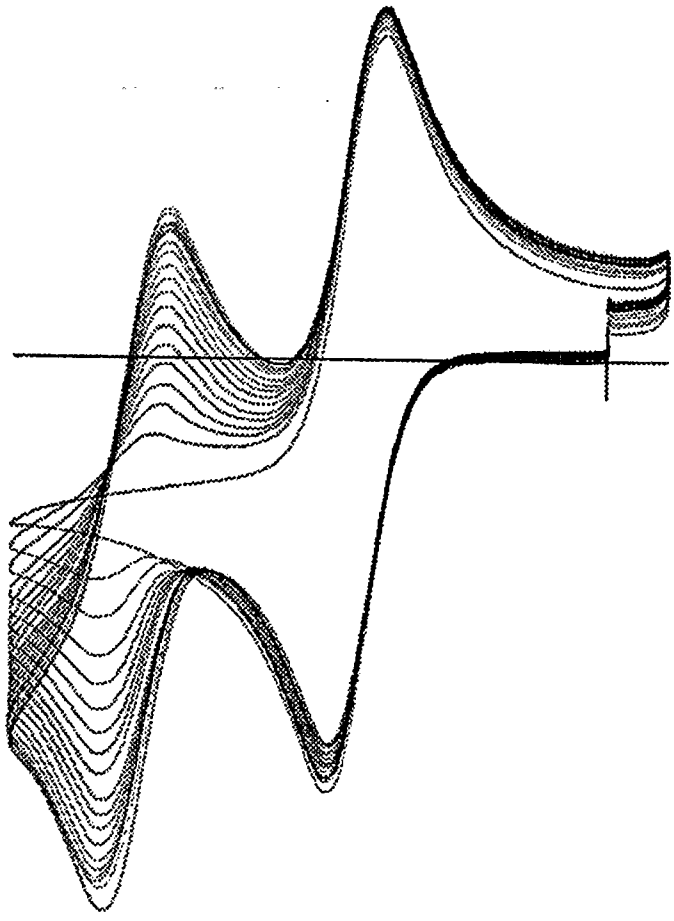

December 13, 1995 pm
1.000 gram PuO_2 assemblage
0.5964 g $FeCl_2$-$4H_2O$ = 40 *mM* Fe
75 ml of 7 *M* HCl in agitated cell
double junction reference electrode
platinum working electrode
X = 200 mV/in
Y = 0.1 mA/in
rest potential = -0.1 V
scanned potential range = -0.2 V to +0.8 V
scan rate = 200 mV/sec
agitation = 500 rpm
temperature = 50°C

Figure A-13: Experimental data for December 13, 1995 pm.

December 19, 1995: The data for this assemblage experiment produced a slope for the surface chemical reaction controlled model of 0.00435 min^{-1}, having a linear correlation coefficient of 0.997. In attempting to determine the best fit linearized form of the three nonporous shrinking sphere models, the last three points were omitted from this data set (see the regression coefficient data presented in Table 4.2).

Table A-14: Experimental Data for December 19, 1995.

Time (min)	Extent of Reaction	Total Coulombs	Temperature (°C)
0	0	0	50
10	0.128	38	50
20	0.250	76	50
30	0.338	109	50
40	0.426	137	50
50	0.514	167	50
60	0.581	187	50
70	0.642	211	50
80	0.709	235	50
90	0.770	251	50
100	0.811	269	50
110	0.845	286	50
120	0.899	302	50
130	0.919	315	50
140	0.953	328	50
150	0.973	337	50
160	0.986	345	50
170	1.000	352	50

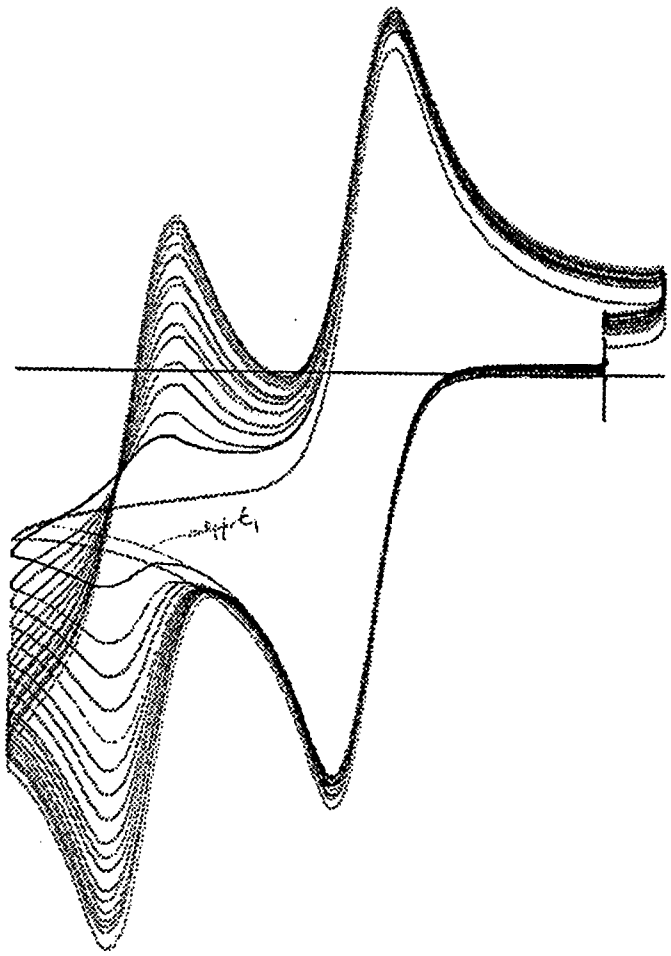

December 19, 1995
1.000 gram PuO_2 assemblage
0.5964 g $FeCl_2$-$4H_2O$ = 40 *mM* Fe
75 ml of 7 *M* HCl in agitated cell
double junction reference electrode
platinum working electrode
X = 200 mV/in
Y = 0.1 mA/in
rest potential = -0.1 V
scanned potential range = -0.2 V to +0.8 V
scan rate = 200 mV/sec
agitation = 500 rpm
temperature = 50°C

Figure A-14: Experimental data for December 19, 1995.

December 20, 1995: The data for this experiment was gathered from -38+25 μm material and produced a slope for the surface chemical reaction controlled model of 0.00495 min^{-1}, having a linear correlation coefficient of 0.997. In attempting to determine the best fit linearized form of the three nonporous shrinking sphere models, the last two points were omitted from this data set (see the regression coefficient data presented in Table 4.2).

Table A-15: Experimental Data for December 20, 1995.

Time (min)	Extent of Reaction	Total Coulombs	Temperature (°C)
0	0	0	50.1
10	0.166	40	49.9
20	0.310	89	50
30	0.414	126	50.1
40	0.490	154	50
50	0.566	179	50
60	0.648	204	50
70	0.703	228	50
80	0.766	249	50
90	0.828	273	50
100	0.876	290	50
110	0.910	311	50
120	0.986	326	50
140	1.000	347	50

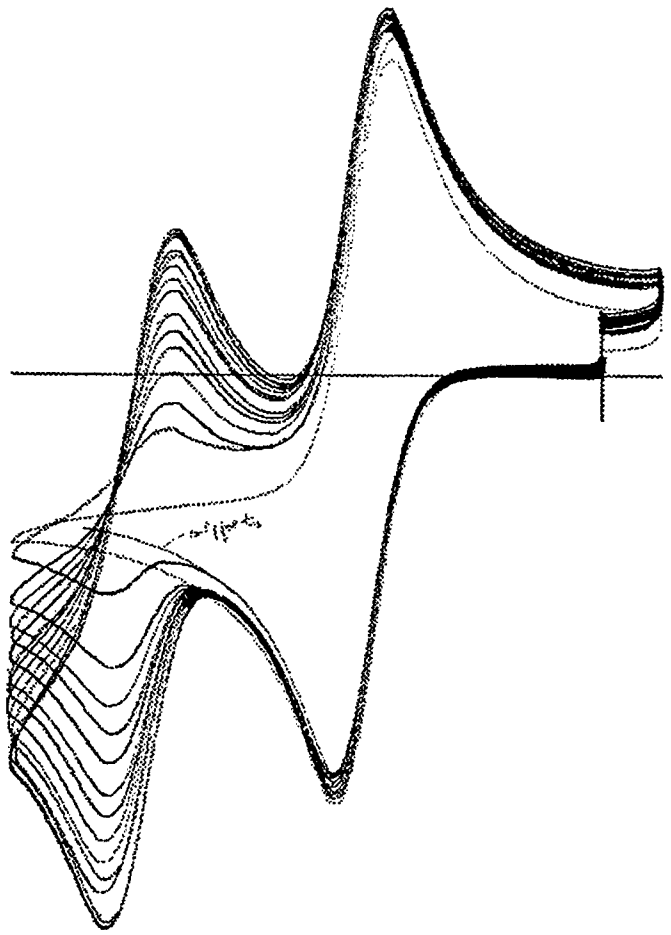

December 20, 1995
1.000 gram -38+25 micron PuO_2
0.5964 g $FeCl_2$-$4H_2O$ = 40 *mM* Fe
75 ml of 7 *M* HCl in agitated cell
double junction reference electrode
platinum working electrode
X = 200 mV/in
Y = 0.1 mA/in
rest potential = -0.1 V
scanned potential range = -0.2 V to +0.8 V
scan rate = 200 mV/sec
agitation = 500 rpm
temperature = 50°C

Figure A-15: Experimental data for December 20, 1995.

January 9, 1996: The data for this experiment was gathered from -25+15 μm material and produced a slope for the surface chemical reaction controlled model of 0.00446 min^{-1}, having a linear correlation coefficient of 0.996. In attempting to determine the best fit linearized form of the three nonporous shrinking sphere models, the last three points were omitted from this data set (see the regression coefficient data presented in Table 4.2).

Table A-16: Experimental Data for January 9, 1996.

Time (min)	Extent of Reaction	Total Coulombs	Temperature (°C)
0	0	0	50.2
10	0.168	28	50
20	0.272	58	50
30	0.376	93	50
40	0.48	125	50
50	0.552	152	50
60	0.624	173	50
70	0.672	193	50
80	0.728	211	50
90	0.776	230	50
100	0.824	247	50
110	0.856	265	50
120	0.904	279	50
130	0.944	293	50.3
140	0.968	306	50
160	1.000	329	50

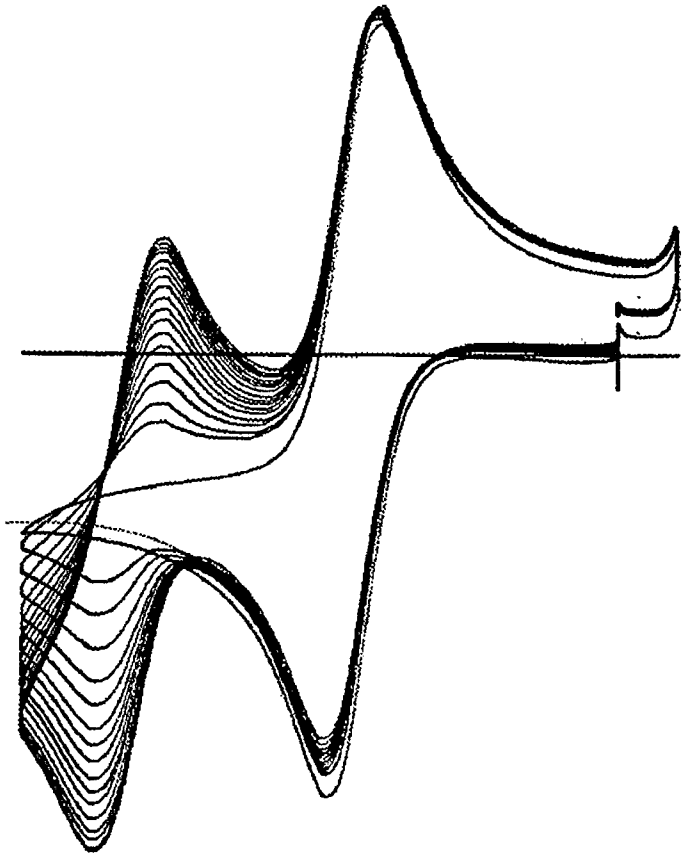

January 9, 1996
1.000 gram -25+15 micron PuO_2
0.5964 g $FeCl_2$-$4H_2O$ = 40 *mM* Fe
75 ml of 7 *M* HCl in agitated cell
double junction reference electrode
platinum working electrode
X = 200 mV/in
Y = 0.1 mA/in
rest potential = -0.1 V
scanned potential range = -0.2 V to +0.8 V
scan rate = 200 mV/sec
agitation = 500 rpm temperature = 50°C

Figure A-16: Experimental data for January 9, 1996.

January 10, 1996 am: The data for this experiment was gathered from -15+10 μm material and was rejected from further analysis due working electrode problems. The experiment, however, produced a slope for the surface chemical reaction controlled model of 0.00356 min^{-1}, having a linear correlation coefficient of 0.993. In attempting to determine the best fit linearized form of the three nonporous shrinking sphere models, the last point was omitted from this data set (see the regression coefficient data presented in Table 4.2).

Table A-17: Experimental Data for January 10, 1996 am.

Time (min)	Extent of Reaction	Total Coulombs	Temperature (°C)
0	0	0	50
10	0.118	26	50
20	0.228	61	50
30	0.315	90	50
40	0.402	117	50
50	0.480	143	50
60	0.543	165	50
70	0.598	187	50
80	0.646	205	50
90	0.685	225	50
100	0.740	245	50
110	0.764	264	50
120	0.803	281	50
130	0.827	296	50
140	1.000	340	50

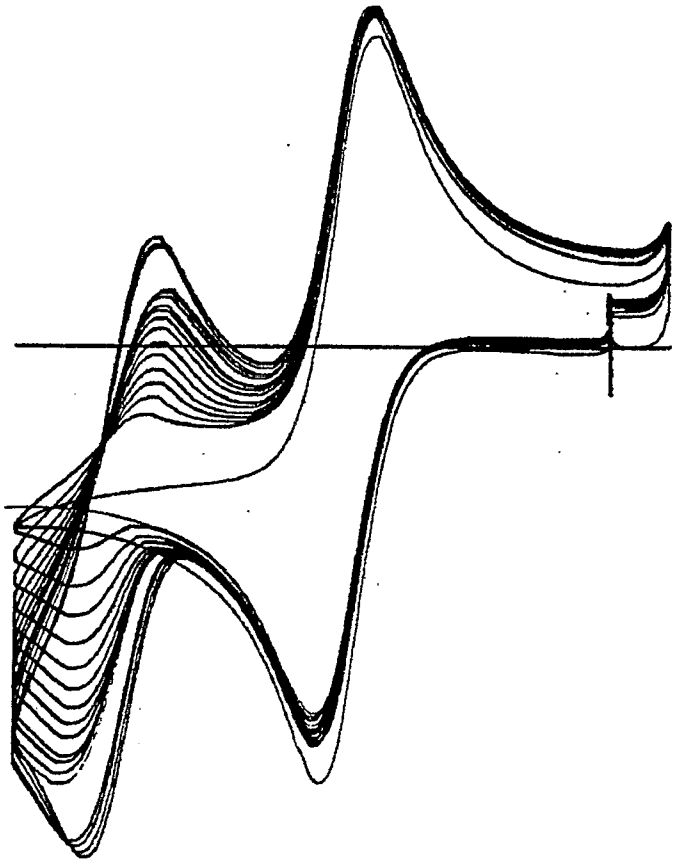

January 10, 1996 am
1.000 gram -15+10 micron PuO_2
0.5964 g $FeCl_2$-$4H_2O$ = 40 *mM* Fe
75 ml of 7 *M* HCl in agitated cell
double junction reference electrode
platinum working electrode
X = 200 mV/in
Y = 0.1 mA/in
rest potential = -0.1 V
scanned potential range = -0.2 V to +0.8 V
scan rate = 200 mV/sec
agitation = 500 rpm
temperature = 50°C

Figure A-17: Experimental data for January 10, 1996 am.

January 10, 1996 pm: The data for this experiment was gathered from -15+10 μm material and was rejected from further analysis due working electrode and serious temperature control problems due to facility voltage spikes. The experiment, however, produced a slope for the surface chemical reaction controlled model of 0.00454 min^{-1}, having a linear correlation coefficient of 0.995. In attempting to determine the best fit linearized form of the three nonporous shrinking sphere models, no points were omitted from this data set (see the regression coefficient data presented in Table 4.2).

Table A-18: Experimental Data for January 10, 1996 pm.

Time (min)	Extent of Reaction	Total Coulombs	Temperature (°C)
0	0	0	50
10	0.142	30	50
20	0.283	68	50
30	0.339	98	50
45	0.504	140	50
55	0.575	164	50
65	0.646	195	58

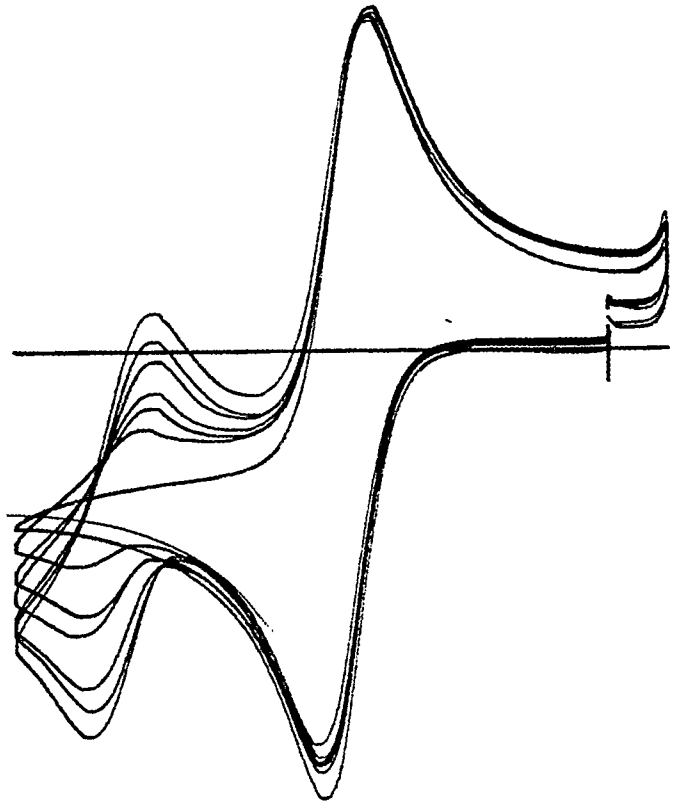

January 10, 1996 pm
1.000 gram -15+10 micron PuO_2
0.5964 g $FeCl_2$-$4H_2O$ = 40 *mM* Fe
75 ml of 7 *M* HCl in agitated cell
double junction reference electrode
platinum working electrode
X = 200 mV/in
Y = 0.1 mA/in
rest potential = -0.1 V
scanned potential range = -0.2 V to +0.8 V
scan rate = 200 mV/sec
agitation = 500 rpm
temperature = 50°C

Figure A-18: Experimental data for January 10, 1996 pm.

January 11, 1996: The data for this experiment was gathered from -15+10 μm material and was rejected from further analysis due working electrode problems and a low acid concentration (titrated at 6 *M*). These data were not included in either Figure 4.11 or 4.12 in the main body of the text. The experiment produced a slope for the surface chemical reaction controlled model of 0.00211 min^{-1}, having a linear correlation coefficient of 0.930. In attempting to determine the best fit linearized form of the three nonporous shrinking sphere models, no points were omitted from this data set (these regression data were not presented in Table 4.2).

Table A-19: Experimental Data for January 11, 1996; Acid Titrated at 6 *M*.

Time (min)	Extent of Reaction	Total Coulombs	Temperature (°C)
0	0	0	50
10	0.094	21	50
20	0.179	45	50
30	0.239	65	50
40	0.308	83	50
50	0.376	98	50
60	0.410	111	50
70	0.470	123	50
80	0.504	136	50
90	0.538	148	50
120	0.581	174	50
130	0.632	185	50
148	0.650	201	49
158	0.684	211	50
170	0.701	222	50
182	0.718	234	50

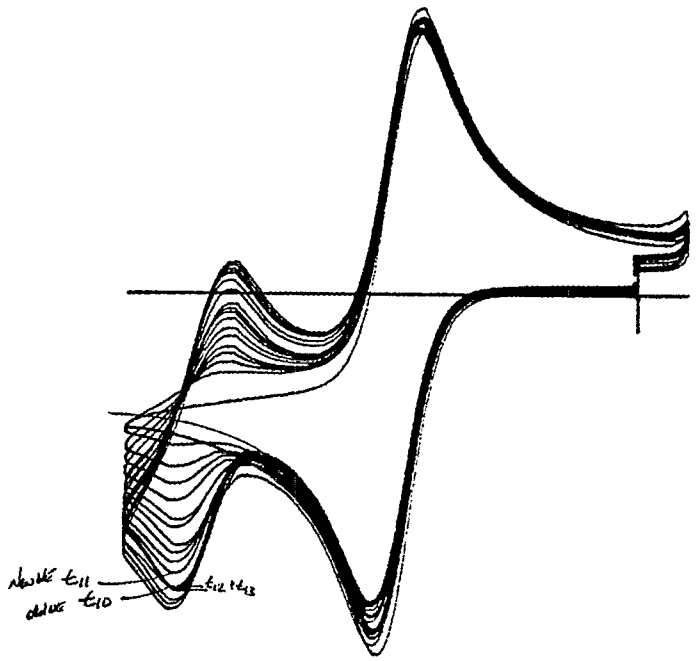

January 11, 1996
1.000 gram -15+10 micron PuO_2
0.5964 g $FeCl_2$-$4H_2O$ = 40 *mM* Fe
75 ml of 6 *M* HCl in agitated cell
double junction reference electrode
platinum working electrode
X = 200 mV/in
Y = 0.1 mA/in
rest potential = -0.1 V
scanned potential range = -0.2 V to +0.8 V
scan rate = 200 mV/sec
agitation = 500 rpm
temperature = 50°C

Figure A-19: Experimental data for January 11, 1996; acid titrated at 6 *M*.

January 12, 1996: The data for this experiment was gathered from -15+10 μm material and was rejected from further analysis due working electrode problems and a low acid concentration (titrated at 6 *M*). These data were not included in either Figure 4.11 or 4.12 in the main body of the text. The experiment produced a slope for the surface chemical reaction controlled model of 0.00195 min^{-1}, having a linear correlation coefficient of 0.984. In attempting to determine the best fit linearized form of the three nonporous shrinking sphere models, the last point was omitted from this data set (these regression data were not presented in Table 4.2).

Table A-20: Experimental Data for January 12, 1996; Acid Titrated at 6 *M*.

Time (min)	Extent of Reaction	Total Coulombs	Temperature (°C)
0	0	0	50
10	0.077	30	50
20	0.145	51	50.3
30	0.197	70	50
40	0.265	86	50
50	0.308	100	50
60	0.342	114	50
70	0.393	126	50
80	0.427	137	50
90	0.462	148	50
100	0.487	158	50
115	0.538	173	50
132	0.573	192	50
147	0.632	205	50
162	0.667	220	50
177	0.692	235	50
309	1.000	346	51

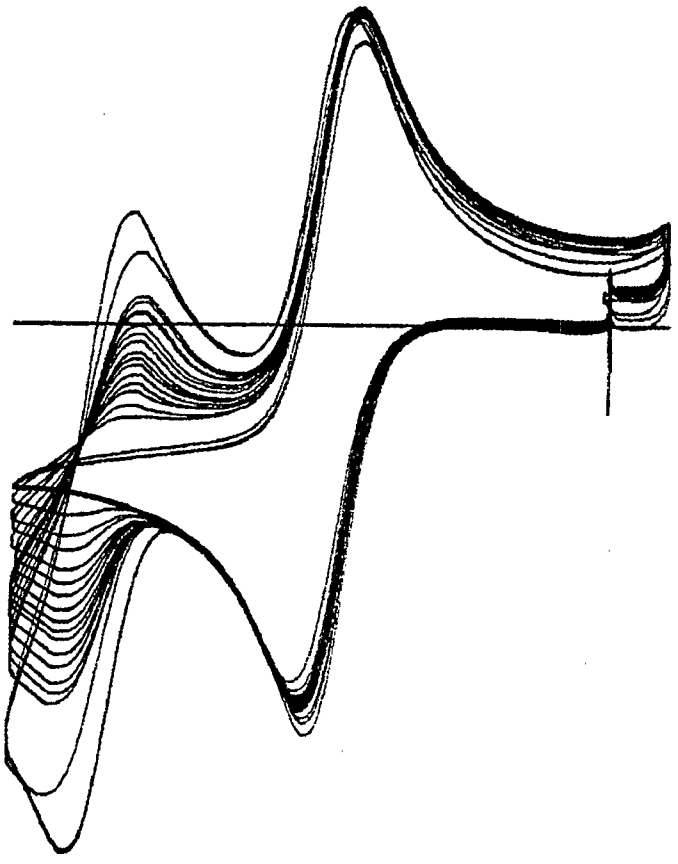

January 12, 1996
1.000 gram -15+10 micron PuO_2
0.5964 g $FeCl_2$-$4H_2O$ = 40 *mM* Fe
75 ml of 6 *M* HCl in agitated cell
double junction reference electrode
platinum working electrode
X = 200 mV/in
Y = 0.1 mA/in
rest potential = -0.1 V
scanned potential range = -0.2 V to +0.8 V
scan rate = 200 mV/sec
agitation = 500 rpm
temperature = 50°C

Figure A-20: Experimental data for January 12, 1996; acid titrated at 6 *M*.

January 16, 1996 am: The data for this assemblage experiment produced a slope for the surface chemical reaction controlled model of 0.0040 min^{-1}, having a linear correlation coefficient of 0.999. In attempting to determine the best fit linearized form of the three nonporous shrinking sphere models, the last three points were omitted from this data set (see the regression coefficient data presented in Table 4.2).

Table A-21: Experimental Data for January 16, 1996 am.

Time (min)	Extent of Reaction	Total Coulombs	Temperature (°C)
0	0	0	49.8
10	0.128	33	50
20	0.227	76	50
30	0.326	108	50
40	0.411	137	50
50	0.489	162	50
60	0.560	186	50
70	0.624	207	50
80	0.681	227	50
90	0.723	246	50
100	0.780	263	50
110	0.816	280	50
120	0.858	295	49
130	0.894	311	50
140	0.922	320	50
150	0.957	330	50
160	0.979	339	50
170	1.000	346	50

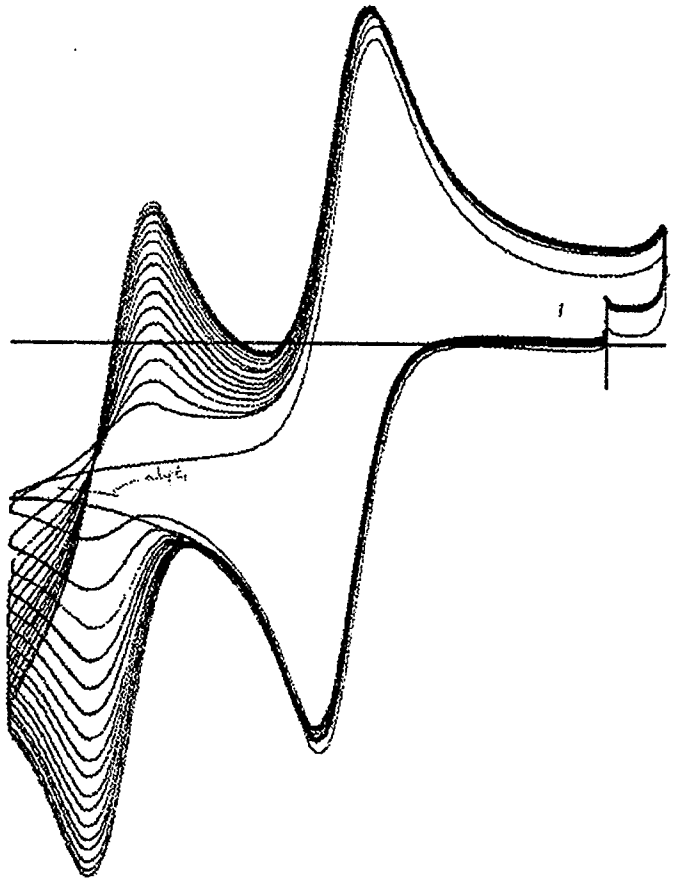

January 16, 1996 am
1.000 gram PuO_2 assemblage
0.5964 g $FeCl_2$-$4H_2O$ = 40 *mM* Fe
75 ml of 7 *M* HCl in agitated cell
double junction reference electrode
platinum working electrode
X = 200 mV/in
Y = 0.1 mA/in
rest potential = -0.1 V
scanned potential range = -0.2 V to +0.8 V
scan rate = 200 mV/sec
agitation = 500 rpm
temperature = 50°C

Figure A-21: Experimental data for January 16, 1996 am.

January 16, 1996 pm: This experiment was performed on -15+10 μm material and produced a slope for the surface chemical reaction controlled model of 0.00439 min^{-1}, having a linear correlation coefficient of 0.995. In attempting to determine the best fit linearized form of the three nonporous shrinking sphere models, the last three points were omitted from this data set (see the regression coefficient data presented in Table 4.2).

Table A-22: Experimental Data for January 16, 1996 pm.

Time (min)	Extent of Reaction	Total Coulombs	Temperature (°C)
0	0	0	50
10	0.157	40	50
20	0.276	82	50
30	0.378	117	50
40	0.465	146	50
50	0.535	171	50
60	0.598	195	50
70	0.661	218	50
80	0.717	238	50
90	0.764	257	50
100	0.803	277	50
110	0.866	295	50
120	0.906	310	50
130	0.937	324	50
140	0.969	335	50
150	1.000	350	50

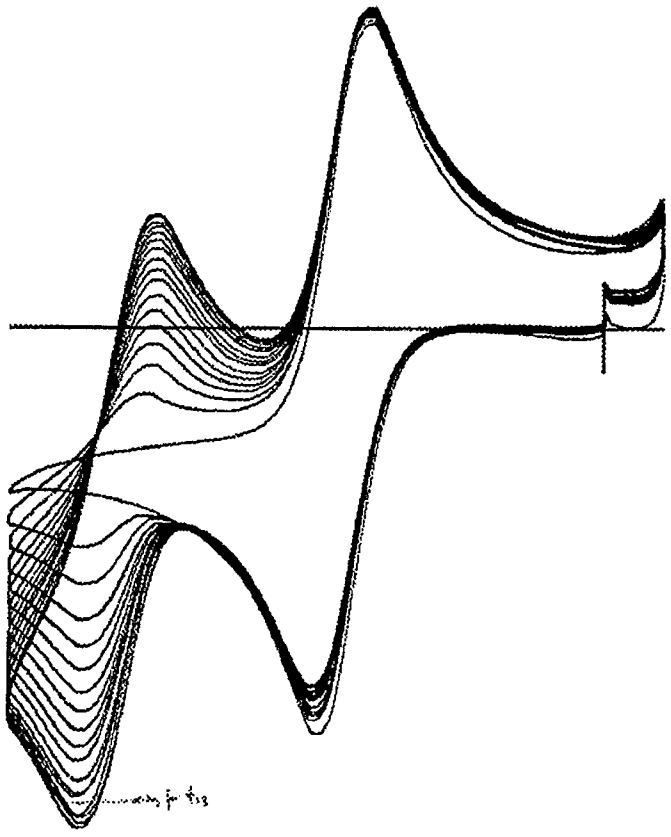

January 16, 1996 pm
1.000 gram -15+10 micron PuO_2
0.5964 g $FeCl_2$-$4H_2O$ = 40 *mM* Fe
75 ml of 7 *M* HCl in agitated cell
double junction reference electrode
platinum working electrode
X = 200 mV/in
Y = 0.1 mA/in
rest potential = -0.1 V
scanned potential range = -0.2 V to +0.8 V
scan rate = 200 mV/sec
agitation = 500 rpm
temperature = 50°C

Figure A-22: Experimental data for January 16, 1996 pm.

January 17, 1996: This experiment was performed on -10+5 μm material and produced a slope for the surface chemical reaction controlled model of 0.00480 min^{-1}, having a linear correlation coefficient of 0.993. In attempting to determine the best fit linearized form of the three nonporous shrinking sphere models, the last point was omitted from this data set (see the regression coefficient data presented in Table 4.2).

Table A-23: Experimental Data for January 17, 1996.

Time (min)	Extent of Reaction	Total Coulombs	Temperature (°C)
0	0	0	49.8
10	0.181	38	50
20	0.310	82	50
30	0.405	117	50
40	0.500	146	50
50	0.578	172	50
60	0.638	197	50
70	0.733	221	51
80	0.776	241	50
90	0.802	261	50
100	0.836	280	49
110	0.897	294	50
120	0.922	310	49
130	0.957	323	50
140	1.000	338	50

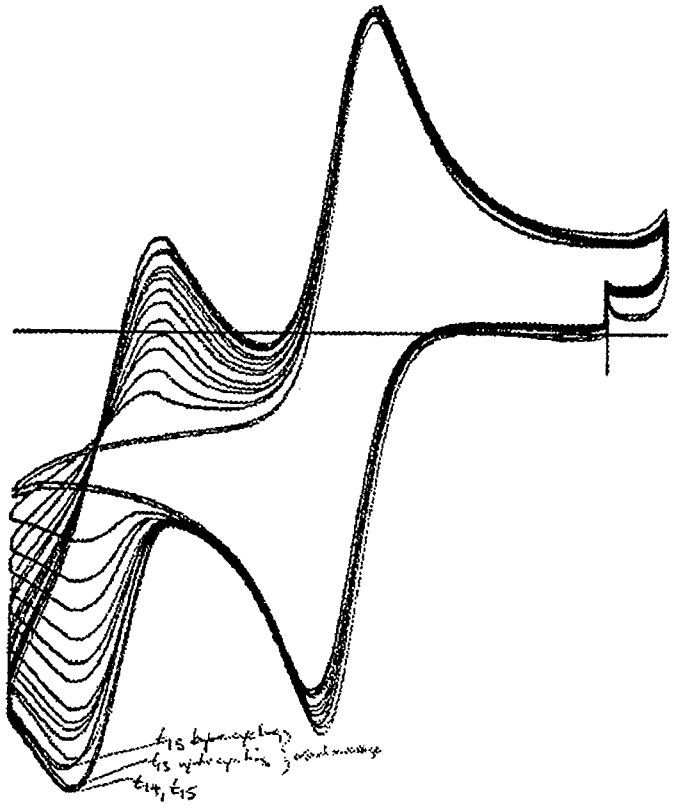

January 17, 1996
1.000 gram -10+5 micron PuO_2
0.5964 g $FeCl_2$-$4H_2O$ = 40 *mM* Fe
75 ml of 7 *M* HCl in agitated cell
double junction reference electrode
platinum working electrode
X = 200 mV/in
Y = 0.1 mA/in
rest potential = -0.1 V
scanned potential range = -0.2 V to +0.8 V
scan rate = 200 mV/sec
agitation = 500 rpm
temperature = 50°C

Figure A-23: Experimental data for January 17, 1996.

January 18, 1996: This experiment was performed on -5 μm material and produced a slope for the surface chemical reaction controlled model of 0.00441 min^{-1}, having a linear correlation coefficient of 0.997. In attempting to determine the best fit linearized form of the three nonporous shrinking sphere models, the last two points were omitted from this data set (see the regression coefficient data presented in Table 4.2).

Table A-24: Experimental Data for January 18, 1996.

Time (min)	Extent of Reaction	Total Coulombs	Temperature (°C)
0	0	0	50
10	0.126	37	50
20	0.236	75	50
30	0.354	113	50
40	0.433	136	50
50	0.512	160	50
60	0.591	182	50
70	0.654	204	50
80	0.709	223	50
90	0.764	243	50
100	0.811	259	50
110	0.858	275	50
120	0.906	290	50
130	0.929	304	50
140	0.953	316	50
150	0.984	325	50
160	1.000	337	50

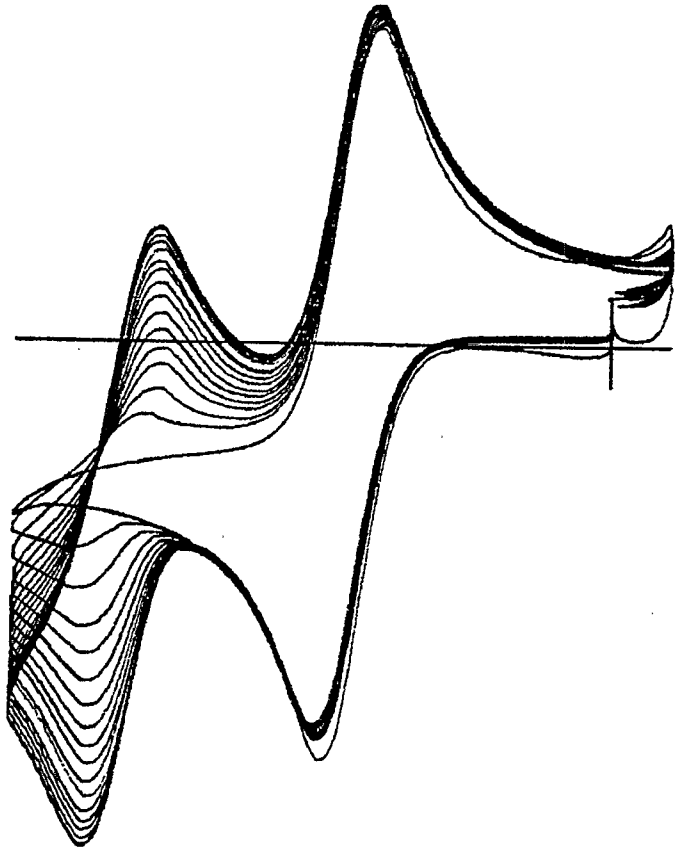

January 18, 1996
1.000 gram -5 micron PuO_2
0.5964 g $FeCl_2$-$4H_2O$ = 40 *mM* Fe
75 ml of 7 *M* HCl in agitated cell
double junction reference electrode
platinum working electrode
X = 200 mV/in
Y = 0.1 mA/in
rest potential = -0.1 V
scanned potential range = -0.2 V to +0.8 V
scan rate = 200 mV/sec
agitation = 500 rpm
temperature = 50°C

Figure A-24: Experimental data for January 18, 1996.

January 24, 1996: This assemblage experiment was used in the Arrhenius evaluation of the reaction activation energy. The slope of the plot of the surface chemical reaction controlled model was determined to be 0.00759 min^{-1} with a linear correlation coefficient of 0.998. In attempting to determine the best fit linearized form of the three nonporous shrinking sphere models, the last two points were omitted from this data set (these regression data were not presented in Table 4.2).

Table A-25: Experimental Data for January 24, 1996; Arrhenius Data at 60°C.

Time (min)	Extent of Reaction	Total Coulombs	Temperature (°C)
0	0	0	60
10	0.253	69	60
20	0.418	136	60
30	0.551	188	60
40	0.652	229	60
50	0.753	269	60
60	0.835	299	60
70	0.892	323	60
80	0.943	344	60
90	0.975	357	60
100	1.000	370	60

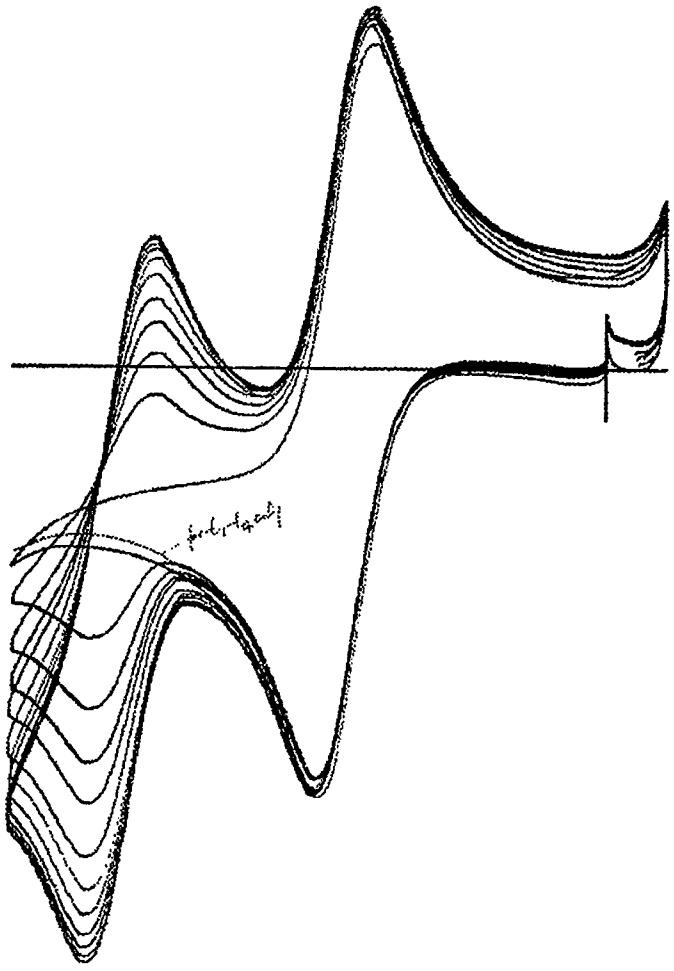

January 24, 1996
1.000 gram PuO_2 assemblage
0.5964 g $FeCl_2$-$4H_2O$ = 40 *mM* Fe
75 ml of 7 *M* HCl in agitated cell
double junction reference electrode
platinum working electrode
X = 200 mV/in
Y = 0.1 mA/in
rest potential = -0.1 V
scanned potential range = -0.2 V to +0.8 V
scan rate = 200 mV/sec
agitation = 500 rpm temperature = 60°C

Figure A-25: Experimental data for January 24, 1996; Arrhenius data at 60°C.

January 26, 1996: This assemblage experiment was used in the Arrhenius evaluation of the reaction activation energy. The slope of the plot of the surface chemical reaction controlled model was determined to be 0.0110 min^{-1} with a linear correlation coefficient of 0.998. In attempting to determine the best fit linearized form of the three nonporous shrinking sphere models, the last point was omitted from this data set (these regression data were not presented in Table 4.2).

Table A-26: Experimental Data for January 26, 1996; Arrhenius Data at 65°C.

Time (min)	Extent of Reaction	Total Coulombs	Temperature (°C)
0	0	0	65.5
10	0.338	93	66
20	0.529	167	65.5
30	0.694	239	65
40	0.834	289	65
50	0.904	324	65
60	0.962	352	65
73	1.000	375	65

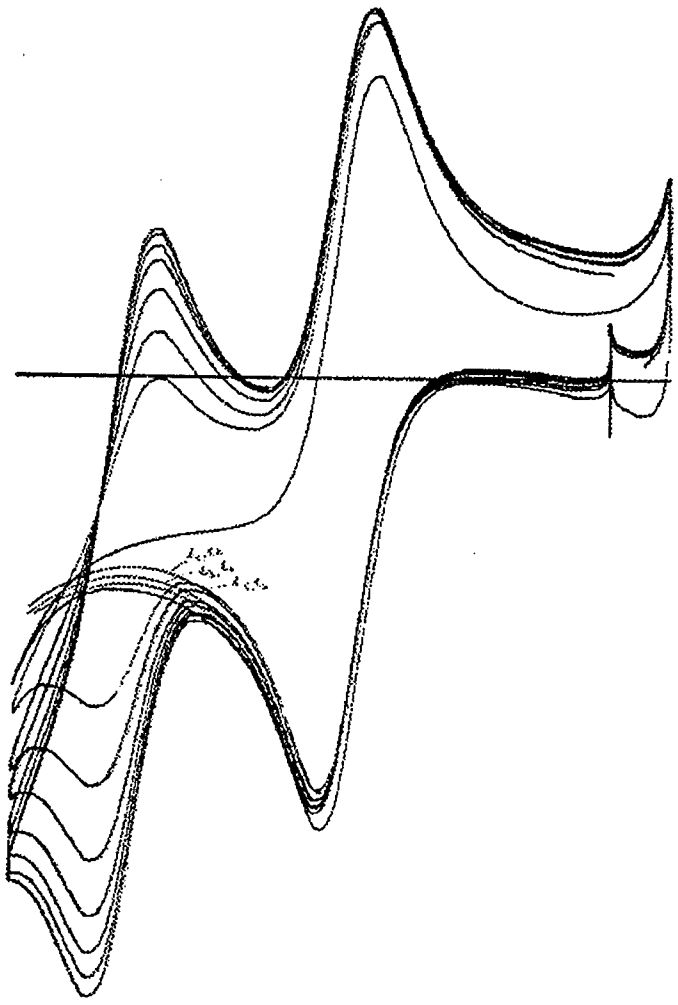

January 26, 1996
1.000 gram PuO_2 assemblage
0.5964 g $FeCl_2$-$4H_2O$ = 40 *mM* Fe
75 ml of 7 *M* HCl in agitated cell
double junction reference electrode
platinum working electrode
X = 200 mV/in
Y = 0.1 mA/in
rest potential = -0.1 V
scanned potential range = -0.2 V to +0.8 V
scan rate = 200 mV/sec
agitation = 500 rpm
temperature = 65°C

Figure A-26: Experimental data for January 26, 1996; Arrhenius data at 65°C.

February 8, 1996: This experiment was performed on -38+25 μm material and produced a slope for the surface chemical reaction controlled model of 0.00443 min^{-1}, having a linear correlation coefficient of 0.995. In attempting to determine the best fit linearized form of the three nonporous shrinking sphere models, the last two points were omitted from this data set (see the regression coefficient data presented in Table 4.2).

Table A-27: Experimental Data for February 8, 1996.

Time (min)	Extent of Reaction	Total Coulombs	Temperature (°C)
0	0	0	50
10	0.169	44	50
20	0.291	89	50
30	0.392	123	50
40	0.466	153	50
50	0.554	179	50
60	0.615	204	50
70	0.676	225	50
82	0.743	248	50
97	0.791	266	50
115	0.865	293	49.8
125	0.905	307	50
135	0.939	318	50
145	0.959	328	50
155	0.980	335	50
165	1.000	344	50

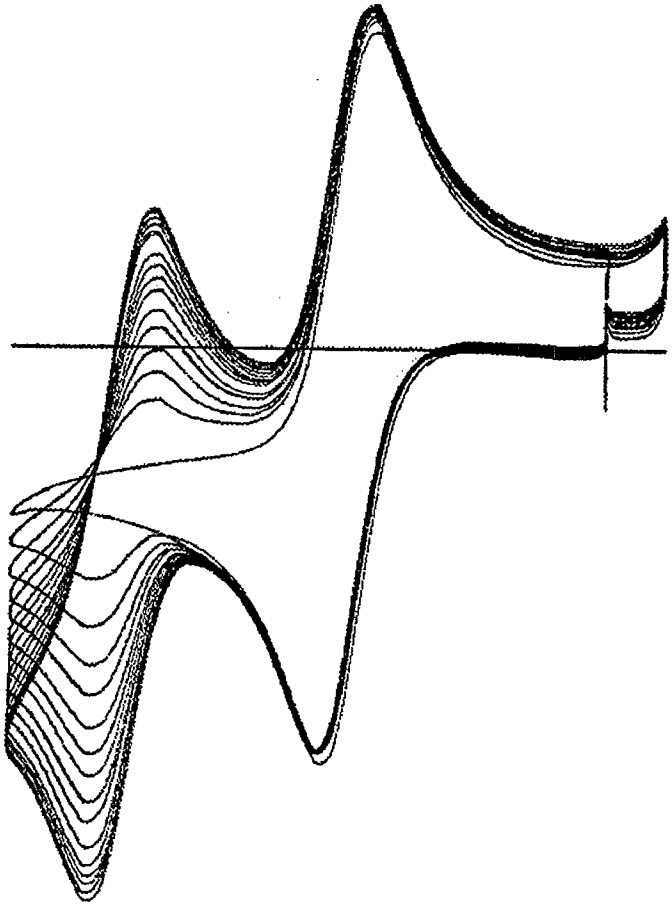

February 8, 1996
1.000 gram -38+25 micron PuO_2
0.5964 g $FeCl_2$-$4H_2O$ = 40 *mM* Fe
75 ml of 7 *M* HCl in agitated cell
double junction reference electrode
platinum working electrode
X = 200 mV/in
Y = 0.1 mA/in
rest potential = -0.1 V
scanned potential range = -0.2 V to +0.8 V
scan rate = 200 mV/sec
agitation = 500 rpm
temperature = 50°C

Figure A-27: Experimental data for February 8, 1996.

February 13, 1996: This experiment was performed on -25+15 μm material and produced a slope for the surface chemical reaction controlled model of 0.00409 min^{-1}, having a linear correlation coefficient of 0.995. In attempting to determine the best fit linearized form of the three nonporous shrinking sphere models, the last point was omitted from this data set (see the regression coefficient data presented in Table 4.2).

Table A-28: Experimental Data for February 13, 1996.

Time (min)	Extent of Reaction	Total Coulombs	Temperature (°C)
0	0	0	50
10	0.145	41	50
20	0.250	82	50
30	0.342	116	50
40	0.428	145	50
50	0.493	171	50
60	0.559	194	50
70	0.618	216	50
80	0.671	234	50
90	0.724	253	50
100	0.776	272	50
110	0.816	288	50
120	0.855	305	50
130	0.888	317	50
140	0.921	328	50
150	0.947	338	50
160	0.967	345	50
170	0.980	351	50
180	1.000	356	50

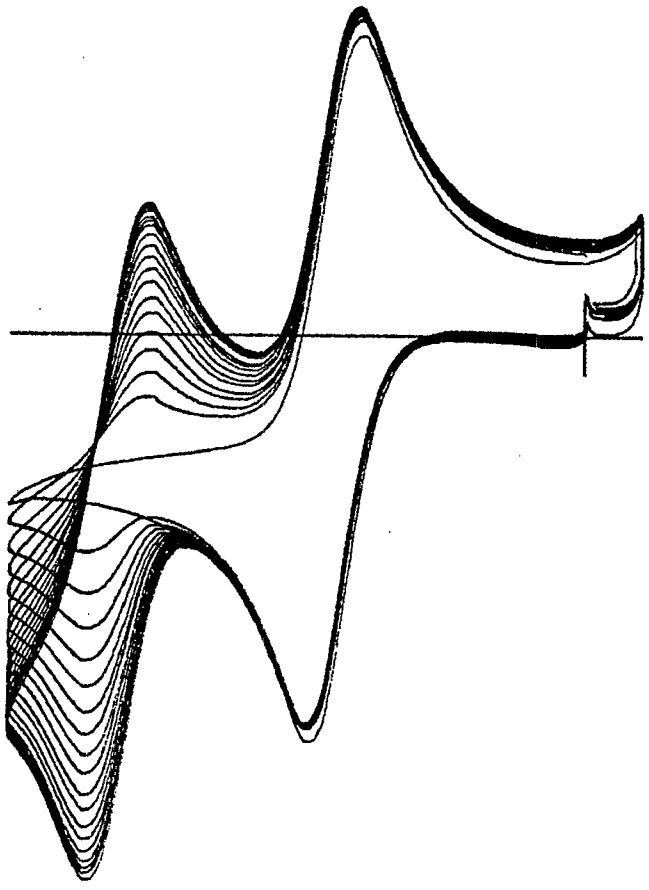

February 13, 1996
1.000 gram -25+15 micron PuO_2
0.5964 g $FeCl_2$-$4H_2O$ = 40 *mM* Fe
75 ml of 7 *M* HCl in agitated cell
double junction reference electrode
platinum working electrode
X = 200 mV/in
Y = 0.1 mA/in
rest potential = -0.1 V
scanned potential range = -0.2 V to +0.8 V
scan rate = 200 mV/sec
agitation = 500 rpm
temperature = 50°C

Figure A-28: Experimental data for February 13, 1996.

February 14, 1996: The data for this experiment was gathered from -10+5 μm material and was rejected from further analysis due working electrode problems. The experiment, however, produced a slope for the surface chemical reaction controlled model of 0.00370 min^{-1}, having a linear correlation coefficient of 0.995. In attempting to determine the best fit linearized form of the three nonporous shrinking sphere models, the last two points were omitted from this data set (see the regression coefficient data presented in Table 4.2).

Table A-29: Experimental Data for February 14, 1996.

Time (min)	Extent of Reaction	Total Coulombs	Temperature (°C)
0	0	0	50
10	0.118	33	50
20	0.213	74	50
30	0.294	106	50.3
40	0.375	135	50
50	0.449	164	50
60	0.522	184	50.3
70	0.566	207	50.3
80	0.610	226	50
100	0.765	266	50
120	0.831	297	50
140	0.897	322	50
150	0.956	332	50
170	1.000	347	50

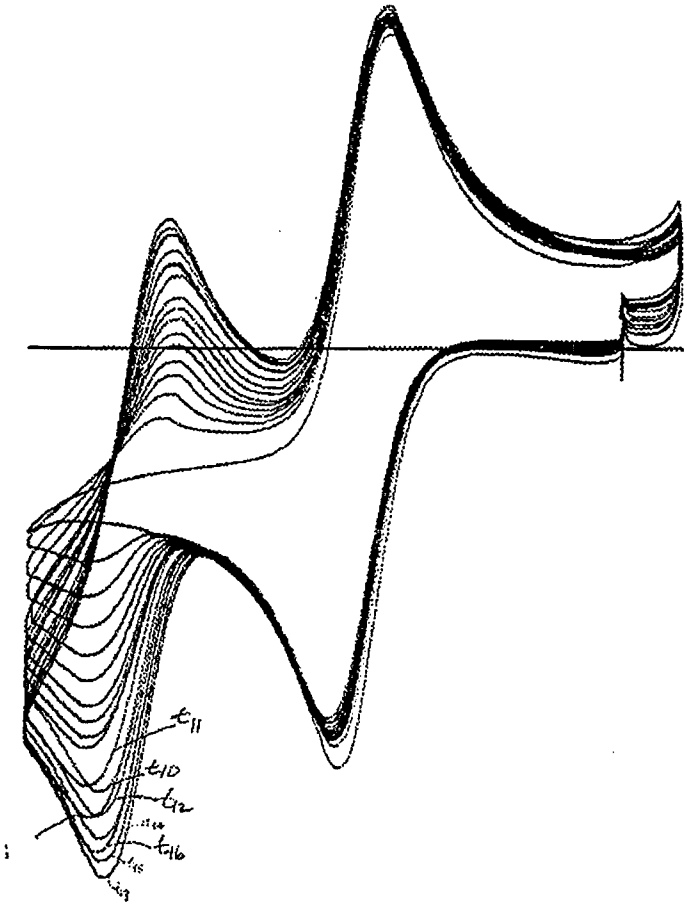

February 14, 1996
1.000 gram -10+5 micron PuO_2
0.5964 g $FeCl_2$-$4H_2O$ = 40 *mM* Fe
75 ml of 7 *M* HCl in agitated cell
double junction reference electrode
platinum working electrode
X = 200 mV/in
Y = 0.1 mA/in
rest potential = -0.1 V
scanned potential range = -0.2 V to +0.8 V
scan rate = 200 mV/sec
agitation = 500 rpm
temperature = 50°C

Figure A-29: Experimental data for February 14, 1996.

February 15, 1996 am: The data for this experiment was gathered from -10+5 μm material and was rejected from further analysis due working electrode and temperature fluctuation problems. The experiment, however, produced a slope for the surface chemical reaction controlled model of 0.00468 min^{-1}, having a linear correlation coefficient of 0.982. In attempting to determine the best fit linearized form of the three nonporous shrinking sphere models, the last point was omitted from this data set (see the regression coefficient data presented in Table 4.2).

Table A-30: Experimental Data for February 15, 1996 am.

Time (min)	Extent of Reaction	Total Coulombs	Temperature (°C)
0	0	0	50
10	0.141	40	49
20	0.258	75	50.5
30	0.313	106	50
60	0.625	185	53
80	0.742	228	51
120	0.852	292	50
130	0.945	305	50
140	0.969	316	50
150	0.984	326	50
160	1.000	340	50

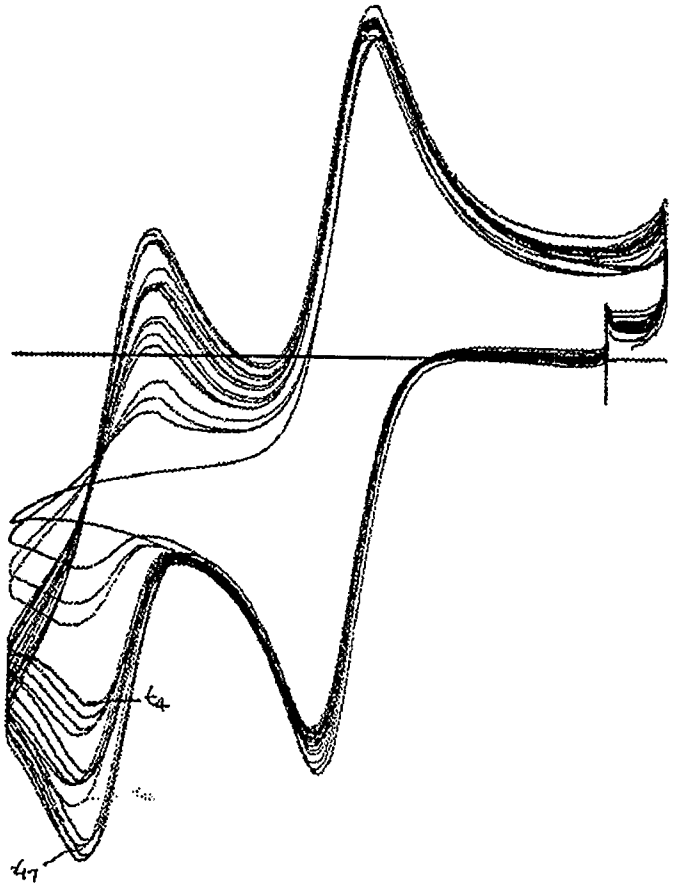

February 15, 1996 am
1.000 gram -10+5 micron PuO_2
0.5964 g $FeCl_2$-$4H_2O$ = 40 *mM* Fe
75 ml of 7 *M* HCl in agitated cell
double junction reference electrode
platinum working electrode
X = 200 mV/in
Y = 0.1 mA/in
rest potential = -0.1 V
scanned potential range = -0.2 V to +0.8 V
scan rate = 200 mV/sec
agitation = 500 rpm
temperature = 50°C

Figure A-30: Experimental data for February 15, 1996 am.

February 15, 1996 pm: The data for this assemblage experiment produced a slope for the surface chemical reaction controlled model of 0.00434 min^{-1}, having a linear correlation coefficient of 0.985. In attempting to determine the best fit linearized form of the three nonporous shrinking sphere models, the last two points were omitted from this data set (see the regression coefficient data presented in Table 4.2).

Table A-31: Experimental Data for February 15, 1996 pm.

Time (min)	Extent of Reaction	Total Coulombs	Temperature (°C)
0	0	0	50
10	0.182	40	50
20	0.306	78	50.3
30	0.421	115	50.3
40	0.504	144	50
50	0.570	168	50
60	0.628	190	50
70	0.686	211	50
80	0.744	231	50
90	0.777	249	50
100	0.818	266	50
110	0.851	281	50
120	0.876	294	50
130	0.901	306	49.5
140	0.934	317	49.5
150	0.967	326	49.5
160	1.000	335	50

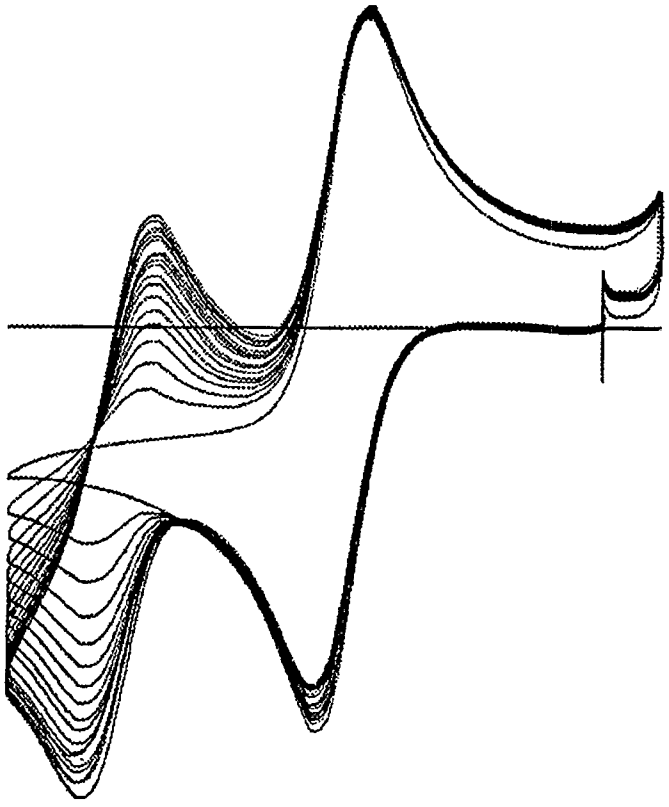

February 15, 1996 pm
1.000 gram PuO_2 assemblage
0.5964 g $FeCl_2$-$4H_2O$ = 40 *mM* Fe
75 ml of 7 *M* HCl in agitated cell
double junction reference electrode
platinum working electrode
X = 200 mV/in
Y = 0.1 mA/in
rest potential = -0.1 V
scanned potential range = -0.2 V to +0.8 V
scan rate = 200 mV/sec
agitation = 500 rpm
temperature = 50°C

Figure A-31: Experimental data for February 15, 1996 pm.

February 23, 1996: The data for this assemblage experiment produced a slope for the surface chemical reaction controlled model of 0.00437 min^{-1}, having a linear correlation coefficient of 0.997. In attempting to determine the best fit linearized form of the three nonporous shrinking sphere models, the last point was omitted from this data set (see the regression coefficient data presented in Table 4.2).

During this experiment, the electrode cleaning procedure of sweeping into the proton reduction region was demonstrated (section 3.3).

Table A-32: Experimental Data for February 23, 1996.

Time (min)	Extent of Reaction	Total Coulombs	Temperature (°C)
0	0	0	50
14	0.182	38	51
20	0.264	65	51
30	0.388	103	51
40	0.479	136	50.3
50	0.537	158	50
60	0.612	179	50
70	0.686	204	50.3
80	0.719	217	50
90	0.777	231	50
100	0.818	247	50
112	0.860	263	50
120	0.884	275	50
130	0.917	286	50
140	0.942	297	50
150	0.959	306	50
160	1.000	318	50

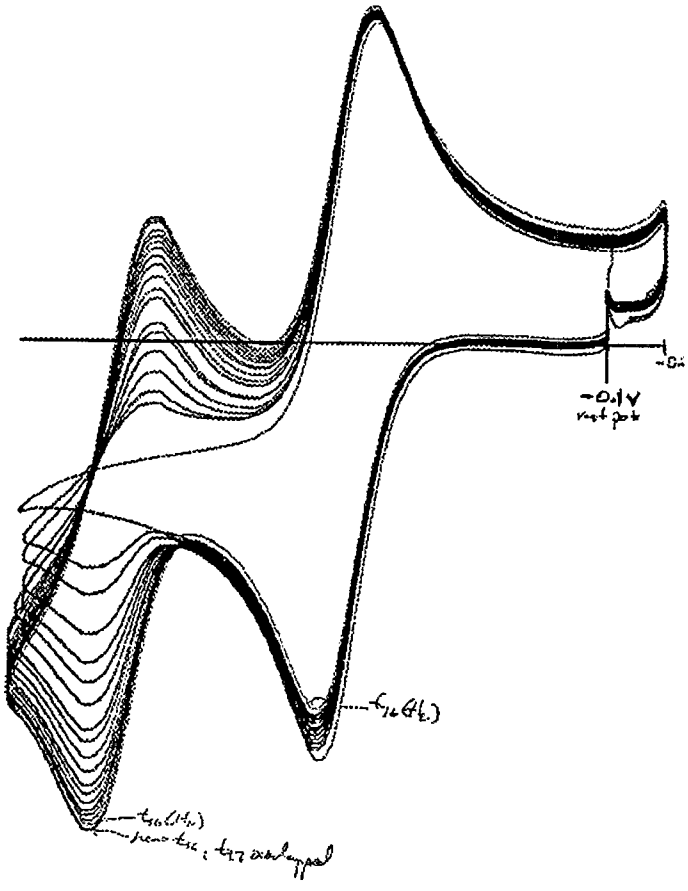

February 23, 1996
1.000 gram PuO_2 assemblage
0.5964 g $FeCl_2$-$4H_2O$ = 40 *mM* Fe
75 ml of 7 *M* HCl in agitated cell
double junction reference electrode
platinum working electrode
X = 200 mV/in
Y = 0.1 mA/in
rest potential = -0.1 V
scanned potential range = -0.2 V to +0.8 V
scan rate = 200 mV/sec
agitation = 500 rpm
temperature = 50°C

Figure A-32: Experimental data for February 23, 1996.

February 26, 1996: The data for this experiment was gathered from -10+5 μm material and was rejected from further analysis due working electrode and temperature fluctuation problems. The experiment, however, produced a slope for the surface chemical reaction controlled model of 0.00398 min^{-1}, having a linear correlation coefficient of 0.994. In attempting to determine the best fit linearized form of the three nonporous shrinking sphere models, the last two points were omitted from this data set (see the regression coefficient data presented in Table 4.2).

Table A-33: Experimental Data for February 26, 1996.

Time (min)	Extent of Reaction	Total Coulombs	Temperature (°C)
0	0	0	50
10	0.158	40	50
20	0.275	81	50.5
30	0.358	109	50
40	0.442	137	50.3
50	0.517	161	50.2
60	0.575	182	50
70	0.625	202	55
80	0.692	224	50
90	0.733	243	49
100	0.767	258	49
110	0.808	271	50
120	0.858	284	50
132	0.883	299	50
140	0.917	308	50
150	0.983	319	50
160	1.000	328	50

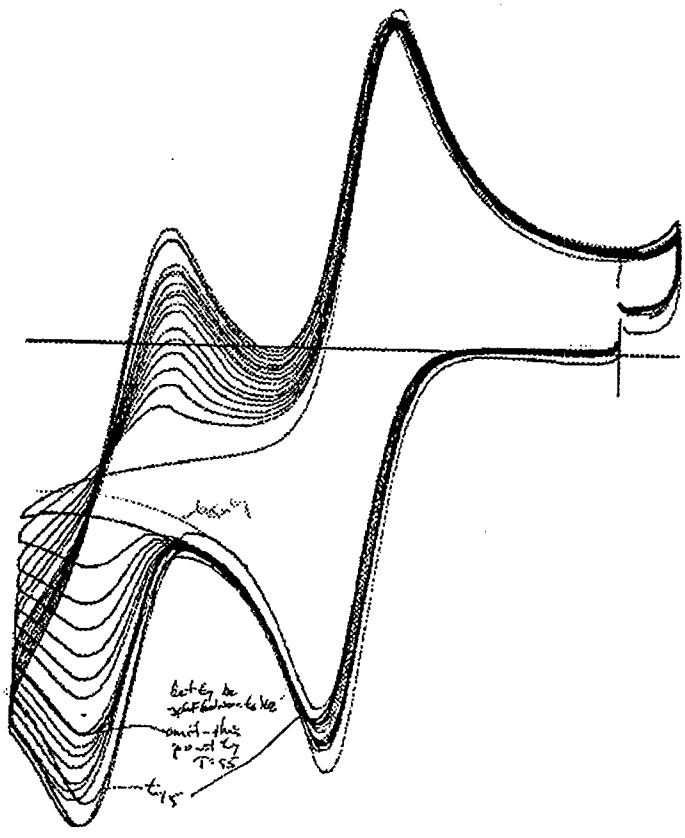

February 26, 1996
1.000 gram -10+5 micron PuO_2
0.5964 g $FeCl_2$-$4H_2O$ = 40 *mM* Fe
75 ml of 7 *M* HCl in agitated cell
double junction reference electrode
platinum working electrode
X = 200 mV/in
Y = 0.1 mA/in
rest potential = -0.1 V
scanned potential range = -0.2 V to +0.8 V
scan rate = 200 mV/sec
agitation = 500 rpm
temperature = 50°C

Figure A-33: Experimental data for February 26, 1996.

February 27, 1996 am: This experiment was performed on -53+38 μm material and produced a slope for the surface chemical reaction controlled model of 0.00476 min^{-1}, having a linear correlation coefficient of 0.996. In attempting to determine the best fit linearized form of the three nonporous shrinking sphere models, the last two points were omitted from this data set (see the regression coefficient data presented in Table 4.2).

Table A-34: Experimental Data for February 27, 1996 am.

Time (min)	Extent of Reaction	Total Coulombs	Temperature (°C)
0	0	0	50
14	0.234	56	50.5
24	0.344	99	49
34	0.430	132	50
44	0.539	160	52
54	0.602	186	50
64	0.672	209	50
74	0.727	230	50
84	0.789	251	50
94	0.828	272	50
104	0.867	288	50
114	0.906	304	50.5
124	0.922	319	50.5
134	0.961	330	50
154	1.000	348	50

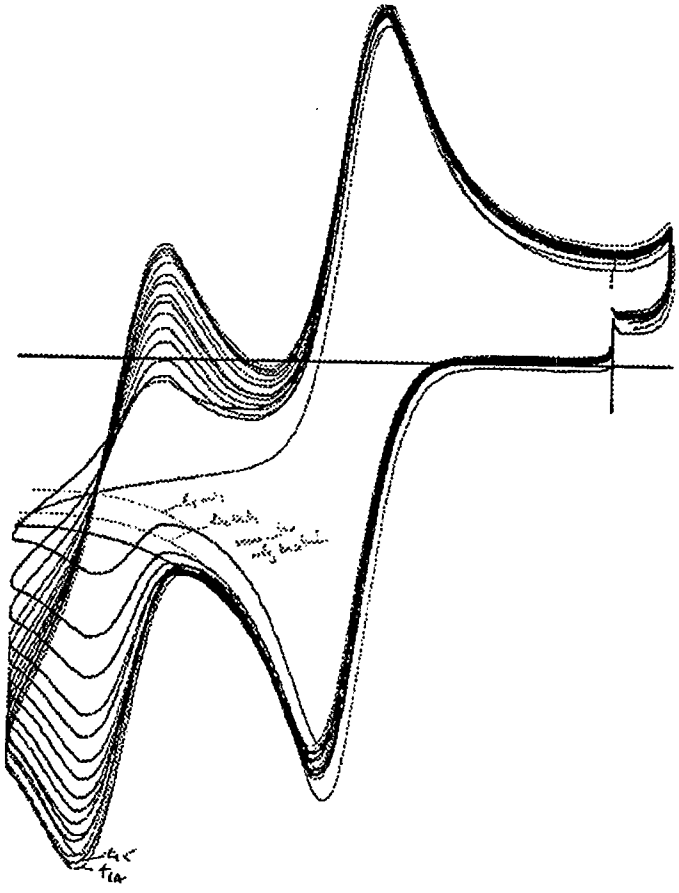

February 27, 1996 am
1.000 gram -53+38 micron PuO_2
0.5964 g $FeCl_2$-$4H_2O$ = 40 *mM* Fe
75 ml of 7 *M* HCl in agitated cell
double junction reference electrode
platinum working electrode
X = 200 mV/in
Y = 0.1 mA/in
rest potential = -0.1 V
scanned potential range = -0.2 V to +0.8 V
scan rate = 200 mV/sec
agitation = 500 rpm
temperature = 50°C

Figure A-34: Experimental data for February 27, 1996 am.

February 27, 1996 pm: This experiment was performed on -38+25 μm material and produced a slope for the surface chemical reaction controlled model of 0.00492 min^{-1}, having a linear correlation coefficient of 0.999. In attempting to determine the best fit linearized form of the three nonporous shrinking sphere models, the last point was omitted from this data set (see the regression coefficient data presented in Table 4.2).

Table A-35: Experimental Data for February 27, 1996 pm.

Time (min)	Extent of Reaction	Total Coulombs	Temperature (°C)
0	0	0	50
13	0.205	43	50.5
23	0.318	91	50
33	0.409	126	50
43	0.500	157	50
53	0.583	186	50
63	0.674	213	50
73	0.720	240	50
83	0.795	260	50
93	0.848	283	50
103	0.886	303	50
113	0.917	323	50
123	0.939	337	50
133	0.955	347	50
143	1.000	355	50

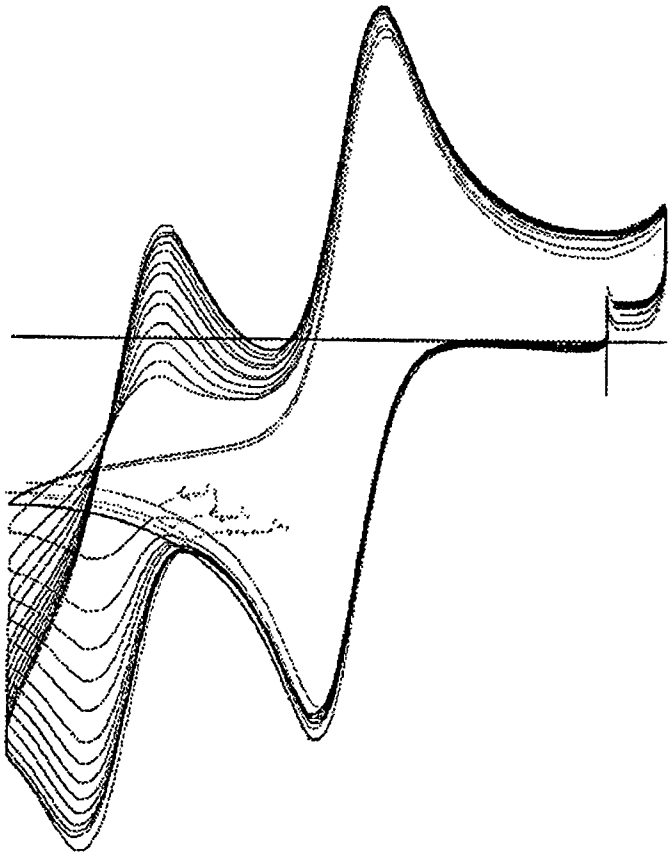

February 27, 1996 pm
1.000 gram -38+25 micron PuO_2
0.5964 g $FeCl_2$-$4H_2O$ = 40 *mM* Fe
75 ml of 7 *M* HCl in agitated cell
double junction reference electrode
platinum working electrode
X = 200 mV/in
Y = 0.1 mA/in
rest potential = -0.1 V
scanned potential range = -0.2 V to +0.8 V
scan rate = 200 mV/sec
agitation = 500 rpm
temperature = 50°C

Figure A-35: Experimental data for February 27, 1996 pm.

February 28, 1996: This experiment was performed on -25+15 μm material and produced a slope for the surface chemical reaction controlled model of 0.00459 min^{-1}, having a linear correlation coefficient of 0.994. In attempting to determine the best fit linearized form of the three nonporous shrinking sphere models, the last point was omitted from this data set (see the regression coefficient data presented in Table 4.2).

Table A-26: Experimental Data for February 28, 1996.

Time (min)	Extent of Reaction	Total Coulombs	Temperature (°C)
0	0	0	50
10	0.179	45	49.5
20	0.297	90	50
30	0.386	117	50
40	0.462	144	50
50	0.545	172	50
60	0.614	195	50
70	0.669	216	50
84	0.738	241	50
90	0.779	255	50
100	0.834	275	50
112	0.883	293	50
120	0.917	310	50
130	0.931	325	50
140	0.966	336	50
150	1.000	350	50

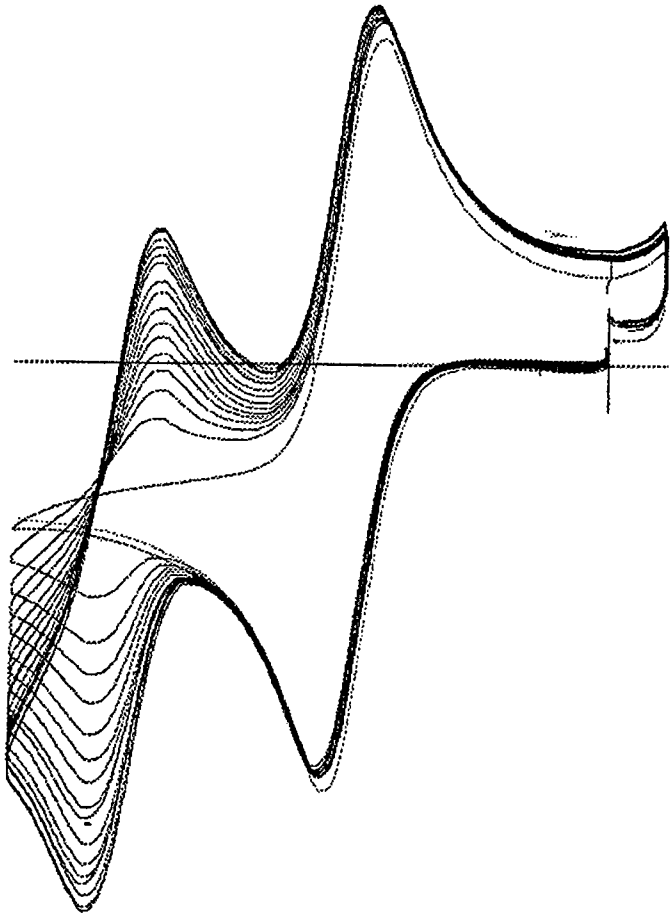

February 28, 1996
1.000 gram -25+15 micron PuO_2
0.5964 g $FeCl_2$-$4H_2O$ = 40 *mM* Fe
75 ml of 7 *M* HCl in agitated cell
double junction reference electrode
platinum working electrode
X = 200 mV/in
Y = 0.1 mA/in
rest potential = -0.1 V
scanned potential range = -0.2 V to +0.8 V
scan rate = 200 mV/sec
agitation = 500 rpm
temperature = 50°C

Figure A-36: Experimental data for February 28, 1996.

May 9, 1996: The data for this assemblage experiment was used in the Arrhenius evaluation of the reaction activation energy. The slope of the plot of the surface chemical reaction controlled model was determined to be 0.0124 min^{-1}, having a linear correlation coefficient of 0.993. In attempting to determine the best fit linearized form of the three nonporous shrinking sphere models, the last point was omitted from this data set (these regression data were not presented in Table 4.2).

Because of the speed of this reaction, data points were attempted at 5 min. intervals. Data points at 30 min. and 35 min. (t_6 and t_7) were omitted because t_6 was less than t_5 indicating a fouled working electrode surface, and t_7 omitted because the correct potentiostat settings were not returned to normal after electrode cleaning. It was not possible to scale the peak height appropriately and salvage the data point at t_7.

Table A-37: Experimental Data for May 9, 1996; Arrhenius Data at 75°C.

Time (min)	Extent of Reaction	Total Coulombs	Temperature (°C)
0	0.000	0	74.5
5	0.200	57	75.5
10	0.340	130	76
15	0.460	193	75.5
20	0.563	248	75
25	0.707	293	75
40	0.860	372	76.5
45	1.000	388	75

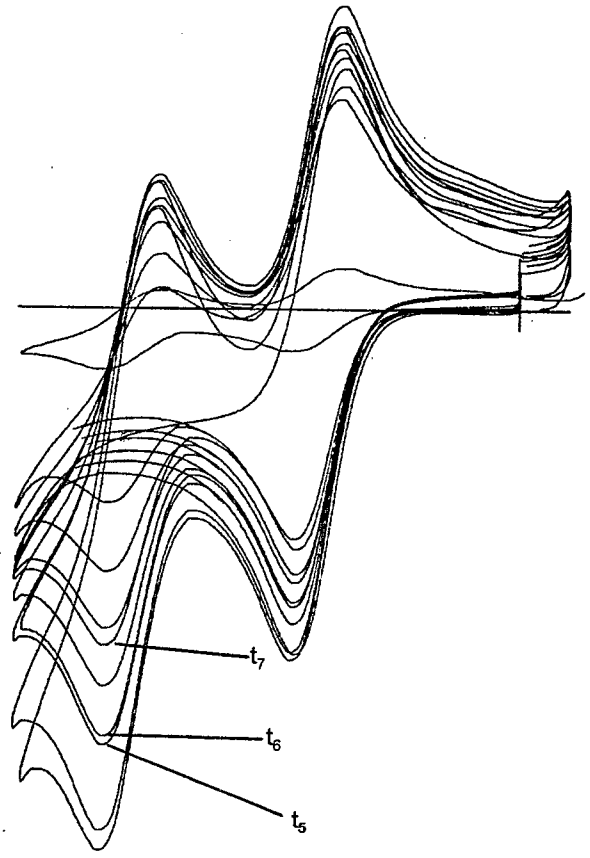

May 9, 1996
1.000 gram PuO_2 assemblage
0.5964 g $FeCl_2$-$4H_2O$ = 40 *mM* Fe
75 ml of 7 *M* HCl in agitated cell
double junction reference electrode
platinum working electrode
X = 200 mV/in
Y = 0.1 mA/in
rest potential = -0.1 V
scanned potential range = -0.2 V to +0.8 V
scan rate = 200 mV/sec
agitation = 500 rpm
temperature = 75°C

Figure A-37: Experimental data for May 9, 1996; Arrhenius data at 75°C.

This report has been reproduced directly from the
best available copy.

It is available to DOE and DOE contractors from
the Office of Scientific and Technical Information,
P.O. Box 62,
Oak Ridge, TN 37831.
Prices are available from
(615) 576-8401.

It is available to the public from the
National Technical Information Service,
US Department of Commerce,
5285 Port Royal Rd.
Springfield, VA 22616.

Los Alamos
NATIONAL LABORATORY
Los Alamos, New Mexico 87545